BROADBAND COMPUTATIONAL RHEOLOGY FOR MATERIAL CHARACTERISATION

Matthew George Smith

Submitted in fulfilment of the requirements for the
Degree of Doctor of Philosophy

James Watt School of Engineering
College of Science and Engineering
University of Glasgow

March 2023

Abstract

Rheology is a wide-reaching field whose applications are underpinned by a *prior* knowledge of the 'viscoelastic' properties of (complex) materials generally employed across industries such as oil and gas, food processing, cosmetics, and biophysics; the latter being the main focus of this thesis. Biomedical studies often only have access to small sample volumes, which make conventional bulk rheology techniques unsuitable for their characterization, this has led to the development of a new field called microrheology, where new techniques can characterise the viscoelastic properties of complex fluids by using only a few microlitres of a sample volume. As a branch of rheology, microrheology utilises the same underpinning principles and aims to calculate a material's properties, including the complex shear modulus, which in turn describes how the material behaves.

The following thesis is aimed at investigating the use of microrheology with optical tweezers in a series of papers exploring different areas within the field of microrheology. Each paper targets certain gaps within the field and as such this thesis is fairly broad reaching touching on algorithm development, machine learning and shear flow analysis.

Chapter 2 presents the work "i-RheoFT: Fourier transforming sampled functions without artefacts", and introduces an open access MATLAB code, "i-RheoFT", which can evaluate the Fourier transform of any generic time-dependent function with a finite number of data points. I-RheoFT could be of particular interest and use to those who study sampled or time-averaged functions. The paper investigates three experimental parameters employing i-RheoFT: (i) the density of initial experimental data points that describe the signal, (ii) the interpolation function used to perform virtual oversampling of the signal, which is required for accurate evaluation of the Fourier transform, and (iii) the effect that signal noise has on the Fourier transform. As the chapter shows, a high number of initial data points or a high signal-to-noise ratio corresponds to a good performance for each interpolation function used. Alternatively, a low number of initial points or signal-to-noise ratio corresponds to poor performance across each interpolation function used. As one would expect, there exists a threshold, for both the signal-to-noise and the number of initial points, at which the

performance becomes acceptable and has been identified in both cases in the chapter. More recently further development of this work has led to the creation of two open source applications [1, 2] available for download, these aim to compute the complex shear modulus from bulk rheology and atomic force microscopy measurements respectively. Moreover, since its publication this work has been used in three studies [3–5], two of which feature the author of this thesis as a co-author.

Chapter 3 examines the claim that linear microrheology with optical tweezers should not be used for the study of living systems due to the variation between the time required to collect statistically valid data and the mutational time of the studied living system. This work is a first step at enhancing conventional statistical mechanics analysis of particle trajectories, captured using microrheology with optical tweezers, by exploiting machine learning techniques to reduce the current measurement time from tens of minutes down to as little as one second. The chapter describes how computer simulated trajectories, of Newtonian fluids with viscosities spanning three decades, have been used to corroborate the requirement for sufficiently long measurements to offer a good estimation of the fluid viscosity using conventional analytical techniques. In addition, the work provides a method for estimating the measurement time of a microrheology with optical tweezers experiment, based on the relative viscosity of the fluid being analysed to produce an uncertainty as low as 1%. Furthermore, this chapter presents a machine learning algorithm that can predict the viscosity of both simulated and real trajectories, carrying an error as low as $\sim 0.3\%$, using only one second of data. It is believed that with this machine learning enhancement, microrheology with optical tweezers will become a powerful tool for studies involving living systems.

Chapter 4 presents an investigation into flow induced self-assembly (FISA) of particles suspended in a viscoelastic shear thinning fluid subjected to simple shear flow. This phenomena is currently not fully understood and little has been done in literature so far to investigate the possible effects of the shear-induced elastic instability. In this work, a bespoke cone and plate shear cell is used to provide new insights on the FISA dynamics. In particular, we have fine tuned the applied shear rates to investigate the chaining phenomenon of micron-sized spherical particles suspended into a viscoelastic fluid characterised by a distinct onset of elastic instability. This has allowed us to reveal three phenomena never reported in literature before, i.e.: (I) the onset of the elastic instability is strongly correlated with an enhancement of FISA; (II) particle chains break apart when a constant shear is applied for 'sufficiently' long-time (i.e. much longer than the fluids' longest relaxation time). This latter point correlates well with the outcomes of parallel superposition shear measurements, which (III) reveal

a fading of the elastic component of the suspending fluid during continuous shear flows.

Contents

List of Tables

List of Figures

Symbols & Acronyms

A	Asymmetric Double Sigmoid Function Parameter: Amplitude.
$A(\tau)$	Normalised Position Autocorrelation Function.
A_P	Plate Area.
A_f	Alignment Factor.
B	Highest frequency contained in the original signal.
$De_{OT,Eff.}$	Nominal Deborah Number for Optical Tweezers.
$De_{OT,Nom.}$	Nominal Deborah Number for Optical Tweezers.
De_{OT}	Deborah Number for Optical Tweezers.
E	Modulus of Elasticity.
F	Force applied to plate.
F_s	Spring Force.
G'	Elastic Modulus.
G''	Viscous Modulus.
$G''(\omega)$	Frequency Dependent Viscous Modulus.
$G'(\omega)$	Frequency Dependent Elastic Modulus.
$G(t)$	Time Dependent Shear Relaxation Modulus.
G^*	Complex Shear Modulus.
$G^*(\omega)$	Frequency Dependent Complex Shear Modulus.
$J(t)$	Creep Compliance.
L	Chain Length.
M	Dimensionless parameter denoting the onset of elastic instability..
M_{Norm}	Normalised Dimensionless parameter denoting the onset of elastic instability..
M_{crit}	Critical value of M when flow becomes unstable..
N	Total Number of Readings.
N_1	First Normal Stress Difference.
N_2	Second Normal Stress Difference.
N_L	Number of Chains of Length, L.

N_e	The number of experimental data points within the explored time window.
N_w	Number of positional data points acquired during the microrheology measurement performed in water..
N_{traj}	Number of Trajectories.
Re	Reynolds Number.
T	Temperature.
T_a	Dimensionless parameter that accounts for the relative position of the material's characteristic relaxation time..
T_m	Measurement Time.
U	Relative velocity of moving plate.
Wi	Weissenberg number.
τ	Lag-time.
β	Oversampling Factor.
$\delta(\omega)$	Frequency Dependent Phase Shift.
δ	Phase Shift.
$\dot{\gamma}$	Shear Rate.
ε	Extensional Strain.
η	Viscosity.
$\gamma(t)$	Time Dependent Strain.
γ_A	Shear Strain Amplitude.
$\hat{\gamma}(t)$	Fourier transform of time dependent Strain.
$\hat{\sigma}(t)$	Fourier transform of time dependent Stress.
κ	Optical Trap Stiffness.
$\langle r^2 \rangle$	Variance of the Particle Position.
ω	Angular Frequency.
σ	Stress.
$\sigma(t)$	Time Dependent Stress.
σ_A	Shear Stress Amplitude.
τ_c	Characteristic relaxation time.
$E(\vec{r})$	Confining Field of Optical Trap.
$\Pi(\tau)$	Normalised Mean Squared Displacement.

α	Cone Angle.
$\dot{g}_\infty$	Fourier Transform of the Oversampled Function from i-Rheo.
$\eta^*(\omega)$	Complex Viscosity.
η_0	Nominal Viscosity Value.
η_{Bulk}	Rotational Shear Viscosity obtained using a Stress-controlled Rheometer.
η_r	Relative Viscosity.
$\hat{A}(\omega)$	Fourier Transform of NPAF.
$\hat{\Pi}(\omega)$	Fourier Transform of NMSD.
$\hat{g}(\omega)$	Fourier Transform of the Oversampled Function from i-Rheo.
λ	Characteristic Relaxation Rate.
λ_{PM}	Characteristic Relaxation Time for onset of elastic instability.
$\omega_{c/p}$	Rotational frequency of the cone/plate.
ω_M	Rotational frequency of the motors.
ω_{cM}	Rotational frequency of the cone motor.
ω_{pM}	Rotational frequency of the plate motor.
τ_{OT}	Characteristic time of the compound system of Optical Tweezers, suspending fluid and suspended bead.
τ_R	Rouse time.
τ_e	Entanglement Time.
τ_{rep}	Reptation Time.
$\vec{a}(t)$	Particle Acceleration.
$\vec{f}_R(t)$	Gaussian White Noise.
$\vec{r}(t)$	Particle Position.
$\vec{v}(t)$	Particle Velocity.
$\xi(t)$	Generalised time-dependent memory function.
$\lvert\eta^*(\omega)\rvert_{MOT}$	Complex Viscosity obtain using Microrheology with Optical Tweezers.
a	Particle Radius.
d	Distance between plates.

d_m	Diameter of Motor.
$d_{c/p}$	Diameter of the cone/plate.
f_s	Sampling Frequency.
$g(t)$	Time dependent function to be Fourier transform with i-Rheo.
i	Imaginary Unit.
k	Spring Constant.
k_B	Boltzmann's Constant.
m	Particle Mass.
s	Deflection path.
t	Time.
w_1	Asymmetric Double Sigmoid Function Parameter: Curve Width.
w_2	Asymmetric Double Sigmoid Function Parameter: Shaping Parameter.
w_3	Asymmetric Double Sigmoid Function Parameter: Shaping Parameter.
x	Spring Deformation.
x_c	Asymmetric Double Sigmoid Function Parameter: Peak Center.
y_0	Asymmetric Double Sigmoid Function Parameter: Steady State Value.
APE	Absolute Percentage Error.
AR	Acquisition Rate.
CMOS	Complementary Metal-oxide Semiconductor.
CNN	Convolutional Neural Network.
Deep NN	Deep Neural Network.
DFT	Discrete Fourier Transform.
DIP	Density of Initial Experimental Points.
DLS	Dynamic Light Scattering.
DPSS	Diode Pumped Solid State.

DWS	Diffusing Wave Spectroscopy.
FISA	Flow-Induced Self-Assembly.
i-RheoFT	Open-access MATLAB code.
LVE	Linear Viscoelastic.
Makima	Modified Akima Piecewise Cubic Hermite Interpolation.
MAPE	Mean Absolute Percentage Error.
ML	Machine Learning.
MOT	Microrheology with Optical Tweezers.
MRAE	Mean Relative Absolute Error.
MROA	Mean Rate of Accumulation.
MSD	Mean Squared Displacement.
NMSD	Normalised Mean Squared Displacement.
NN	Neural Network.
NPAF	Normalised Position Autocorrelation Function.
NSE	Neutron Spin Echo.
OT	Optical Tweezers.
OWch	Optimally Windowed-chirp.
PAM	Polyacrylamide.
PCHIP	Piecewise Cubic Hermite Interpolating Polynomial.
QPD	Quadrant Photodiode.
RAE	Relative Absolute Error.
RAM	Random-Access Memory.
ReLu	Rectified Linear Unit.

SLM	Spatial Light Modulator.
SM	Statistical Mechanics.
SNR	Signal-to-Noise Ratio.
Spline	Cubic Spline Data Interpolation.

Acknowledgments

As is often the case, the journey to completing this PhD thesis has been a long one since it began in September 2018. It is therefore fitting for me to acknowledge all of the people who have helped me along the way.

First and foremost, I would like to thank my supervisor Manlio Tassieri. Without your guidance and expert supervision I would not have been able to achieve this goal, and your interest and enthusiasm for my studies has been second to none. I would also like to thank my second supervisor Graham Gibson, your expertise allowed the work carried out in chapter 4 to exist and your insights for various projects have been exceedingly helpful.

I would like to thank the CDT in Intelligent Sensing and Measurement for the opportunity to study this degree in the first place and for their organisation of the initial taught year, which I learned a substantial amount from. I would like to thank the admin staff who always responded promptly to queries and were instrumental in helping to organise my trip to Seville for AERC 2022. Additionally, I would like to give a special thanks to Linda Hadfield for her extremely supportive and helpful meetings especially throughout lockdown when motivation was tough. I would also like to thank my colleagues at the CDT for their support and camaraderie throughout the years.

Next I would like to thank all of my friends, especially Ian, whose exceptional company I can always count on. I would also like to thank the Maitlands for their continued support and encouragement.

I would like to thank my Mum, Dad, Dan, Carla, Laura, Beth and Isabella. You have all supported me more than you know and I couldn't have asked for a better family. A special thanks to my Mum and Dad who have always encouraged me to achieve my goals even when I believed I wasn't capable of doing so. Last but certainly not least, I would like to express my deepest gratitude to Robyn. You have been by my side throughout these long years and your support and encouragement has been perfect. Thank you for everything and I hope I make you proud.

Declaration

I declare that, except where explicit reference is made to the contribution of others, that this thesis is the result of my own work and has not been submitted for any other degree at the University of Glasgow or any other institution.

Chapter 1

Introduction

1.1 Summary

This thesis presents a series of papers that have been published in the field of microrheology; an extension of the larger field of rheology. The works aim to address gaps within the literature surrounding passive microrheology with optical tweezers (MOT). The effectiveness of this measurement method has not been fully realised, due to its relative novelty within the field, and as such the papers presented here target specific areas of passive MOT to help bridge these gaps.

Beginning with an introductory chapter, this thesis provides some context and background to the field of rheology, microrheology and MOT. The first paper presented in this thesis is "*i-RheoFT: Fourier transforming sampled functions without artefacts*", found in Chapter 2, and focuses on the development of an open-access code for Fourier transforming generic time-dependent signals over a finite range. "*Machine learning opens a doorway for microrheology with optical tweezers in living systems*" is introduced in Chapter 3 and investigates both the requirement for passive MOT measurements to be measured for a long time and the use of machine learning to overcome this requirement. The final paper presented in this thesis is found in Chapter 4, titled "*The role of elastic instability on the self-assembly of particle chains in simple shear flow*", studies the relationship between the self-assembly of particle chains at shear rates tuned to the onset of elastic instability. The final chapter of this thesis summarises the findings, and future work, for each of the published works.

1.2 Introduction to Methods

1.2.1 Rheology

Rheology is the study of the flow of matter and was first introduced by Bingham in 1920 after a number of experiments [6–11] began to challenge the classical Hookean and Newtonian descriptions of materials. For context, Hooke's law is concerned with purely elastic solids (i.e. solids that store potential energy), the simplest example being a spring, where the deformation of the spring (x) is linearly proportional to the force (F_s) being applied such that:

$$F_s = -kx, \tag{1.1}$$

where k is the spring constant. Or for the case of purely elastic solids:

$$\sigma = E\varepsilon, \tag{1.2}$$

where σ is the stress (ratio of force and area) applied to the material, E is the modulus of elasticity, and ε is the extensional strain (ratio of the change in length and the original length) applied to the material. On the other side of the spectrum, Newton's description of fluids bears a striking resemblance to Hooke's law. A schematic representation is displayed in Fig.1.1 where a fluid is placed between parallel, stationary and moving plates.

From Fig.1.1, the fluid that is closest to each plate will gain the velocity of that plate (ignoring resistance effects). Consequently, the fluid between the plates will develop a velocity gradient in the direction of the moving plate. Intuitively, the velocity at any given point on this gradient is dependent on the velocity of the moving plate and the distance from the plate, which is the shear rate ($\dot{\gamma}$). Interestingly, the configuration shown in Fig.1.1 is called viscometric flow, where the gap size is small to ensure the velocity gradient is constant. As described previously, the stress applied to the fluid is just the force divided by the area and is linearly proportional to the shear rate by:

$$\sigma = \eta\dot{\gamma} \tag{1.3}$$

where η is the resistance to flow, commonly called the viscosity.

In both classical descriptions k, E and η are constant for the same material and Eqs.(1.1)-(1.3) are linearly proportional, meaning that doubling the applied force, doubles the deformation (or shear rate). Hence, researchers are interested in calculating the constants (k, E

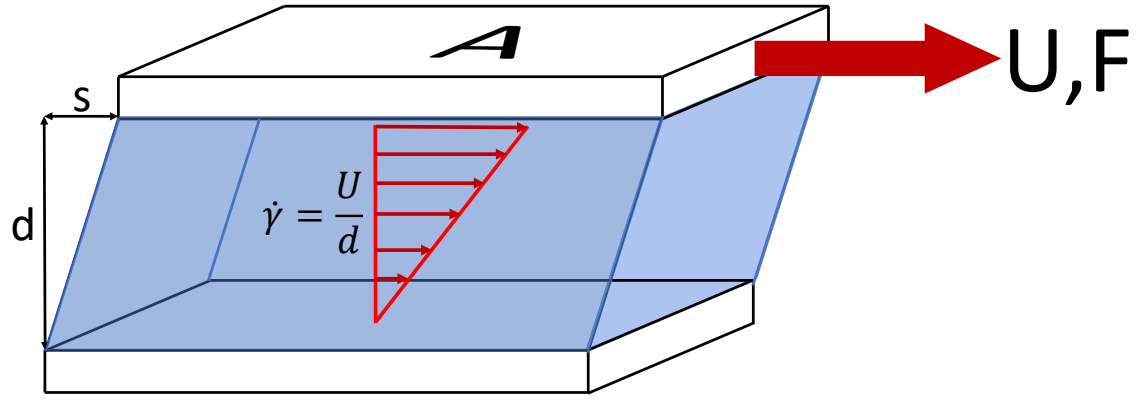

Figure 1.1: Schematic representation of Newtonian description of fluid behaviour under viscometric flow, where A_P is the area of the plate, U is the relative velocity of the moving plate, F is the force applied to the plate, d is the distance between plates, s is the deflection path, and $\dot{\gamma}$ is the shear rate.

and η) as they give a clear description of how the material will behave. Unfortunately, many materials behave neither purely elastically nor purely viscously but instead have both components and such classical descriptions of the material no longer give a good approximation of these materials [12].

The field of rheology concerns itself with the materials that lie in between the two extremes of Hookean solids and Newtonian liquids, and these materials can be described as viscoelastic as they have both an elastic and viscous component. A common 'Kitchen Science' experiment that demonstrates viscoelasticity involves combining corn-starch and water to produce a material that flows like a fluid if force is applied slowly, while the rapid application of force induces solid like behaviour. Importantly, materials that fall on the spectrum between the two extremes can behave very differently to each other and determining the variation between them is the remit of Rheologists.

As mentioned above, Hooke's Law measurements are often interested in calculating the elastic modulus, which is a single number providing information about the material i.e. the larger the elastic modulus the "stiffer" the material. To achieve this, researchers will apply stress to a solid of known dimension and measure the strain or vice versa, making the calculation of E trivial using Eq.(1.2).

Rheologists do something very similar except they must carry out oscillatory measurements instead of a linear application of stress/strain. For a detailed description of such oscillatory measurements this author would recommend [13] but for convenience they will be summarised here. Imagine in Fig.1.1 the moving plate is oscillating back and forth at a steady frequency with a set shear stress. As the plate moves, the fluid between each plate would be moving to catch up but there would be a delay between the maximum applied shear stress and the maximum deflection between the plates (i.e. shear strain). This oscillatory test would produce sine wave functions of the shear stress and strain as they increase and decrease during the measurement. By measuring the shear strain amplitude (γ_A) for a chosen shear stress amplitude (σ_A), one can calculate the complex shear modulus (G^*) through:

$$G^* = \frac{\sigma_A}{\gamma_A}, \tag{1.4}$$

which describes the entire viscoelastic behaviour of the material for the frequency applied. Additionally, the delay between the sine waves (or phase shift, δ) is also recorded during these measurements so that a vector diagram can be created as detailed in Fig.1.2.

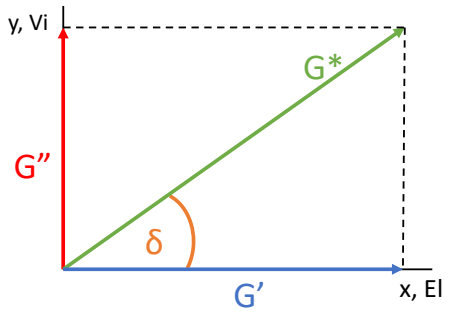

Figure 1.2: Vector diagram showing the relationship between the complex shear modulus G^* and the phase angle δ can be used to compute the elastic (G') and viscous (G'') component of G^*. [13]

This vector diagram can be used to split the complex shear modulus G^* into the elastic (G') and viscous (G'') components, which can be used to infer how the material under examination generally behaves i.e. if $G' > G''$ the material will behave more like a solid and if $G' < G''$ the material will behave more like a liquid.

However, as we have seen from the corn-starch and water example given above, the speed (or frequency) at which force (stress) or deformation (strain) is applied will determine the mechanical properties of the complex material and therefore applying stress/strain at just one frequency is not sufficient to describe the full behaviour. The gold standard for measuring the complex shear modulus is using a conventional bulk rotational rheometer to apply a

frequency sweep to the material. In such systems the material is rotated between two plates rather than a single plate moving back and forth, but the principles are the same. At each pre-set frequency, the stress or strain is pre-set or measured and the complex shear modulus can be calculated. However, the stress and strain in both these experiments is measured in the time domain, whereas the aim here is to determine the frequency dependent complex shear modulus ($G^*(\omega)$). To calculate this, one may determine the magnitude of $G^*(\omega)$ through the ratio of peak stress to peak strain, use the lag-time between the stress and strain curves to determine the phase angle (δ) and then compute $G'(\omega)$ and $G''(\omega)$. Alternatively, one may apply a Fourier transform to both the time-dependent stress and time-dependent strain individually such that:

$$G^*(\omega) = \frac{\hat{\sigma}(t)}{\hat{\gamma}(t)} \equiv \frac{\int_{-\infty}^{+\infty} \sigma(t) e^{-i\omega t} dt}{\int_{-\infty}^{+\infty} \gamma(t) e^{-i\omega t} dt} \tag{1.5}$$

where i is the imaginary unit ($i = \sqrt{-1}$), ω is the angular frequency, and $\hat{\sigma}(t)$ and $\hat{\gamma}(t)$ are the Fourier transforms, denoted by the hat ($\hat{}$) , of the time dependent stress and strain respectively. Due to the oscillatory nature of the experiment, the applied oscillatory strain and measured stress can be represented as:

$$\gamma(\omega,t) = \gamma_A sin(\omega t) \tag{1.6}$$

and

$$\sigma(\omega,t) = \sigma_A sin(\omega t + \delta(\omega)) \tag{1.7}$$

respectively [14]. Where $\delta(\omega)$ is the frequency dependent phase shift. These frequency dependent representations of the oscillatory stress and strain produce a new expression of the complex shear modulus as follows:

$$G^*(\omega) = \frac{\sigma_A}{\gamma_A} cos(\delta(\omega)) + i\frac{\sigma_A}{\gamma_A} sin(\delta(\omega)) \equiv G'(\omega) + iG''(\omega) \tag{1.8}$$

This general formula can be used to determine the properties of not only purely elastic solids and viscous liquids ($\delta(\omega) = 0 \equiv G^*(\omega) = G'(\omega)$ and $\delta(\omega) = \pi/2 \equiv G^*(\omega) = iG''(\omega)$ respectively) but also every material in between that has a combination of each component across a full range of frequencies. One should note that this method of analysis is only possible on the materials linear viscoelastic (LVE) region, which can be determined through an amplitude sweep, as applying a stress or strain above this region would result in destruction of the sample [13]. Interestingly, it has been shown that the frequency dependent shear complex modulus provides information about the internal structure of materials from the

atomic scale (10^{-10}m) at THz up to the macroscopic scale (cm) at relatively low frequencies [15–18], hence the importance of determining the LVE properties over the widest possible frequency range. The difficulty with achieving such a range with oscillatory amplitude and frequency sweeps is that these measurements can only provide information at the frequencies analysed, the experimental timescales associated with these tests can be on the order of hundreds of seconds, and the limits of a desired frequency range may be impossible to measure with a conventional rheometer. These limitations have led to the development of new procedures. A recent study by Geri *et al.* [19] introduced an "optimally windowed-chirp" (OWch) sequence aimed at replacing the standard, time-consuming frequency sweep. As with all chirps, the OWch sequence is a frequency-modulated deterministic signal and can be thought of as a combination of both a frequency and amplitude sweep. The benefits of using such a signal are: (i) using an OWch sequence can dramatically reduce the measurement time of oscillatory tests by 2 orders of magnitude and (ii) the optimisation of the OWch sequence leads to minimum error determined by the noise floor of the rheometer. In addition, a study by Tassieri *et al.* [20] has provided a simple analytical tool, i-Rheo that can access the widest possible range of frequencies using a step-strain measurement. In such a measurement, a finite strain is applied instantaneously to a sample and the stress is measured over time. The stress and strain in this instance can be related to the time-dependent shear modulus through:

$$G(t) = \frac{\sigma(t)}{\gamma(t)}, \tag{1.9}$$

only if the ramp time from the experimental stress and strain measurement is discarded and a preconceived fit is applied to the functions. i-Rheo on the other hand, does not require preconceived fitting procedures nor the idealisation of the experimental data. Instead, this tool works by first interpolating between the data points of the time-dependent functions ($\sigma(t)$,$\gamma(t)$) using a cubic spline function, then virtually oversampling the interpolation, i.e. increasing the number of data points, and finally passing this new function ($g(t)$), which must vanish for negative times, through the following Fourier transform method:

$$\begin{aligned} -\omega^2 \hat{g}(\omega) = i\omega g(0) + \left(1 - e^{-i\omega t_1}\right) \frac{(g_1 - g(0))}{t_1} + \\ + \dot{g}_\infty e^{-i\omega t_N} + \sum_{k=2}^{N} \left(\frac{g_k - g_{k-1}}{t_k - t_{k-1}} \right) \left(e^{-i\omega t_{k-1}} - e^{-i\omega t_k} \right), \end{aligned} \tag{1.10}$$

where ω is the frequency, $\hat{g}(\omega)$ is the Fourier transform of the signal, $g(0)$ is the value of the signal extrapolated to zero time, t_1 and g_1 are the initial time and corresponding signal value

respectively, $\dot{g}_\infty$ is the gradient of the signal extrapolated to infinite time, and t_k and g_k are the finite number of data points over which the signal was sampled where $k = 1...N$. The above Fourier transform method (Eq.(1.10)) is a significant improvement over a conventional discrete Fourier transform (DFT) because rheology measurements, such as the aforementioned step-strain measurement, often have features that do not fit with the preconceived approximations of a DFT, which can lead to an output in the Fourier domain that is peppered with artefacts [21]. The effectiveness of i-Rheo was validated by Tassieri *et al.*[20] and subsequent works [22–24] and allows researchers to determine the complex shear modulus using a relatively simple experimental procedure.

Rheology is a vitally important field of study used across a vast array of disciplines including the oil and gas, food processing and cosmetic industries, to name a few, and more recently within biophysics to measure the properties of biological materials [25–30].

1.2.2 Microrheology

Conventional rheological techniques, such as the rotational tests described above, are the gold standard when it comes to measuring material properties. However, the major drawback with this technique is the requirement for millilitres of a sample. This makes the procedure unsuitable for use in biophysical studies when only rare or precious samples are often available. Microrheology is a branch of rheology and is a field of study that aims to determine the LVE properties of materials at the micron length scale i.e. using a few μL of sample. Although microrheological techniques appear at first glance to be vastly different from those of conventional bulk rheology, the fundamental underlying principles are the same, with the aim of calculating the frequency dependent complex shear modulus of viscoelastic materials. Generally, microrheology techniques will employ microscale dielectric particles suspended in the material of interest to determine these properties. Depending on how these microscale particles are utilised determines whether the microrheology technique is 'passive' or 'active'. Passive microrheology analyses the random Brownian motion of the microscale particle, caused by the inherent thermal fluctuations of the material's molecules, to determine the LVE properties. Conversely, active microrheology techniques utilise an external force, such as magnetic or optical tweezers, to oscillate the suspended particles (much like bulk rheology) through the material while measuring the force response and hence determine the LVE properties [31]. One hybrid technique that can be used for both passive and active studies is microrheology with optical tweezers (MOT). Although this thesis consists of multiple research papers in slightly different areas, the main microrheology technique

discussed throughout all chapters is passive MOT and as such the principles underpinning passive MOT will be summarised here.

In order to understand how a particle suspended in a material can be used to determine the LVE properties of said material using passive MOT, one must first understand how optical tweezers (OT) are utilised in such a technique. OTs were first introduced by Ashkin [32] in the 1970s and are employed as extremely sensitive force transducers throughout the natural sciences [33–38]. They can optically trap, in three dimensions, a micron sized dielectric particle suspended within a media through the use of a highly focused monochromatic laser beam.

The mechanism of this optical trap can be described by the ray-optics model as the dielectric particle's diameter is more than twice the wavelength of the laser beam. This author would direct the reader to a detailed description of the ray-optics model in chapter 4 of [39], for convenience it will be summarised henceforth. As understood by Maxwell in 1873 [40], electromagnetic waves can apply force to a mirror or scattering object. An intuitive analogy would be a wave of water exerting a force on a barrier as it is reflected away. In the same way, a wave of laser light carries that same ability to apply force, however it is unremarkable at the macroscopic scale. Yet, as the length scale is decreased to the micron scale (10^{-6}m) the optical force is sufficient to displace micron sized particles. The particle in question has a different refractive index to the media surrounding it and therefore as a ray of laser light enters the particle, the light is refracted causing a change in momentum of the ray. This change in momentum imparts an opposite and equal force to the particle, as described by Newton's third law.

A particle positioned at the beam centre will experience equal counteracting resultant forces and will therefore remain fixed. Within a highly focused laser, the beam's greatest intensity is at the beam centre and decreases towards the beam edge. If the particle moves away from the centre, the higher intensity rays close to the beam centre will refract to a greater extent than those rays closer to the beam edge. Consequently, these rays experience a greater change in momentum and hence a larger resultant force towards the trap center. The particle, in turn, will experience a restoring force, due to the large resultant force, back to the beam centre and hence the particle is now optically trapped. The shape of this restoring force is best described as a quadratic potential which is linearly proportional to the distance the particle is away from the beam centre i.e. the further it moves away the more restoring force it feels, providing the displacement is within the bead diameter.

Atoms and molecules continuously streak through the suspending media at random, due

to thermal fluctuations, bombarding any particle in their path. In turn the particle experiences Brownian motion [41] and randomly 'walks' through the media. In the case of an optically trapped particle in a MOT setup, the particle is weakly confined by the trap but can explore the volume of that trap. One important benefit of MOT is that calibration of the optical trap requires no external measuring equipment based on the theory of Equipartition of energy. This theorem states that for an object in thermal equilibrium, the same average energy, $k_BT/2$ will be present in each degree of freedom, where k_B is Boltzmann's constant and T is the temperature. The energy for each degree of freedom would be equal to the potential energy stored in the optical trap such that:

$$\frac{1}{2}k_BT = \frac{1}{2}\kappa\langle r^2\rangle, \tag{1.11}$$

where κ is the trap stiffness and $\langle r^2\rangle$ is the variance of the particle position, as described in chapter 5 of [39]. In passive MOT, a high speed motion detection device (usually a high speed camera) measures the particle's trajectory as it explores the optical trap and using Eqn.(1.11), it is therefore possible to find and calibrate the optical trap stiffness by measuring $\langle r^2\rangle$ at a given temperature for the degree of freedom one is interested in [42].

The particle trajectory can be used not only to calibrate the optical trap but also can give a good estimation of the frequency dependent complex shear modulus, $G^*(\omega)$. In the section "Theoretical Background" of Chapter 3, the reader will see a description of how one is able to convert the two-dimensional particle trajectory into $G^*(\omega)$, but for convenience it will be briefly summarised here.

For any generic fluid, the LVE properties can be inferred from the 2D trajectory of an optically trapped particle through the calculation of either the normalised mean squared displacement (NMSD, $\Pi(\tau)$) or the normalised positional autocorrelation function (NPAF, $A(\tau)$). The NMSD and NPAF are related to each other through the following equation:

$$\Pi(\tau) = \frac{\langle\Delta r^2(\tau)\rangle_{t_0}}{2\langle r^2\rangle_{eq}} \equiv \frac{\langle[r(t_0+\tau)-r(t_0)]^2\rangle_{t_0}}{2\langle r^2\rangle_{eq}} = 1-A(\tau), \tag{1.12}$$

where τ is the lag-time ($t-t_0$), $\langle r^2\rangle_{eq}$ is the variance of the particle position and $\langle\Delta r^2(\tau)\rangle_{t_0}$ is the mean squared displacement (MSD). It is important to note that the brackets $\langle ...\rangle_{t_0}$ denote an average over all initial times t_0. As will be shown in the following chapters, the necessity to perform time averaging to obtain the NMSD and NPAF means that it is of vital importance to capture the particle position over a long time with many individual time steps.

The NMSD and NPAF are related to the frequency dependent complex shear modulus through:

$$G^*(\omega)\frac{6\pi a}{\kappa} = \frac{\hat{A}(\omega)}{\hat{\Pi}(\omega)}, \tag{1.13}$$

where a is the particle radius, κ is the trap stiffness and $\hat{A}(\omega)$ and $\hat{\Pi}(\omega)$ are the Fourier transforms of $A(\tau)$ and $\Pi(\tau)$ respectively [43–45]. The analysis of these Fourier transforms can be determined through the use of Kramers-Kronig transformations [46–48]; however, such transformations produce high frequency artefacts in $G^*(\omega)$. More recent analytical methods, including the symmetric method introduced by Nishi *et al.* [49] and i-Rheo described previously [20], have aimed at reducing these high frequency artefacts; although i-Rheo has been shown to have greater accuracy [50] and therefore will be utilised in this thesis.

As discussed, passive MOT solves the problem of conventional bulk rheology techniques with its ability to attain the frequency dependent complex shear modulus, which describes the full behaviour of a material, using only a few μL of sample.

1.3 Thesis Aims

The aims of this thesis are:

- To open the availability of the analytical tool i-Rheo to a broader audience of researchers.
- To investigate how experimental parameters translate through the virtual oversampling procedure used in i-Rheo.
- To explore the claim that conventional MOT cannot be used to measure living systems.
- To show the potential machine learning has to enhance MOT and significantly reduce measurement time.
- To investigate the role of elastic instability on the flow-induced self-assembly of suspended particles in simple shear flow.

1.4 Thesis Outline

This thesis is a collection of original works that explore different areas within the field of microrheology. Each of the following technical chapters have their own aims and present individual pieces of published work carried out through the duration of the PhD.

Chapter 2 is the presentation of an open-access MATLAB code (i-RheoFT) that evaluates the Fourier transform of any generic time-dependent function sampled over a finite set of data points over a finite range. This work explored the effectiveness of i-RheoFT by comparing the resultant Fourier transforms of two generic functions to their corresponding analytical expressions. Additionally, this paper further investigated the performance of i-RheoFT by altering both the density of initial experimental points and signal-to-noise ratio of the generic functions as well as the interpolation method used to perform the virtual oversampling used within the code.

Chapter 3 presents a substantial investigation of the efficacy of passive MOT for use on living systems. This work explores the necessity of conventional passive MOT experiments to have long measurements ($\sim$ 17mins) with many individual readings (1 million data points), making them unsuitable for analysis of living systems, which are able to change their material properties at much shorter time scales. Furthermore, this work presents a machine learning algorithm that has the ability to predict viscosity of Newtonian fluids on only 1s of particle trajectory data, opening a doorway for passive MOT studies involving living systems.

Chapter 4 is an experimental investigation of particle self-assembly behaviour in simple shear flow whilst suspended in a viscoelastic shear thinning fluid (Polyacrylamide), whose frequency-dependent viscoelastic moduli have been determined through the use of classical bulk rheology and MOT measurements. In this work, a range of shear rates have been selected that bound the transition of the fluid from shear thinning to elastic instability. In addition, this work presents evidence that the self assembly of particle chains is significantly enhanced by the onset of elastic instability. Furthermore, the work displays the spontaneous reduction in particle chain length at relatively long times, during shear flow, which is speculated to be caused by a shear induced disentanglement of the polymer chains constituting the viscoelastic fluid as discussed in the chapter.

Chapter 5 is a discussion of the findings from each paper, their impact on the field of microrheology and it describes potential future work for each chapter.

Chapter 2

i-RheoFT: Fourier transforming sampled functions without artefacts

Matthew G. Smith [a], Graham M. Gibson [b], Manlio Tassieri [a],

[a] Division of Biomedical Engineering, James Watt School of Engineering, University of Glasgow, Glasgow, G12 8LT, UK

[b] SUPA, School of Physics and Astronomy, University of Glasgow, Glasgow, G12 8QQ, UK

Published: Scientific Reports

Access: https://doi.org/10.1038/s41598-021-02922-8 [51]

Author Declaration

I confirm that my contribution to this paper is over 50%.

2.1 Abstract

In this article we present a new open-access code named "i-RheoFT" that implements the analytical method first introduced in [PRE, 80, 012501 (2009)] and then enhanced in [New J. Phys. 14, 115032 (2012)], which allows to evaluate the Fourier transform of any generic time-dependent function that vanishes for negative times, sampled at a finite set of data points that extend over a finite range, and *need not* be equally spaced. i-RheoFT has been employed here to investigate three important experimental factors: (i) the 'density of initial experimental points' describing the sampled function, (ii) the interpolation function used to perform the "*virtual oversampling*" procedure introduced in [New J. Phys. 14, 115032 (2012)], and

(iii) the detrimental effect of noises on the expected outcomes. We demonstrate that, at relatively high signal-to-noise ratios and density of initial experimental points, all three built-in MATLAB interpolation functions employed in this work (i.e., Spline, Makima and PCHIP) perform well in recovering the information embedded within the original sampled function; with the Spline function performing best. Whereas, by reducing *either* the number of initial data points *or* the signal-to-noise ratio, there exists a threshold below which all three functions perform poorly; with the worst performance given by the Spline function in both the cases and the least worst by the PCHIP function at low density of initial data points and by the Makima function at relatively low signal-to-noise ratios. We envisage that i-RheoFT will be of particular interest and use to all those studies where sampled or time-averaged functions, often defined by a discrete set of data points within a finite time-window, are exploited to gain new insights on the systems' dynamics.

2.2 Introduction

In the field of soft-matter physics, it has been shown that at thermal equilibrium the motion and the interactions between the materials' building blocks govern the linear mechanical properties of matter [15, 17, 18]. These can be educed via a statistical mechanics (SM) analysis of the thermally driven motion of their constituents (e.g., molecules); whose dynamics can be measured either directly (e.g., neutron spin echo (NSE)[52, 53]) or implicitly by means of (nano/micro) tracers embedded into the samples [54]. Interestingly, the majority of these experimental methods return a measure of the materials' dynamics in an analytical form of a time-dependent exponential decay function, which in the simplest cases assumes the shape of a 'single' exponential decay $exp(-t/\tau_c)$, with τ_c being the characteristic relaxation time of the process under investigation (e.g., the diffusion of monodisperse molecules/tracers in Newtonian fluids [55] or bond percolation of transient gels [56]).

In general, for more complex systems than those just mentioned, a SM analysis of materials' thermal fluctuations may return more convoluted functions, such as a 'stretched' exponential $exp(-t/\tau_c)^{\beta}$, with $\beta < 1$. This is indeed a common outcome of both dynamic light scattering (DLS) [57] and diffusing wave spectroscopy (DWS) [58] measurements; e.g., when employed in the study of the dynamics of semi-flexible biopolymer solutions [59], for which the high-frequency mechanical properties are expected to show a frequency (ω) dependency of the linear viscoelastic (LVE) moduli proportional to ω^{β}, with $\beta = 0.75$ [60]. By increasing systems' complexity, such as in the field of polymer physics, a SM analysis of the

shear component of the stress tensor allows to evaluate the time-dependent materials' shear relaxation modulus $G(t)$ [23]. This is often a multi-modal decay function (i.e. characterised by multiple relaxation times) that embodies, without disclosing at once, the full frequency spectrum of the materials' LVE properties. These are instead fully revealed by the frequency-dependent materials' complex shear modulus $G^*(\omega)$, which is a complex number whose real and imaginary parts provide quantitative information on the elastic and viscous nature of the material, respectively [20]. Notably, these two moduli are in principle simply related to each other by means of the Fourier transform of the time derivative of $G(t)$, whose computation given a discrete set of data is at the heart of this article. A similar issue is encountered in the field of microrheology [39], where in the particular case of measurements performed with optical tweezers, a SM analysis of the trajectory of an optically trapped particle suspended into a complex fluid may return the particle normalised position autocorrelation function $A(\tau)$, or equivalently its normalised mean square displacement $\Pi(\tau) = 1 - A(\tau)$ (where τ is the lag-time or time interval), whose temporal form is a generic decay (or growth) function governed by the frequency-dependent linear viscoelastic properties of the suspending fluid [24].

Interestingly, a common feature for all the above mentioned time-dependent functions is that they are evaluated for a discrete number of timestamps, within a finite observation time window. Yet, one of the aims of most of the studies where they are employed is often to evaluate the 'continuous' frequency spectrum of the system, over the widest range of experimentally accessible frequencies. Thus the need of an effective Fourier transform algorithm to translate the information embedded into a generic time-dependent sampled function into those equipollent, but more explicit, in the frequency-domain. This is a non-trivial task [61], and has driven scientists to overcome such an issue by fitting the experimental data by means of a generalized Maxwell model (i.e., a finite sum of weighted single exponentials, each identifying a characteristic relaxation time of the system), which has a straightforward Fourier transform, but may potentially interpret the data [50]. Remarkably, an effective solution to this issue has been presented by Evans *et al.* [61] and its efficacy has been augmented by Tassieri *et al.* [44] by means of a "*virtual oversampling*" procedure that involves first a numerical interpolation between experimental data points by using a standard non-overshooting cubic spline function, and then generating a new, over-sampled data set, by sampling the interpolating function at a number of equally spaced points on a logarithmic time scale. The effectiveness of this method has been validated for a variety of applications within the fields of rheology and microrheology [44, 61]; however, its general validity has

been not fully exploited yet.

In this work, we have implemented the analytical method developed by Evans & Tassieri into a open-access MATLAB code named "i-RheoFT" (allowing its use to a broad audience, see SI) and investigated its accuracy as function of three important experimental factors that are often overlooked in many applications: (i) the density of initial experimental points (DIP) describing a generic time-dependent function (i.e., the sampled function), (ii) the interpolation function used to implement the virtual oversampling procedure, and (iii) the destructive effects on the expected outcomes due to the presence of (white) noise.

As we shall demonstrate, the relative value of the first parameter plays a crucial role in the quality of the outputs of all those experimental methods (such as DLS, DWS and NSE) where data are acquired at high frequencies (e.g., at 10^7 Hz or at 10^9 Hz in the case of DLS and NSE measurements, respectively) and stored in the form of time-averaged functions, which are often evaluated on-the-fly by means of fast correlators. These correlation functions are commonly evaluated only for a relatively 'small' number of lag-times within a finite time window, often spanning several decades (e.g., from 10^{-7} sec to 10^2 sec in the case of DLS measurements); thus avoiding the risk of clogging the machines' internal random-access memory (RAM) after a few seconds of measurement duration. The investigation of the second point has been driven by the fact that a few research groups have implemented the oversampling procedure by using different interpolation functions [62, 63] than the one employed in the original work [44]. Therefore, here we have compared the effectiveness of the following three interpolation functions already built-in MATLAB: a cubic spline data interpolation (Spline) [64] (as the one used in [44]), a modified Akima piecewise cubic Hermite interpolation (Makima) [65] and Piecewise Cubic Hermite Interpolating Polynomial (PCHIP) [66]. Notably, we can anticipate that, at relatively high DIP values and signal-to-noise ratios (SNR), all three of the above mentioned interpolation methods recover the information embedded into the sampled function to a high degree of fidelity, allowing the evaluation of its Fourier transform without a significant loss of information. Whereas, at relatively low values of *either* of DIP *or* SNR, the same is not true and a clear discrimination between their efficacy is achieved in both the time- and the frequency-domains.

2.3 Theoretical background

2.3.1 Fourier transform of raw data

In the digital era, continuous data storing does not exist and signals are stored at a finite acquisition rate (AR), whatever fast this process could be. Therefore, measurements are represented by a finite sequence of points, often equally spaced in time and rarely acquired at time intervals equally spaced on a logarithmic scale. Nonetheless, a logarithmic timestamp is often used in post-acquisition storing procedures, such as those employed in the study of fast quasi-stochastic phenomena, for which (i) a high AR is necessary and (ii) prolonged measurements are mandatory because of statistical principles. However, these two requirements would place a high demand on the RAM capacity of any machine. Thus, the common use of correlators to evaluate on-the-fly a correlation function of the acquired signal for a finite set of lag-times often logarithmically spaced within a defined time window that spans several decades; yet, without a need of storing the raw data.

Interestingly, the discrete nature of measurements has revealed to be a hurdle to overcome in many applications, especially for those where a Fourier transform is involved; simply because the latter is a linear (integral) operator that requires the integrating function to be defined $\forall t \in]-\infty,+\infty[$, and not just for a finite set of timestamps. This is equally true for all those processes where the integrating function is defined only for positive times (i.e., $\forall t \in [0^+,+\infty[$) and it is (or assumed to be) identically equal to zero $\forall t \in]-\infty,0^-]$ because of causality; such as in the studies of materials' relaxation processes after they have been subjected to either a finite deformation or a constant stress (creep), both applied within a small time interval (ε) [20, 61]. In this regard, an analytical procedure for the evaluation of the Fourier transform of any generic function sampled over a finite time window has been proposed by Evans *et al*. [61] to convert creep compliance $J(t)$ (defined as the ratio between the material strain $\gamma(t)$ and the applied constant stress) into $G^*(\omega)$ directly, without the use of Laplace transforms or fitting functions. This method is based on the interpolation of the finite data set by means of a piecewise-linear function. In particular, the general validity of the proposed procedure makes it equally applicable to find the Fourier transform $\hat{g}(\omega)$ of any time-dependent function $g(t)$ that vanishes for negative t, sampled at a finite set of data points (t_k, g_k), where $k = 1 \ldots N$, which extend over a finite range, and *need not* be equally

spaced [61]:

$$-\omega^2 \hat{g}(\omega) = i\omega g(0) + \left(1 - e^{-i\omega t_1}\right) \frac{(g_1 - g(0))}{t_1} + \\ + \dot{g}_\infty e^{-i\omega t_N} + \sum_{k=2}^{N} \left(\frac{g_k - g_{k-1}}{t_k - t_{k-1}} \right) \left(e^{-i\omega t_{k-1}} - e^{-i\omega t_k} \right) \tag{2.1}$$

where $\dot{g}_\infty$ is the gradient of $g(t)$ extrapolated to infinite time and $g(0)$ is the value of $g(t)$ extrapolated to $t = 0$ from above.

This method has been improved by Tassieri *et al.* [44] while analysing microrheology measurements performed with optical tweezers [39]. The authors found that a substantial reduction in the size of the high-frequency artefacts, from which some high-frequency noise tends to spill over into the top of the experimental frequency range, can be achieved by an *over-sampling* technique. The technique involves first numerically interpolating between data points using a standard non-overshooting cubic spline, and then generating a new, over-sampled data set, by sampling the interpolating function at a number of equally-spaced points on a logarithmic time-scale. We remind that, over-sampling is a common procedure in signal processing and it consists of sampling a signal with a sampling frequency f_s much higher than the Nyquist rate $2B$, where B is the highest frequency contained in the original signal. A signal is said to be oversampled by a factor of $\beta \equiv f_s/(2B)$ [67].

2.3.2 Interpolation functions

In this work we have employed three built-in interpolation functions listed in MATLAB: (i) Makima, (ii) Spline and (iii) Piecewise Cubic Hermite Interpolating Polynomial (PCHIP). The spline function has been used in previous studies by Tassieri *et al.* [24], however it is susceptible to overshooting if there are large jumps between data points. Makima and PCHIP are two interpolation functions that aim to reduce this oscillatory behaviour hence their selection for this work. These functions are fully described in Ref.s [64–66] and here they are briefly summarised for convenience of the reader.

The Makima algorithm for one-dimensional interpolation, also described in Ref.s [68, 69], is a modification to the Akima algorithm that performs cubic interpolation to produce piecewise polynomials with continuous first-order derivatives. The algorithm preserves the slope and avoids undulations in flat regions. A flat region occurs whenever there are three or more consecutive collinear points, which the algorithm connects with a straight line. When two flat regions with different slopes meet, the modification made to the original Akima algorithm gives more weight to the side where the slope is closer to zero. This modification

gives priority to the side that is closer to horizontal, which is more intuitive and avoids overshoot. Notice that, the original Akima algorithm gives equal weights to the points on both sides, thus evenly dividing the undulation.

The Spline algorithm, performs cubic interpolation to produce piecewise polynomials with continuous second-order derivatives. The result is comparable to a regular polynomial interpolation, but is less susceptible to heavy oscillation between data points for high degrees. Still, this method can be susceptible to overshoots and oscillations between data points at long times. Interestingly, when this is compared to the Akima algorithm, the latter produces fewer undulations and is better suited to deal with quick changes between flat regions.

The PCHIP algorithm, also performs a piecewise cubic polynomial interpolation in much the same way as the Spline function just mentioned. However, they differ in one key area which is that while the Spline functions' second-order derivative is continuous, the second-order derivative for PCHIP is unlikely to be and therefore the interpolation function is shape preserving for large jumps between data points. Additionally, the non continuous nature of the second-derivative means that PCHIP has no overshoots and much lower oscillation when the data is not smooth when compared to the Spline function.

2.3.3 Sampled functions and the density of initial points

In order to quantify the fidelity of the above mentioned interpolation procedures in recovering the original information contained by a sampled function, we have employed them to evaluate the Fourier transform (via Equation (2.1)) of two functions that are similar to those often seen in optical tweezers experiments [24, 39]: (I) a single exponential decay function:

$$A(t) = exp(-t/\tau_c), \tag{2.2}$$

describing the dynamics of a Maxwell fluid characterised by a single relaxation time τ_c, as shown in Figure 2.1 (top); and (II) a set of data resembling the mean square displacement of a weakly trapped probe particle suspended into a non-Newtonian fluid (Figure 2.1 (bottom)), which have been evaluated by means of the following series:

$$\Pi(q,t) = \sum_{q=1}^{\infty} \frac{1}{q^4}\left(1 - e^{-q^4 t}\right), \quad t \geqslant 0, \tag{2.3}$$

where q is the mode number and time is measured in units of the longest relaxation time for $q = 1$. It is important to notice that Equation (2.3) is a series definitely convergent, and in this work we have used its approximant $\Pi_{11}(q,t) = \sum_{q=1}^{11}(1 - e^{-tq^4})q^{-4}$; which provides a good estimation of the series $\forall t$. This has been corroborated by evaluating the incremental value

of the mean relative error of the approximant $\Pi_{11}(q,t)$ when compared to the approximants $\Pi_{100}(q,t)$ and $\Pi_{200}(q,t)$, for $t \in [10^{-2}, 10^{2}]$; which results in being as low as 0.0000287%.

Interestingly, the Fourier transform of the time derivative of both the functions described by Equations (2.2) and (2.3) can be calculated analytically and therefore an exact expression of the related complex moduli (i.e., $G_A^*(\omega)$ and $G_M^*(\omega)$, describing the viscoelastic properties of the suspending fluids) can be derived for both of them [24, 39, 50]:

$$G_A^*(\omega) = i\omega\hat{A}(\omega) = \frac{(\omega\tau_c)^2}{1+(\omega\tau_c)^2} + i\frac{\omega\tau_c}{1+(\omega\tau_c)^2} \tag{2.4}$$

and

$$G_M^*(\omega) = [i\omega\hat{\Pi}(\omega)]^{-1} = \left[\sum_{q=1}^{11} \frac{(q^4 - i\omega)}{(q^8+\omega^2)}\right]^{-1} \tag{2.5}$$

where $\hat{A}(\omega)$ and $\hat{\Pi}(\omega)$ are the Fourier transforms of the functions described by Equations (2.2) and (2.3), respectively. It follows that, Equations (2.4) and (2.5) can each act as a reference for a quantitative evaluation of the errors generated during the Fourier transform of a discrete set of data representing either of Equations (2.2) or (2.3), as function of both the density of initial points (DIP) and the oversampling factor (β). However, while the latter is a well known parameter in signal processing and would not affect the effectiveness of Equation (2.1) for relatively high values of β [44] (here it is kept constant to 50), DIP is introduced in this work to inform the scientific community of its relevance when modelling or interpreting a discrete set of data by means of a continuous interpolation function:

$$DIP = \frac{\log_{10}(N_e)}{\log_{10}(t_N/t_1)} \tag{2.6}$$

where N_e is the number of experimental data points within the explored time window, which extends from a lower end equal to t_1 to a maximum time equal to t_N. Therefore, a function sampled at a few MHz over a time window spanning from $t_1 = 10^{-7}$s to $t_N = 10$s would have DIP$= 1$ if N_e were equal to 10^8. Interestingly, this is not the case for the majority of the experimental techniques mentioned in the introduction (e.g. DLS, DWS, etc.), for which the technological constrain dictated by the finite RAM of the instruments is compensated by the adoption of correlators that *convolve* the high-speed acquired data into a finite set of *averaged* values calculated for a relatively small number of lag-times. Thus, returning a DIP value often much smaller than 1; which, as we shall demonstrate below, may lead to erroneous outcomes, especially at relatively low DIP values.

2.4 Results and Discussion

Let us start by considering both Equations (2.2) and (2.3) sampled at a relatively low acquisition rate, as shown in Figure 2.1. Both the functions are represented by 10 experimental points equally spaced on a logarithmic scale (black dots) and a continuous (pink) line, within a time window ranging from 10^{-2}s to 10^{2}s; which implies a DIP$= 1/4$.

The experimental data have been interpolated by using the three MATLAB built-in functions mentioned above and compared with the theoretical curve. *At a glance*, from Figure 2.1 it is possible to see the detrimental effect caused by a relatively low DIP value on all three interpolation processes, especially at large lag-times, where the Spline function performs worse. In order to quantify such a discrepancy, we have evaluated the relative absolute error (RAE(t)) of the three interpolation functions ($g_I(t)$) with respect to the theoretical functions computed by means of Equations (2.2) and (2.3):

$$RAE(t) = \frac{|g_I(t) - A(t)|}{A(t)} \quad or \quad RAE(t) = \frac{|g_I(t) - \Pi(t)|}{\Pi(t)} \tag{2.7}$$

The insets in Figure 2.1 show the RAE(t) of the three interpolation functions, with a focus in the time window ranging from 10^{1}s to 10^{2}s, where the error is at its highest. Interestingly, in the case of the single exponential decay, all three RAEs increase rapidly by almost ten decades across the explored time window, with the Spline function returning the highest error. A similar outcome can be seen in the case of $\Pi(\tau)$, where both PCHIP and Makima interpolation functions perform significantly better than the Spline function, returning a RAE(t) at long times almost five decades smaller. Notice that, the minima in the RAE(t) are due to the inherent nature of interpolation functions to pass through each experimental data point; a condition that is not guaranteed by any fitting procedure.

In order to investigate the fidelity of the interpolation process as function of DIP, we have evaluated the mean relative absolute error (MRAE) of the interpolating functions for N_e varying from 10 to 10^4, which implies a DIP ranging from $1/4$ to 1 (see Figure 2.2). The MRAE is defined as follows:

$$MRAE = \frac{100}{N} \sum_{n=1}^{N} \frac{|g_I(n) - A(n)|}{A(n)} \tag{2.8}$$

where N is the number of points at which all the functions are evaluated within the experimental time window $[10^{-2}, 10^{2}]$; in this study $N = 10^4$. Notice that, a similar expression to Equation (2.8) can be written in terms of $\Pi(\tau)$. From Figure 2.2 it is interesting to note that, at relatively low DIP values, all three function perform poorly; with the Spline function performing worst and the PCHIP returning the lowest error in both the cases; yet higher than

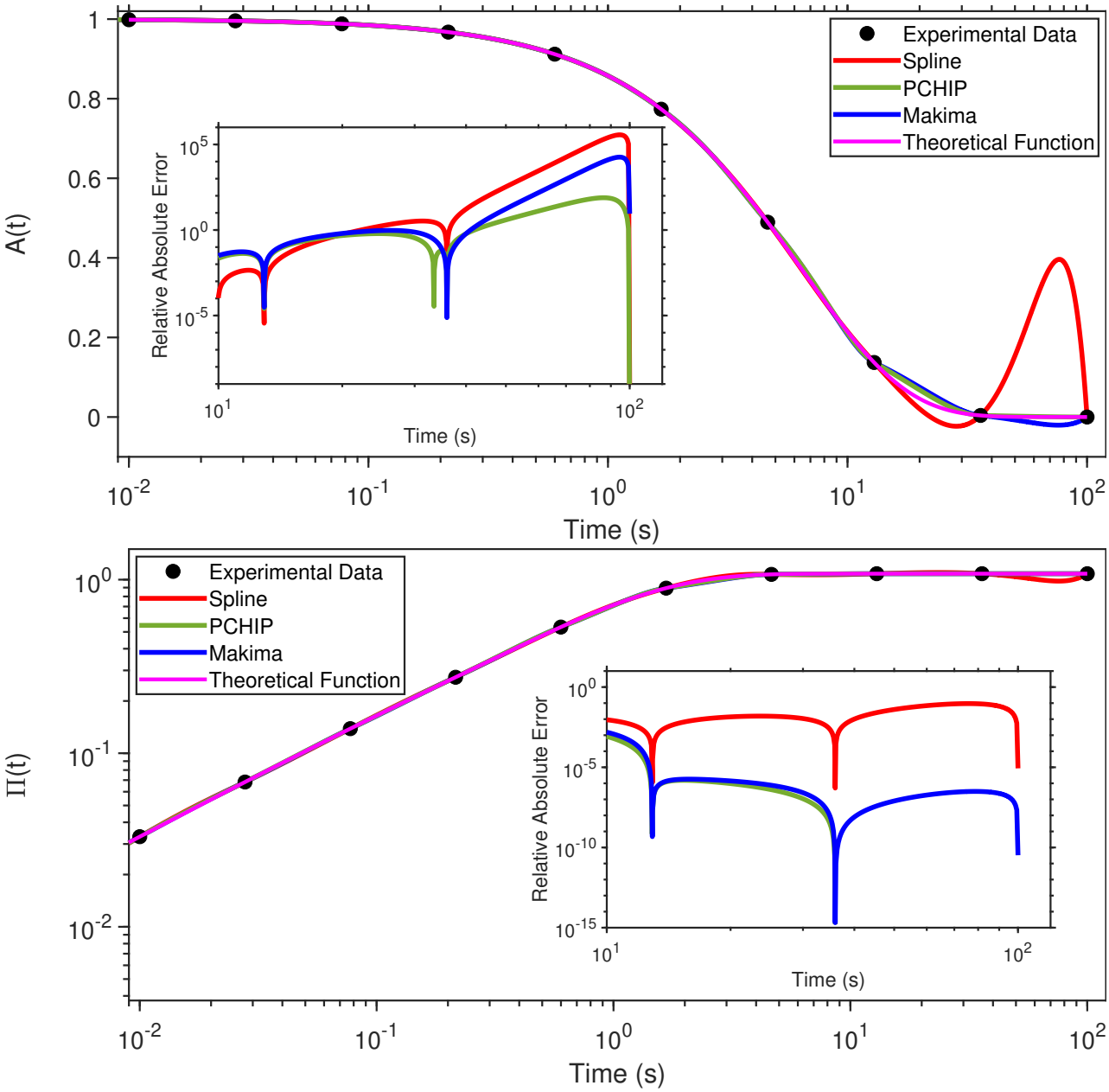

Figure 2.1: (Top) A single exponential decay function vs. time, representing the relaxation modulus of a single mode Maxwell fluid. (Bottom) A generic function resembling the normalised mean square displacement vs. time of an optically trapped particle suspended into a non-Newtonian fluid. Equations (2.2) and (2.3) are represented by a finite number of 'sampled' points and a continuous (pink) line. The points are also interpolated by means of three MATLAB built-in interpolation functions: Spline, PCHIP and Makima. The insets show the relative absolute error of each interpolation function with respect of either of Equations (2.2) and (2.3), as calculated using Eq.(2.7). The time window of the inset encompasses the final three points of the main graph, where the relative error is at its highest.

10^3% in the case of the single exponential decay (Figure 2.2, top). This exceptionally large error, found at low values of DIP, is due to the large difference between the theoretical function and each of the interpolation functions connecting the final data points, as displayed in Figure 2.1(top), where there is the largest time step. We argue that, the better fidelity shown by the PCHIP function can be attributed to the non continuous nature of the second-derivative of its interpolation algorithm, which prevents from overshoots and returns much lower oscillation in case of large jumps between data points (i.e., at low DIP) when compared to the Spline function.

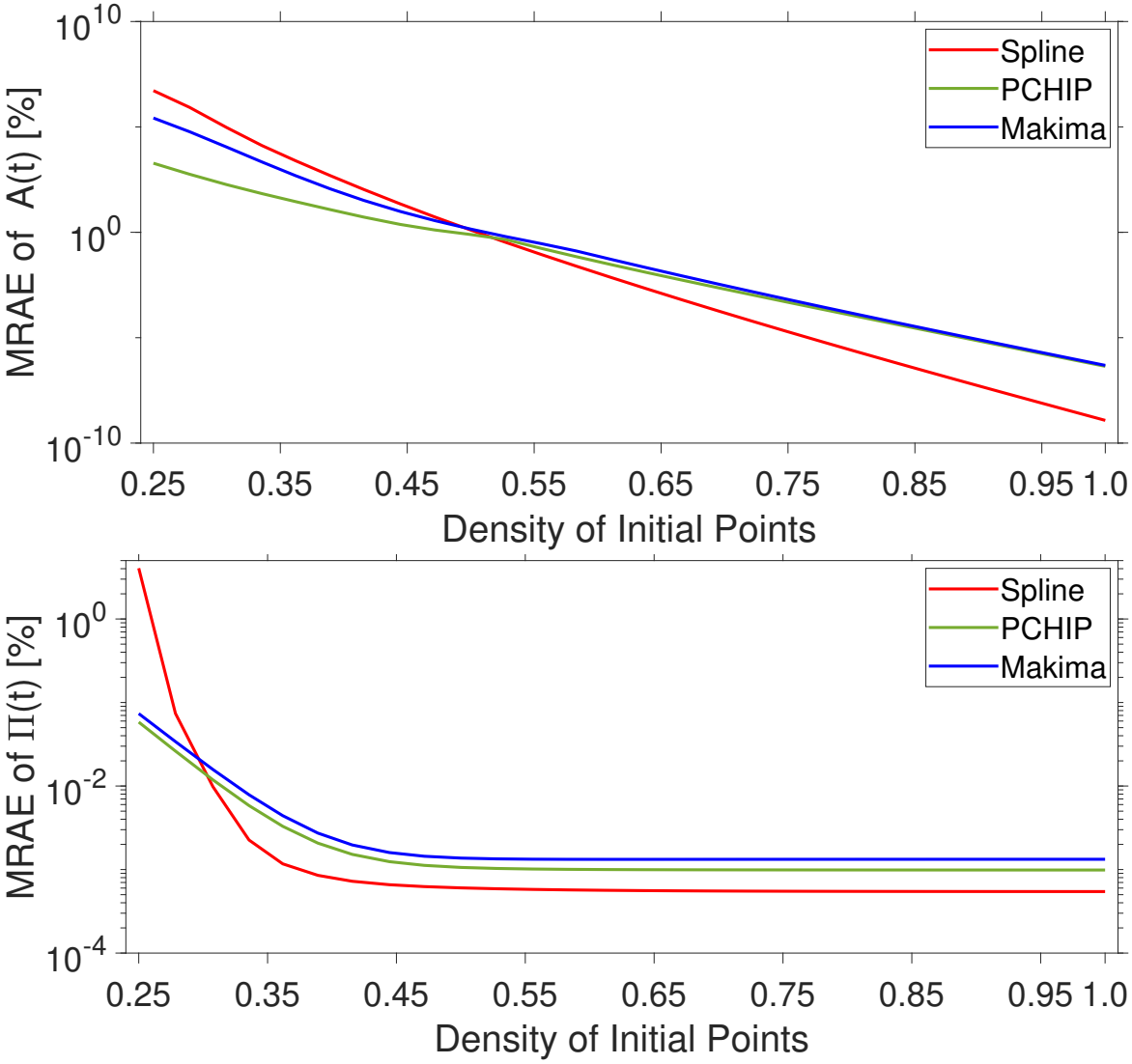

Figure 2.2: Mean relative absolute error (MRAE) vs. the density of initial experimental points (DIP) of the three MATLAB built-in interpolation functions: Spline, PCHIP and Makima. (Top) The MRAE is evaluated with respect to Equation (2.2). (Bottom) The MRAE is evaluated with respect to Equation (2.3).

Notably, for DIP values approaching 1, all three interpolation functions successfully re-

cover the sampled functions to a high degree of accuracy, returning MRAE values lower than $10^{-5}\%$ for the case of the single exponential decay. In this case, from a practical point of view, it is worth noting that the MRAE of all three interpolation functions falls below 1% for DIP values higher than circa 0.56, which implies a minimum number of 174 initial sampled points within the explored time window. Interestingly, when this outcome is applied for instance to DLS measurements (for which the experimental time window spans from 10^{-7} sec to 10^{2} sec), a DIP of 0.56 would imply a minimum number of $\approx 10^{5}$ initial timestamps (or lag-times); a condition never met in real experiments, where instead a DIP of circa 0.25 is commonly found. In the case of the NMSD (see Figure 2.2, bottom), at low DIP values, both PCHIP and Makima start with a MRAE smaller than 0.1%, while the Spline function starts with a MRAE value of circa 4%; thus confirming its poor performance at relatively low DIP values. Nonetheless, when comparing the errors generated by the interpolation procedures for the two cases of study, it is striking the different behaviour of their MRAE curves, which differ from each other by almost five orders of magnitude in opposite direction at the extremes of the explored range of DIP values.

Let us now investigate how the error propagates into the frequency-domain as function of both the chosen interpolation algorithm and the DIP, when performing the Fourier transform by means of the Evans & Tassieri's method. In Figure 2.3, the viscoelastic moduli evaluated by means of Equations (2.4) and (2.5) are drawn together with those derived by Fourier transforming the interpolation functions shown in Figure 2.1 for the case of DIP$= 1/4$.

From Figure 2.3, it is evident the detrimental effects of using a relatively low DIP value for determining the dynamic information embedded within the sampled functions. In particular, as discussed earlier, the Spline function carries the biggest error because of its poor performance in resembling the sampled functions at long times, which translates into artefacts in the low-frequency behaviour of both the moduli. Notably, these artefacts are significantly reduced in the case of Makima and even further in the case of PCHIP, which is the one that performs best at low DIP values. In Figure 2.3 we also report the viscoelastic moduli evaluated in the case of DIP$= 1$ as a means of comparison. The inset of Figure 2.3 (h) highlights the relatively small divergence of the elastic modulus from the expected value at high frequencies shown by all three of the interpolation functions. We argue that this (small) discrepancy is caused by the different constrains on the first and second derivatives adopted by the three interpolation algorithms to model the sampled function at the boundaries of the experimental time window; i.e, here within the time-gap occurring between the first experimental point at t_1 and the asymptotic one at $t = 0$.

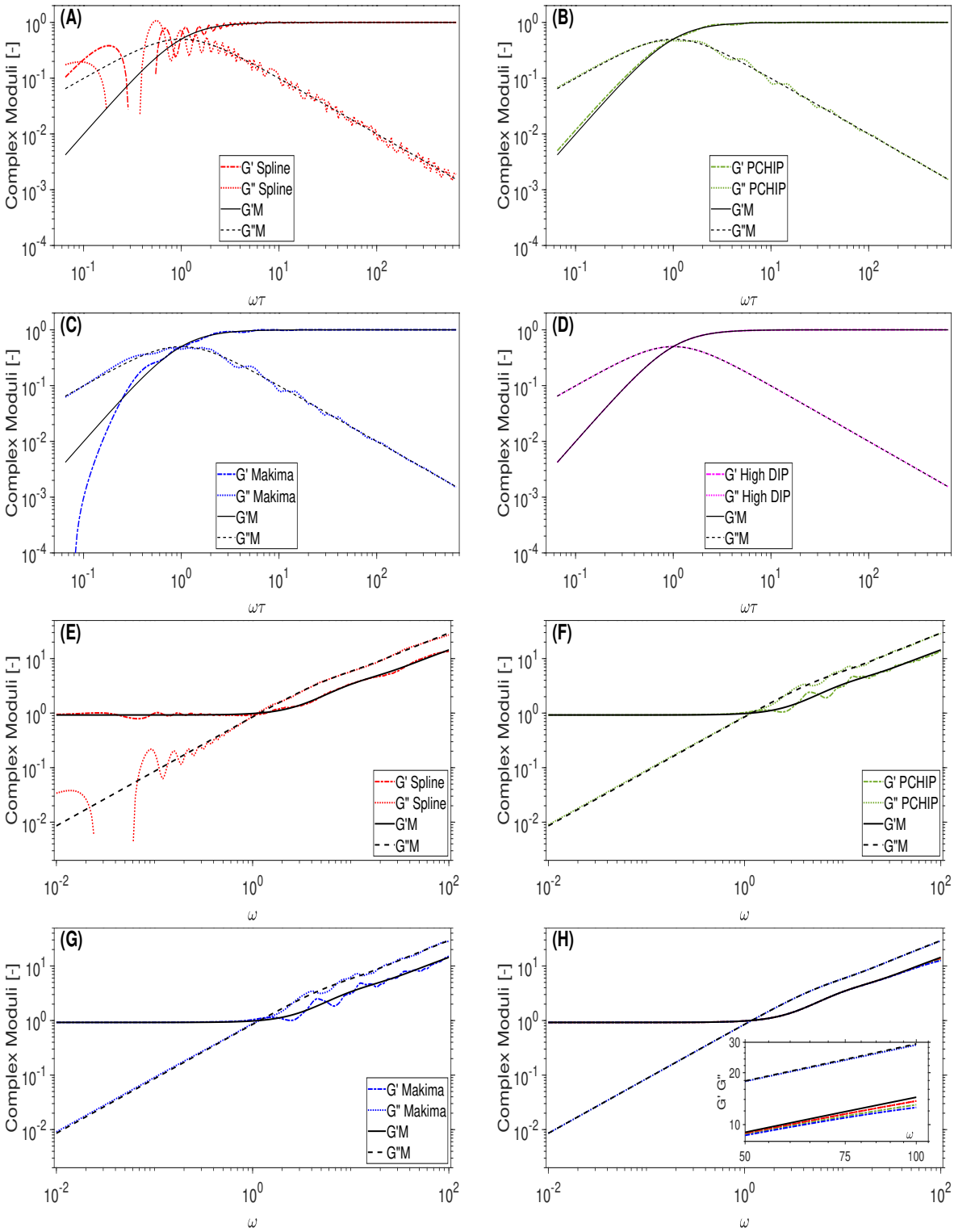

Figure 2.3: Comparison between the frequency-dependent complex moduli obtained via Equation (2.4) and those evaluated by Fourier transforming via Equation (2.1) the interpolations functions shown in Figure 2.1 for DIP$= 1/4$ in (A,B,C,E,F,G) and for DIP$= 1$ in (D,H). Note the spline interpolation function was used in (D) to represent High DIP (magenta line) and the Spline (red), PCHIP (green) and Makima (blue) functions were used in (H).

In order to quantify these discrepancies, we have evaluated the MRAE of both the real and imaginary parts (i.e., $G_i'(\omega)$ and $G_i''(\omega)$) of the calculated complex modulus with respect to their expected values (i.e., $G_A'(\omega)$ and $G_A''(\omega)$, $G_M'(\omega)$ and $G_M''(\omega)$) obtained from Equations (2.4) and (2.5), respectively:

$$MRAE = \frac{1}{N_\omega} \sum_{n=1}^{N_\omega} \frac{|G_i'(\omega_n) - G_A'(\omega_n)|}{G_A'(\omega_n)} \tag{2.9}$$

where $n = 1...N_\omega$ is the number of frequencies at which Eq. (2.9) is evaluated (here $N_\omega = 500$, with ω_n equally spaced on a logarithmic scale ranging from 10^{-2} to 10^2 Hz). A similar expression can be written for the viscous modulus, with $G_i'(\omega_n)$ and $G_A'(\omega_n)$ replaced by $G_i''(\omega_n)$ and $G_A''(\omega_n)$, and for Equation (2.5) by replacing $G_A^*(\omega_n)$ with $G_M^*(\omega_n)$, respectively. In particular, we have evaluated the MRAE for DIP values ranging from $1/4$ to 1; and the results are reported in Figure 2.4 for both the sampled functions. From Figure 2.4 top, it can be seen that (i) at relatively low DIP values (i.e., for DIP$\lesssim 0.33$) both the interpolation functions PCHIP and Makima perform significantly better than the Spline one; which, (ii) for DIP> 0.33 returns relatively lower values of the MRAE for both the moduli. Interestingly, for DIP> 0.9 the MRAE reaches a plateau value for both the moduli and all the interpolation functions; with the MRAEs of the elastic modulus showing an identical value for all three interpolation functions starting from DIP$= 0.75$. Moreover, it can be seen that for $0.33 <$DIP< 0.9 both PCHIP and Makima return a MRAE of the viscous modulus much higher than for the elastic one, which is actually comparable to the MRAE of both the moduli obtained by means of a Spline interpolation. From Figure 2.4 top, we can assert that, all the three interpolation functions provide a MRAE of both the moduli smaller than 1% for DIP> 0.4, which implies the need of a minimum number of initial data points of circa 40 within the explored time window.

From Figure 2.4 bottom, it can be seen that (i) at relatively low DIP values (i.e., for DIP$\lesssim 0.28$) both the interpolation functions PCHIP and Makima return a similar value of the MRAE (i.e. lower than 5%) for both the moduli; whereas, the Spline function returns a similar value of the MRAE only for the elastic modulus, while the MRAE for the viscous modulus goes up to a value of 50% at DIP$= 0.25$. Interestingly, for DIP> 0.5 the MRAE of both the viscoelastic moduli reach similar constant values for all the interpolation functions. Specifically, the MRAEs of the elastic modulus is of the order of 1% and the MRAEs of the viscous modulus is of the order of 0.1%. Notably, also in this case, the Spline function returns overall a lower (and constant) MRAE than both PCHIP and Makima for DIP> 0.4.

Let us now investigate how the presence of (white) noise impacts on the effectiveness of

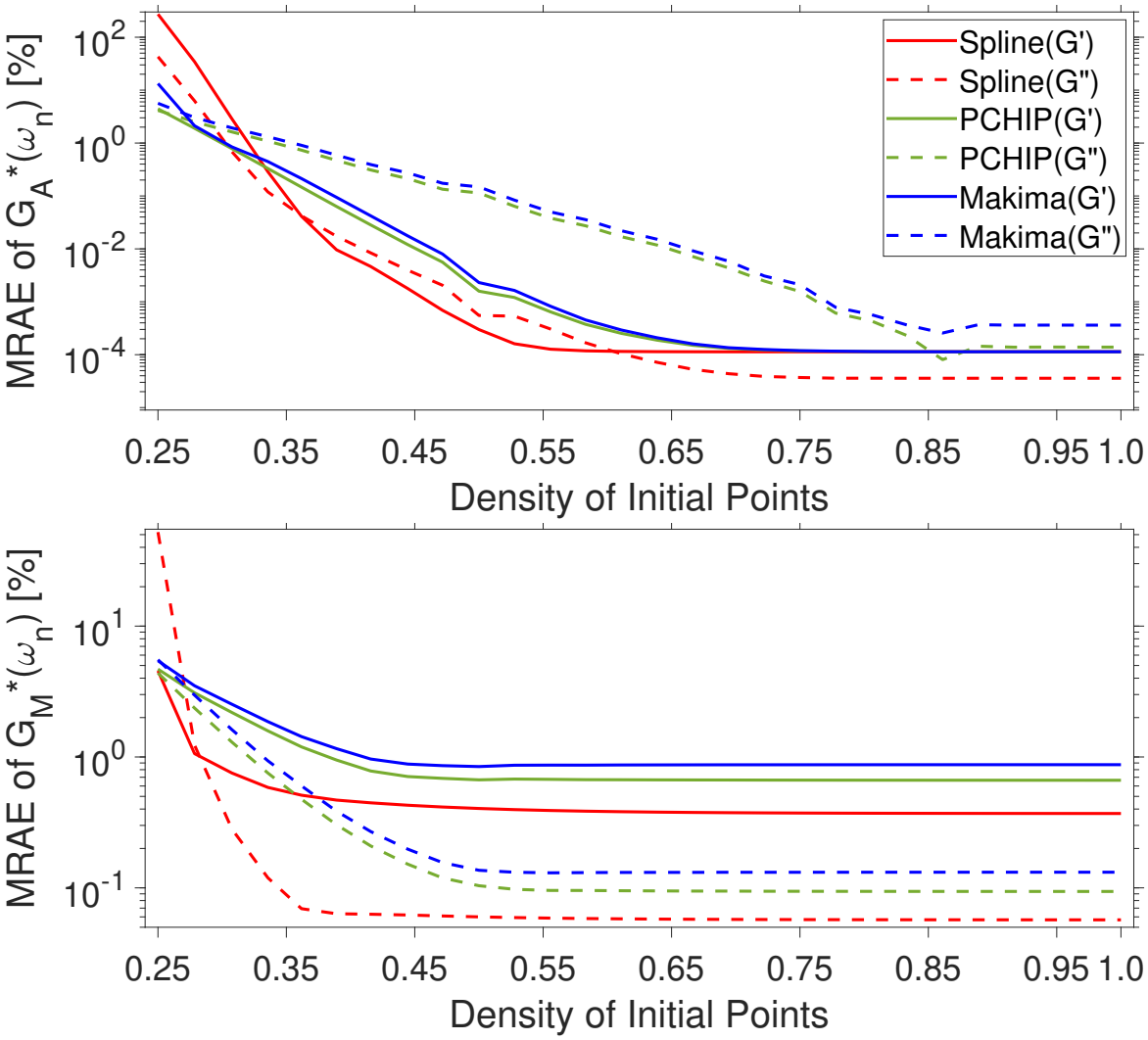

Figure 2.4: Mean relative absolute error (MRAE) of the frequency-dependent complex moduli determined by Fourier transforming (via Equation (2.1)) the interpolation functions shown in Figure 2.1 (top & bottom) for DIP values ranging from $1/4$ to 1.

the analytical method developed by Evans & Tassieri, when the above mentioned interpolation functions are employed to analyse both Equations (2.2) and (2.3), sampled at a fixed acquisition rate and for which the amplitude of the added noise is varied to explore a range of signal-to-noise ratios (SNR) spanning from 1dB to 350dB. The latter has been calculated by using the following equation:

$$SNR = \left(\frac{A_{signal}}{A_{noise}} \right)^2 , \tag{2.10}$$

where A_{signal} and A_{noise} are the root mean square amplitudes of the signal and the noise, respectively.

As a means of discussion, in Figure 2.5 are reported both Equations (2.2) (top) and (2.3) (bottom) drawn as continuous (pink) lines by using 10^4 experimental points linearly spaced within a time window of $[10^{-2}, 10^2]$ sec (i.e., DIP$=1$), to which a random white noise having a SNR $= 50$ has been added. The resulting 'noisy' functions have been then interpolated by means of all three the above mentioned MATLAB built-in interpolation functions. From Figure 2.5, and further elucidated hereafter, it can be seen that, at relatively low SNR, the different nature of the interpolation functions can lead to very large deviations from the expected values within the time window $[0, t_1]$, where $t_1 = 1/AR$. This is especially true in the case of the Spline function, as shown by the insets of Figure 2.5, both at top and bottom. In contrast, due to its non-continuous nature of the second derivative that prevents overshoots, the PCHIP algorithm performs better than both Spline and Makima functions. Notably, as we shall demonstrate below, these deviations are the major source of error at high frequencies when performing the Fourier transform via Equation (2.1), which otherwise reveals to be almost unaffected at low frequencies by the presence of the noise themselves; as shown in Figure 2.6, but also supported by the experimental evidences reported in Figures 7 and 8 of Ref. [20]. Here, Figure 2.6 shows a comparison between the viscoelastic moduli calculated via Equations (2.4) (top) and (2.5) (bottom) and those evaluated by Fourier transforming via Equation (2.1) the interpolations functions shown in Figure 2.5. From Figure 2.6 it is clear that the high frequency noise caused by the 'miss modelling' of the short time (i.e., $\forall t \in]0, t_1[$) behaviour of the experimental data tends to spill over into the top of the experimental frequency range, with the moduli evaluated either via PCHIP or Makima adhering most to the exact solutions, especially at relatively low frequencies; whereas the Spline function performs worse over the whole frequency range. Interestingly, also in this case, for a given set of experimental data, there exists a threshold value of the SNR above which all the three interpolation functions allow an accurate estimation of the Fourier transform.

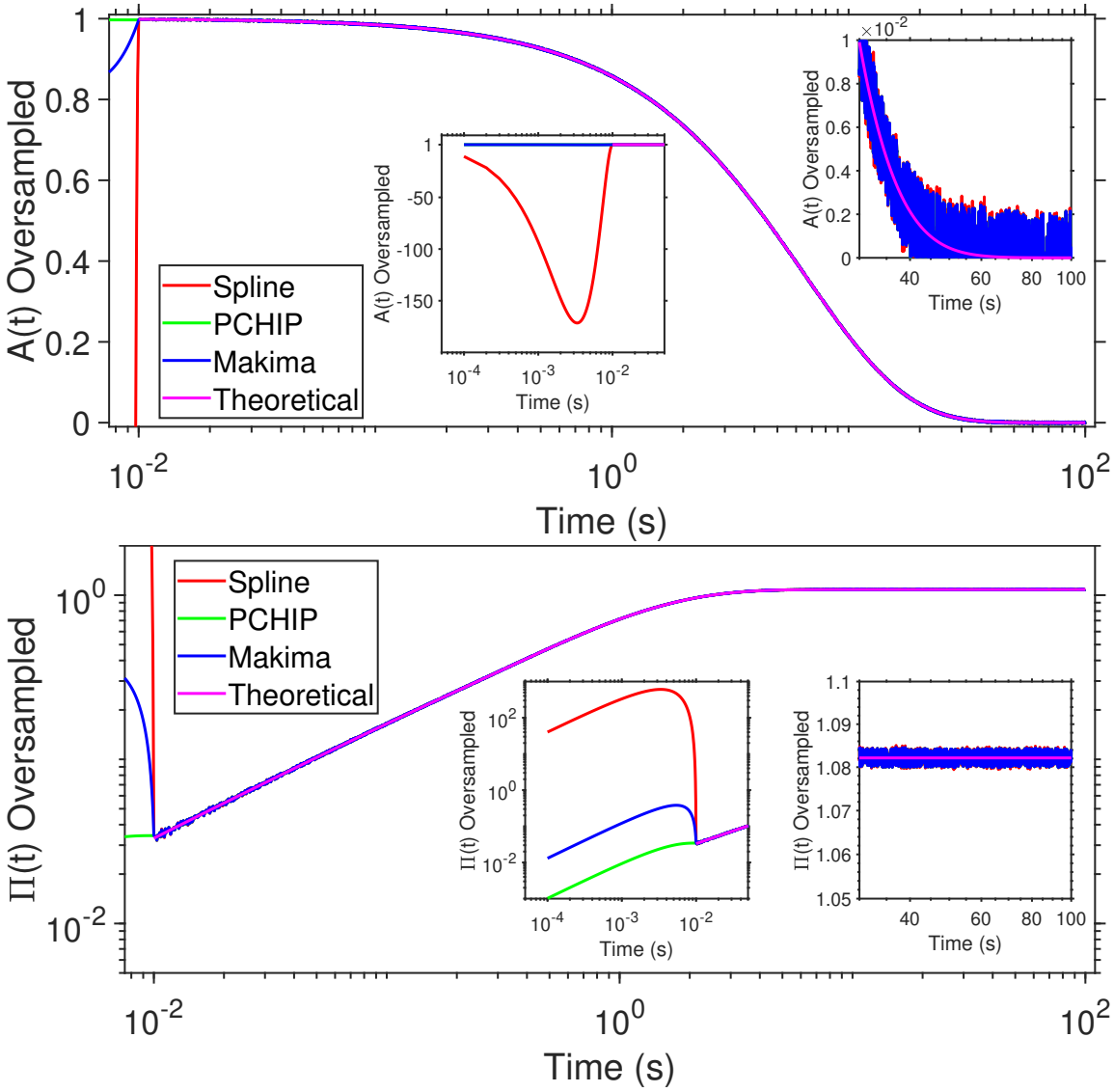

Figure 2.5: (Top) Equation (2.2) and (bottom) Equation (2.3) drawn as continuous (pink) lines by using 10^4 experimental points linearly spaced in time. A white noise having a SNR $= 50$ is added to the experimental data, which are then interpolated by means of three MATLAB built-in interpolation functions: Spline, PCHIP and Makima. The insets highlight the detrimental effects on the interpolation process due to the presence of noise, both at short and long time scales.

In order to identify the threshold value for each interpolation method applied to both Equations (2.2) and (2.3) (with DIP $= 1$), we have evaluated the MRAE of the transformed data (i.e., Equations (2.9)) as function of the SNR; with the latter ranging from 1dB to 350dB. The results are reported in Figure 2.7 for both the sampled functions shown in Figure 2.5. From Figure 2.7 top, it can be seen that at low values of SNR (i.e. $\lesssim 50$ dB) all of the interpolation functions perform poorly, with a MRAE as large as $10^8\%$ for the Spline interpolation function at SNR $= 0$; thus performing significantly worse than PCHIP and Makima.

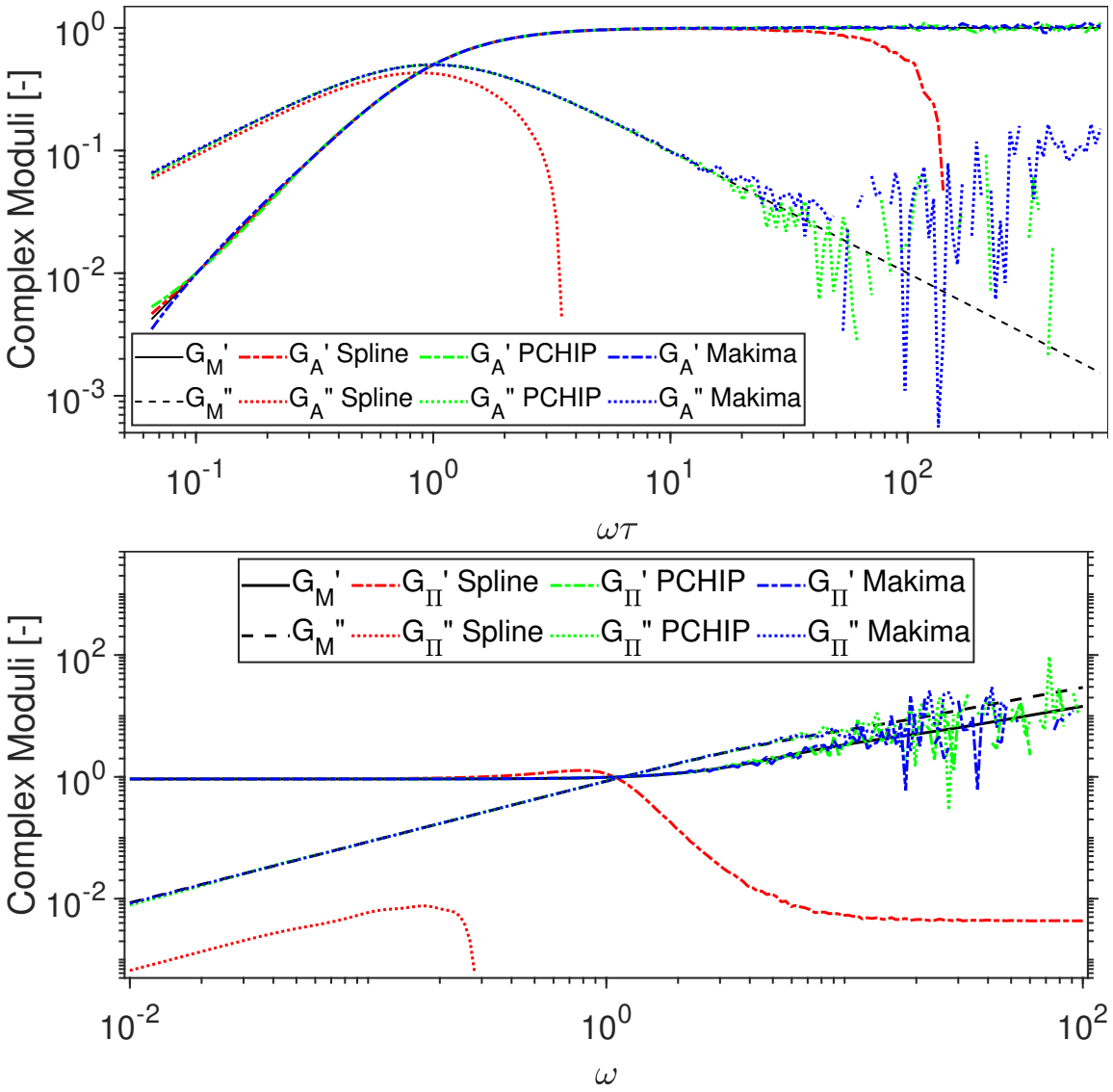

Figure 2.6: Comparison between the frequency-dependent complex moduli obtained via Equations (2.4) (top) and (2.5) (bottom) and those evaluated by Fourier transforming via Equation (2.1) the interpolations functions shown in Figure 2.5.

However, as one would expect, by increasing the SNR to a relatively high value (here above $\sim$ 170dB) the MRAEs of the moduli associated with each interpolation function fall below 1% and asymptotically approach the values presented in Figure 2.4 for DIP $= 1$. Interestingly, from Figure 2.7, one could argue that, in presence of noise, the interpolation processes performed by PCHIP and Makima work best, when compared to the Spline. However, in response it must be highlighted that, in real experiments, it is rare to process data with low SNR; such as those reported in the insets of Figure 2.5, where both the Equations (2.2) and (2.3) are drawn with a SNR $= 50$, which would commonly be discarded as 'noisy measurements'.

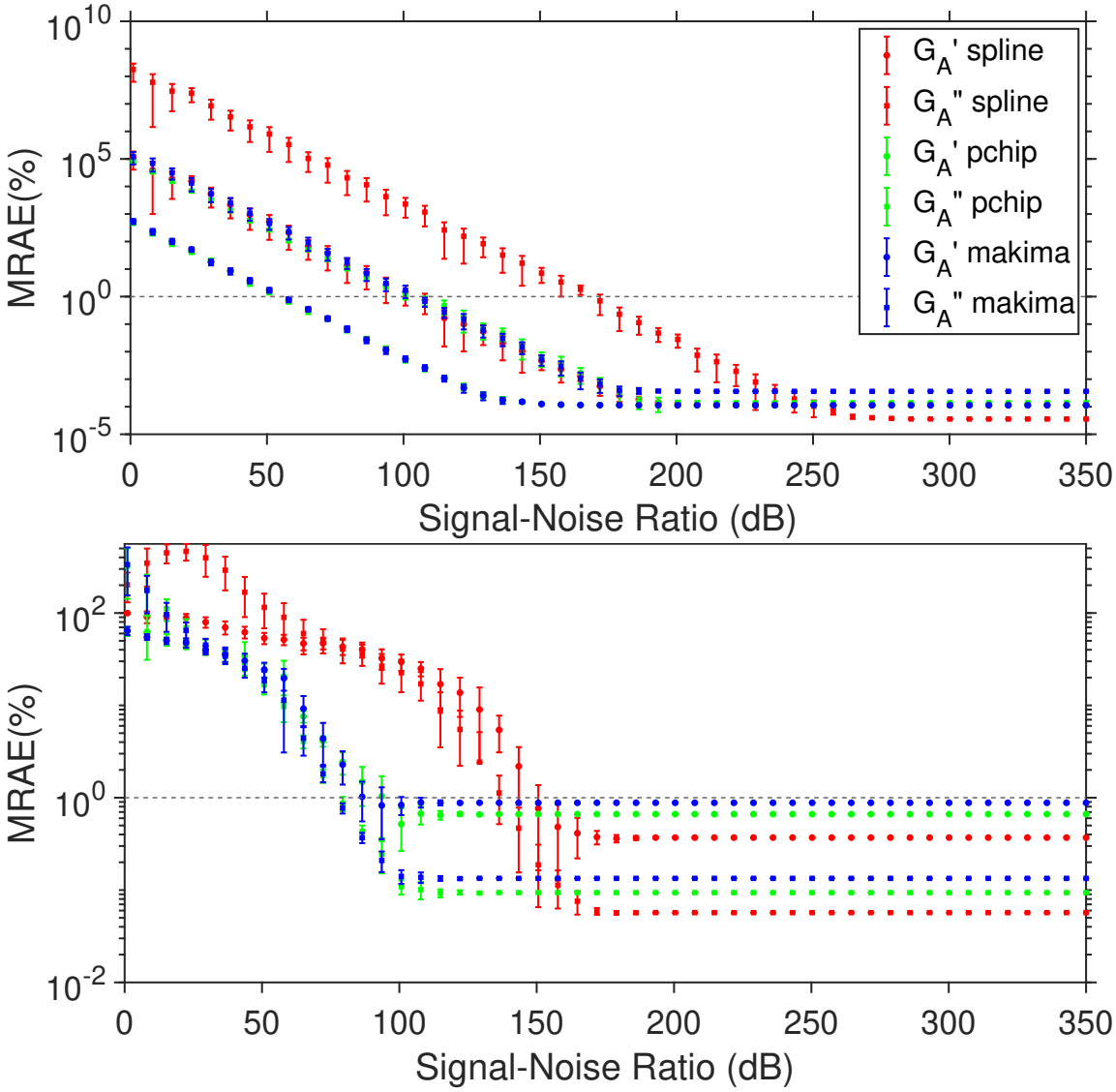

Figure 2.7: Mean relative absolute error (MRAE) of the frequency-dependent complex moduli determined by Fourier transforming (via Equation (2.1)) the interpolation functions shown in Figure 2.5 (top & bottom respectively) for SNR values ranging from 1dB to 350dB. The error bars represent one standard deviation of uncertainty calculated over ten repeats.

2.5 Conclusion

In this article we have presented an open-access code named i-RheoFT that allows to evaluate the Fourier transform of any generic time-dependent function that vanishes for negative times, sampled at a finite set of data points that extend over a finite range, and *need not* be equally spaced. The analytical method that underpins this code has been originally introduced by Evans & Tassieri [44, 61] in the form of an open-access LabVIEW executable specialised for the analysis of microrheology measurements performed with optical tweezers. Here we expand the range of its potential applications by implementing it into an open-

access MATLAB code, with the aim of reaching a broader audience and encouraging its exploitation in a variety of applications.

The effectiveness of i-RheoFT has been corroborated here by evaluating the Fourier transform of two generic functions having a known analytical expression of their Fourier transforms. Moreover, the analytical method has been tested as function of three important experimental parameters: (i) the 'density of initial experimental points' (DIP) describing the sampled function; (ii) the interpolation algorithm used to perform the "*virtual oversampling*" procedure introduced by Evans & Tassieri, which here is achieved by means of the following three built-in MATLAB functions: Spline, Makima and PCHIP; and (iii) the destructive effects on the expected outcomes due to the presence of (white) noise.

The outcomes of this study reveal that, at relatively high DIP values and signal-to-noise ratios, all three interpolation functions perform well in recovering the original information of the sampled function, with the Spline function always performing best. Whereas, by reducing *either* the number of initial data points *or* the signal-to-noise ratio, there exists a threshold value below which all three functions perform poorly, with the Spline function always returning the highest error of all three functions.

Therefore, we envisage that these results and i-RheoFT will be of particular interest and use to all those (experimental and simulation) studies where fast streams of acquired data are processed on-the-fly to build time-averaged functions, which are often defined by a finite number of data points over a limited time window spanning several decades; as for instance, in the cases of diffusing wave spectroscopy and dynamic light scattering measurements.

2.6 Acknowledgements

This work was supported by the EPSRC CDT in "Intelligent Sensing and Measurement" (EP/L016753/1). M.T. acknowledges support via EPSRC grant "Experiencing the micro-world - a cell's perspective" (EP/R035067/1 - EP/R035563/1 - EP/R035156/1).

2.7 Author Contributions

T.M. conceived the method. M.G.S. implemented the MATLAB code and performed the data analysis. M.G.S., G.M.G. and T.M. contributed writing the manuscript.

2.8 Additional Information

Competing financial interests: The authors declare no competing financial interests.

2.9 Appendix

The following appendix is the supplementary information available alongside the paper (through this link: `https://www.nature.com/articles/s41598-021-02922-8#additional-information`), which provides the MATLAB code used for i-RheoFT in addition to how to use it. In addition, screenshots of each open-source application have been provided.

2.9.1 MATLAB Script

In this section we report the MATLAB script that has been used in this work to evaluate the Fourier transform of two generic functions defined by Equations 2 and 3 in the main text, which are evaluated for a finite set of timestamps. A "readme" file is reported in the next section.

```
%% I-RheoFT: Fourier transforming sampled functions without
    artefacts.
% Authors: Matthew G. Smith, Graham M. Gibson & Manlio
   Tassieri
% University of Glasgow
% Date: 14/09/2020
% Aim: This program is designed to evaluate the Fourier
   transform (FT)
% of a generic function, sampled at a finite rate. It will
   produce the FT
% named GFT and the Complex modulus in the form G' and G"
   named gdata I.
% When the% script is run it will ask for the file name (.
   csv/.xlsx),
% the value of the function at time = 0 (g0), the gradient
   of the function
```

```
% at time=+infinity (ginf) and the interpolation function
   you wish to use
% (spline, makima or pchip). As recommended in the paper,
   if the function
% has a Density of Initial Points (DIP) of more than 0.35
   then the spline
% function should be chosen as this gives the lowest error.
% The oversampling (OverSample) and the number of frequency
    points
% (freqpoints) can be edited, although a significant
   increase in either
% could lead to longer run times.
%% Ask user for File, g0, g infinity and interpolation
   function
filename = input('Please input file name: ','s');
file = readtable(filename);
g0 = input('Please input g0: ');
ginf = input('Please input ginf: ');
InterpFunc = ...
input('Please input the Interpolation Function(spline,
   makima,pchip): ','s');
file = table2array(file);
t = file(:,1).';
g = file(:,2).';
t0 = 0;
Num_Init_Pts = length(t);
freqpoints = 200;
OverSample = 1e5*Num Init Pts;
%% Interpolation, Oversampling and Fourier transform
% Interpolation and Oversampling
t_I = linspace(t(1),t(end),OverSample);
Gint_I = interp1(t,g,t I,InterpFunc);
% Fourier Transform using function below
[GFT,gdata_I] = IRHEO GT(t_I,Gint_I,freqpoints,g0,ginf);
```

```
%% The Fourier Transform function
function [GFT,gdata_I] = IRHEO GT(t_I,Gint_I,freqpoints,g0,
   ginf)
gdata_I = zeros(freqpoints,3);
GFT = zeros(freqpoints,3);
wrange = logspace(-2,2,freqpoints); % Freqency Range
A = zeros(1,length(t_I)-1);
for n = 1:freqpoints
w = wrange(n);
for k = 2:length(t I)
A(k) = (((Gint_I(k)-Gint_I(k-1))/(t_I(k)-t_I(k-1)))*...
(exp(-i*w*t_I(k-1))-exp(-i*w*t_I(k))));
end
GFT1 = ((i*w*g0+((1-exp(-i*w*t_I(2)))*((Gint_I(1)-g0)/t_I
   (2)))+ ginf*exp(-i*w*t_I(end)))+sum(A))/(i*w)^2;
Gstar = GFT1*(i*w);
GFT(n,:) = [w real(GFT1) imag(GFT1)];
gdata_I(n,:) = [w real(Gstar) imag(Gstar)];
end
end
```

2.9.2 README

This is a MATLAB code that implements the analytical method originally introduced by Evans & Tassieri[44, 61], which allows to evaluate the Fourier transform of any generic timedependent function that vanishes for negative times, sampled at a finite set of data points that extend over a finite range, and need not be equally spaced. In particular this program has been designed to evaluate the Fourier transform of data fed in the form of a .csv/.xlsx file, while also giving the user the option to use any of the three interpolations functions described in the main manuscript.

Installation

The .m file to be installed is *iRheoFT.m*, which is written in MATLAB R2018b. It is recommended that the input data should be in a column format in a .csv or .xlsx file. Attention must

be paid to make sure that both the data and the .m file are in the same directory in MATLAB; otherwise the data file will not be found.

How to use?

Once the files have correctly been installed in the same directory of MATLAB, running the script will produce a series of prompts for the user to input. Firstly, it will ask the user to input the file name including the file type (.csv/.xlsx). It will then ask the user to input the value of the function at time 0 and then the value of the gradient of the function at time plus infinity. Finally, it will ask the user to input which interpolation method they would like to use (Spline, Makima or PCHIP) and this should be chosen depending on the Density of Initial Points (DIP) of the data analysed. The DIP can be calculated from Equation 6. One can also edit the Oversampling and the number of frequencies used, although the default values should be valid in most of the cases. Once the script has finished running, the Fourier transform of the function will be contained in the variable *GFT* and the Complex Modulus will be contained in the variable *gdata_I*.

Example Data

A possible starting point to make sure the program is working properly, would be to generate a single exponential decay function that takes the form of Equation 2. The relaxation time used in the manuscript is 6.5 sec, with 103 points logarithmically spaced in a time window ranging from 0.01 - 100 sec. The data should be saved as a .csv or a .xlsx file and loaded into the same directory of iRheoF T.m. In order to produce the viscoelastic moduli curves, one should plot the log-log of *gdata_I*, where column 1 is the frequency, column 2 is G' and column 3 is G''. The plot should be similar to Figure 3 (D), if this is the case then the code is working as intended.

2.9.3 Open-source Applications

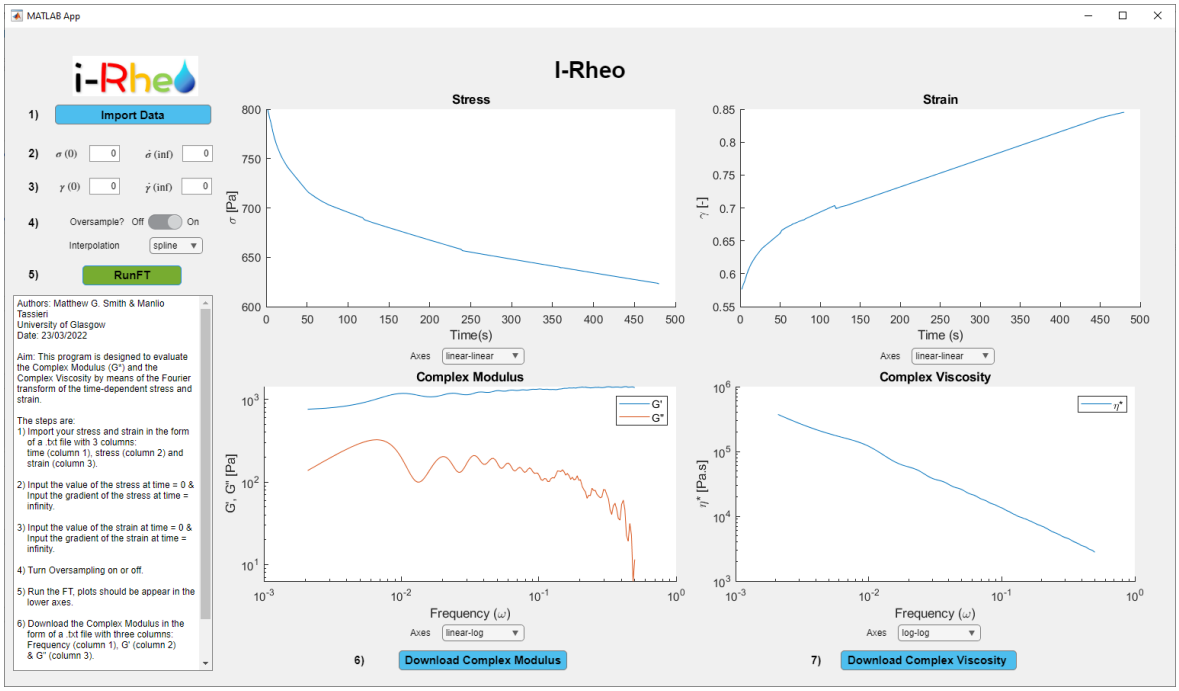

Figure 2.8: Screenshot from the open-source application "*I-Rheo*" developed from the work in "*i-RheoFT: Fourier transforming sampled functions without artefacts*". Available to download at [1]

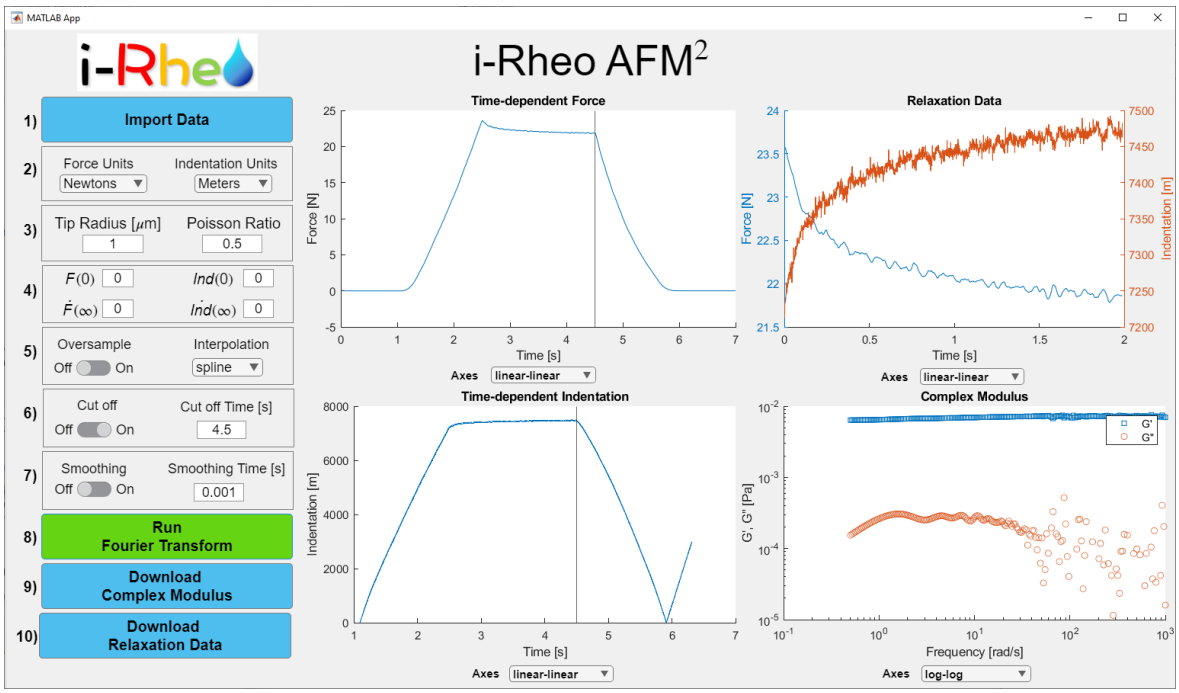

Figure 2.9: Screenshot from the open-source application "*I-Rheo AFM2*" developed from the work in "*i-RheoFT: Fourier transforming sampled functions without artefacts*". Available to download at [2]

Chapter 3

Machine learning opens a doorway for microrheology with optical tweezers in living systems

Matthew G. Smith [a], Jack Radford [b], Eky Febrianto [c], Jorge Ramírez [d], Helen O'Mahony [a], Andrew B. Matheson [e], Graham M. Gibson [b], Daniele Faccio [b], and Manlio Tassieri [a]

[a] Division of Biomedical Engineering, James Watt School of Engineering, University of Glasgow, Glasgow G12 8LT, U.K.

[b] School of Physics and Astronomy, University of Glasgow, Glasgow G12 8QQ, U.K.

[c] Glasgow Computational Engineering Centre, James Watt School of Engineering, University of Glasgow, Glasgow G12 8LT, U.K.

[d] Departamento de Ingeniería Química Industrial y Medio Ambiente, Universidad Politécnica de Madrid, José Gutiérrez Abascal 2,28006 Madrid, Spain

[e] School of Engineering and Physical Sciences, Institute of Biological Chemistry, Biophysics and Bioengineering, Heriot Watt University, Edinburgh, U.K.

Published: AIP Advances

Access: https://doi.org/10.1063/5.0161014 [70]

Author Declaration

I confirm that my contribution to this paper is over 50%.

3.1 Abstract

It has been argued that linear microrheology with optical tweezers (MOT) of living systems "*is not an option*", because of the wide gap between the observation time required to collect statistically valid data and the mutational times of the organisms under study. Here, we have exploited modern machine learning (ML) methods to reduce the duration of MOT measurements from tens of minutes down to one second, by focusing on the analysis of computer simulated experiments. We explicate for the first time in literature the relationship between the required duration of MOT measurements (T_m) and the fluids relative viscosity (η_r) to achieve an uncertainty as low as 1% by means of conventional analytical methods; i.e., $T_m \cong 17\eta_r^3$ minutes. Thus, revealing why conventional MOT measurements commonly underestimate the materials' viscoelastic properties, especially in the case of high viscous fluids or soft-solids. Finally, we have developed and corroborated by means of real experimental data a ML algorithm to determine the viscosity of Newtonian fluids from trajectories of only one second in duration, yet capable of returning viscosity values carrying an error as low as $\sim 0.3\%$ at best; hence the opening of a doorway for MOT in living systems.

3.2 Introduction

Since their first appearance in the 1970s [32, 71, 72], Optical Tweezers (OT) have been employed as extremely sensitive force transducers across a variety of disciplines within the *Natural Sciences* [33–38]. OT rigs rely on the ability of a highly focused laser beam to optically trap in 3D micron sized dielectric particles suspended in a fluid. This is achieved by optically guiding a monochromatic laser beam through a microscope objective with a high numerical aperture. Once trapped, the particle experiences a quadratic potential and therefore a restoring force that is linearly proportional to the distance of the particle from the trap centre; with a constant of proportionality of the order of a few μN/m. It follows that by measuring the particle position to a high spatial resolution (i.e., of a few nm), scientists have successfully measured forces as low as a few pNs, such as those generated by the thermally driven motion of water molecules [73] or those exerted by single motor proteins [74]. Interestingly, accessing particles' trajectory to high temporal and spatial resolutions is one of the requirements underpinning microrheology techniques [75, 76], as elucidated in this paper for the specific case of Optical Tweezers.

Microrheology is a branch of rheology (the study of the flow of matter) and is focused on the characterization of the mechanical properties of complex materials by performing mea-

surements at micron length scales, often with sample volumes as little as a few microlitres, or even within living cells [77]. This offers an indisputable advantage over classical bulk rheology techniques, which require millilitres of sample, especially in biophysical studies where samples are often rare and/or precious and come in small quantities (e.g., a few microlitres). Microrheology techniques are categorised as either 'passive' or 'active' depending on whether the motion of the tracer particles is thermally driven or induced by an external force field, respectively. Interestingly, optical tweezers is one of such techniques that can be defined as a *hybrid* microrheology tool [78], because of the quadratic nature of the optical potential constraining the motion of the probe particle. Indeed, despite the tracer particles being optically trapped (within the focal plane of a microscope), at short time scales (i.e., for small displacements) the restoring force exerted on the probe is weak enough for the particle to experience Brownian motion because of the thermal fluctuations of the molecules of the suspending media. Nonetheless, active microrheology with OT is still possible by driving the trapping laser, often in a sinusoidal pattern as elucidated within References [79, 80]. However, as we shall further corroborate in this work, a necessary condition for executing either passive or active linear MOT measurements is to perform "*sufficiently*" long measurements, commonly of the order of tens of minutes [24, 80]. This is because most of the analytical methods used to determine the materials' viscoelastic properties are underpinned by statistical mechanics principles, whose accuracy relies on the analysis of a *significant* number of independent readings. Therefore, as pointed out by Tassieri [80], it may not be appropriate to adopt MOT for studies involving living systems, as biological processes occur at time-scales ranging from 10^{-2} to 10^{2}sec [81–84], and therefore the viscoelastic properties of biological systems may not be considered time-invariant during the measurements.

Hence, the aim of this work is to exploit modern Machine Learning (ML) methods to reduce the duration of MOT measurements and thus allow scientists to perform microrheology measurements in living systems. In order to achieve such a challenging aim, in this work, we have taken a first step towards a possible solution of the problem by focusing initially on the analysis of computer simulated trajectories of an optically trapped particle suspended within a set of Newtonian fluids having viscosity values spanning three decades, i.e. from 10^{-3} to 1 Pa·s, before looking at some experimentally obtained trajectories. The goal was to develop a ML algorithm that would effectively estimate fluids' viscosity from relatively short measurements ($\leq$ 1sec) and compare the outcomes with those obtained by analysing the same set of data with conventional methods based on statistical mechanics principles [24, 43, 44, 85]. Notably, this study has led to the following key findings: (i) we corroborate the requirement

for MOT studies to perform "*sufficiently*" long measurements when using conventional analytical methods for data analysis and (ii) we provide, for the first time in literature, a means for estimating the required duration of the experiment to achieve an uncertanty as low as 1%; (iii) we provide evidence explaining why conventional MOT measurements commonly underestimate the materials' viscoelastic properties, especially in the case of high viscous fluids or soft-solids (e.g., gels and cells); (iv) we have developed a ML algorithm that uses feature extraction on only 'one second' of trajectory data to determine the viscosity of Newtonian fluids; yet capable of returning viscosity values carrying an error as low as $\sim 0.3\%$ at best and of $\sim 7\%$ at worst, which is five times smaller than those obtained from conventional analytical methods applied to the same data.

3.3 Theoretical Background

3.3.1 Passive Microrheology with Optical Tweezers

Passive MOT is typically performed by means of a stationary optical trap that confines in 3D a spherical particle suspended in a fluid of unknown viscoelastic properties. At thermal equilibrium, the Brownian motion of the probe particle is caused by the thermal fluctuations of the fluids' molecules and it is monitored by means of a high speed motion detection device. The particle trajectory is typically extracted in 2D, as the one shown in Fig. 3.1(B-C). Notably, a statistical mechanics analysis of the particle's trajectory can return not only the trap stiffness of the OT, but also a good estimation of the frequency-dependent viscoelastic properties of the suspending fluid [24, 43–45, 51, 85, 87, 88]. The latter can be evaluated by solving a generalised Langevin equation as the following one:

$$m\vec{a}(t) = \vec{f}_R(t) - \int_0^t \xi(t-\tau)\vec{v}(\tau)d\tau - \kappa\vec{r}(t), \tag{3.1}$$

where m is the mass of the particle, $\vec{a}(t)$ is its acceleration, $\vec{v}(t)$ is its velocity, $\vec{r}(t)$ is its position, $\vec{f}_R(t)$ is the Gaussian white noise term used for modelling the stochastic thermal forces, and $\xi(t)$ is the generalised time-dependent memory function accounting for the viscoelastic nature of the fluid [89]. The convolution integral represents the time-dependent friction force exerted by the complex fluid onto the particle. The term $\kappa\vec{r}(t)$ is the restoring force of the optical trap, when the confining field $E(\vec{r})$ exerted by the optical tweezers is assumed to have an harmonic form:

$$E(\vec{r}) = \frac{1}{2}\kappa\vec{r}^2, \tag{3.2}$$

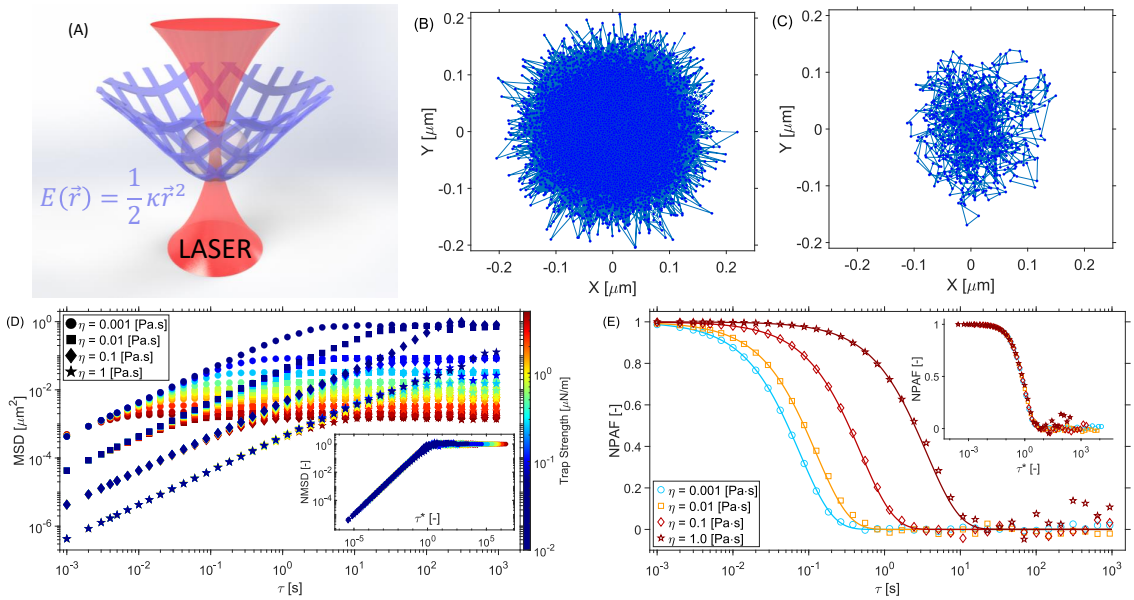

Figure 3.1: (A) A schematic representation of an optically trapped bead within a harmonic potential, $E(\vec{r})$, where κ is the trap $\vec{r}(t)$ is the bead position from the trap centre. (B-C) Two examples of 2D trajectories of an optically trapped bead of radius of 1μm suspended in water for 1024s (B) and for 1s (C). Both trajectories were generated by means of a MATLAB code adapted from the one developed by Volpe [86]. (D) The mean square displacement (MSD) curves of a series of 48 simulated trajectories of 1024 sec duration and acquired at a 1 kHz of an optically trapped particle experiencing constraining forces ranging from 0.01 to 5 μN/m (see colour bar) and suspended into four different Newtonian fluids having viscosity values spanning three orders of magnitude (see legend). The inset shows the same data as in the main, but with the ordinate axis normalised by the twice the variance of the particle trajectory and the abscissa τ replaced by the dimensionless lag-time τ^*, as elucidated in the body of the manuscript. (E) Four examples of normalised position autocorrelation functions (NPAF, symbols) of a particle suspended in four Newtonian fluids having viscosity of 10^{-3}, 10^{-2}, 0.1, 1Pa·s and experiencing constraining forces of 0.25, 1.5, 4, 5μN/m (from left to right and colour coded as for the colour bar in D), respectively. The lines are single exponential decay functions $A(\tau) = e^{-\lambda\tau}$ drawn with $\lambda = \kappa/(6\pi\eta a)$ evaluated by using the input (nominal) parameters mentioned above; i.e., $\lambda = 13.26$, 7.96, 2.12 and 0.27Hz, respectively. The inset shows the same data as in the main (symbols only), but the abscissa has been replaced by $\tau^* = \lambda\tau$.

where κ is the trap stiffness and $\vec{r}(t)$ is the particle position from the trap centre. Interestingly, in the case of Newtonian fluids (i.e., for purely viscous fluids with constant viscosity η) and at low Reynolds numbers (i.e., $Re << 10$ for which the inertia term can be neglected; notice

that, in our experiments the highest Reynolds number is achieved at the highest frequency, which returns a value on the order of 10^{-3}), Equation (3.1) simplifies as follows [86]:

$$\vec{W}(t)\sqrt{2k_BT\gamma} = \gamma\vec{v}(t) + \kappa\vec{r}(t), \tag{3.3}$$

where the term on the left side represents the fluctuating force due to random impulses from many neighboring fluid molecules, $\gamma = 6\pi\eta a$ is the friction coefficient, a is the particle radius, k_B is the Boltzmann's constant, and T is the absolute temperature. In this work, Equation (3.3) has been adopted to generate (thousands of) 2D trajectories of optically trapped particles suspended into a set of Newtonian fluids having different viscosity values for machine learning purposes, as explained in the following sections.

In the general case, i.e. for any generic complex fluid, it has been shown [43–45] that Equation (3.1) can be solved for the fluids' complex shear modulus ($G^*(\omega)$) in terms of either the particle normalised mean squared displacement (NMSD), $\Pi(\tau)$, or its normalised position autocorrelNPAF), $A(\tau)$; which are both drawn in the insets of Figure 3.1(D, E) for some of the cases studied in this work. Notably, these two functions are simply related to each other and their expressions are:

$$\Pi(\tau) = \frac{\langle \Delta r^2(\tau)\rangle_{t_0}}{2\langle r^2\rangle_{eq.}} \equiv \frac{\langle [r(t_0+\tau) - r(t_0)]^2\rangle_{t_0}}{2\langle r^2\rangle_{eq.}} = 1 - A(\tau), \tag{3.4}$$

where τ is the lag-time ($t - t_0$) and the brackets $\langle ... \rangle_{t_0}$ represent an average over all initial times t_0. The relationship between the above two time-averaged functions and the time-invariant fluids' complex shear modulus is:

$$G^*(\omega)\frac{6\pi a}{\kappa} = \left(\frac{1}{i\omega\hat{\Pi}(\omega)} - 1\right) \equiv \left(\frac{1}{i\omega\hat{A}(\omega)} - 1\right)^{-1} \equiv \frac{\hat{A}(\omega)}{\hat{\Pi}(\omega)}, \tag{3.5}$$

where $\hat{\Pi}(\omega)$ and $\hat{A}(\omega)$ are the Fourier transforms of $\Pi(\tau)$ and $A(\tau)$, respectively. The inertial term ($m\omega^2$) present in the original works[43, 45] has been here neglected, because for micron-sized particles it only becomes significant at frequencies of the order of MHz.

Notably, in the case of Newtonian fluids, the above equations simplify significantly and the relationship between the fluids' viscosity and the particle trajectory reads as follows:

$$\Pi(\tau) = 1 - A(\tau) = 1 - e^{-\lambda\tau}, \tag{3.6}$$

where $\lambda = \kappa/(6\pi\eta a)$ is the characteristic relaxation rate (also known as the "*corner frequency*"[42]) of the compound system OT *plus* fluid. Moreover, it has been shown [85] that by plotting $\Pi(\tau)$ and $A(\tau)$ versus a dimensionless lag-time $\tau^* = \tau\lambda$, all the curves having different values of η would collapse onto a master curve, as shown in the insets of Figure 3.1

(D) and (E), respectively. It follows that, for Newtonian fluids it is a straightforward step to determine their viscosity by analysing the temporal behavior of the NPAF [85]. In particular, by plotting the natural logarithm of $A(\tau)$ versus τ, one would obtain a straight line having a slope equal to $-\lambda$, from which the viscosity could be determined by means of a simple linear fit. In this work the fitting procedure has been constrained to the ordinate values ranging from 0 and -1 (equivalent to $A(\tau) = 1$ and $A(\tau) = e^{-1}$, respectively) to minimize the error, as discussed hereafter.

3.4 Methods

3.4.1 Simulation of particle trajectories

In order to train and test the machine learning algorithm discussed in the next section, we have used Equation (3.3) to generate thousands of trajectories by means of a MATLAB code adapted from the one developed by Volpe [86], which is able to simulate a 2D trajectory of an optically trapped particle suspended into a Newtonian fluid. The input parameters of the code were the trap stiffness, the viscosity, the temperature, the particle radius, the acquisition rate and the number of individual readings required. For instance, in Figure 3.1 are shown two examples of trajectory having the same input parameters, but duration of 10^3s in (B) and 1s in (C).

Moreover, in order to investigate the impact of the measurements duration on the outcomes obtained from both the conventional and the ML enhanced MOT approaches, we generated a set of particle trajectories suspended into four different Newtonian fluids having viscosity values of 10^{-3}, 10^{-2}, 0.1 and 1 Pa·s, respectively; and trap strengths ranging from 0.01 to 5 μN/m. These trajectories were simulated for 1024 sec at an acquisition rate of 1 kHz, which is equivalent to a real measurement of circa 17 minutes in duration. Notably, due to their stochastic nature, it is possible to split each of these trajectories into shorter ones of variable duration, down to 0.05 sec. All these trajectories were analysed to calculate the fluids' viscosity by means of Equation (3.6), and the mean absolute percentage error (MAPE) of the outcome was calculated for each trajectory by means of the following equation:

$$MAPE = \frac{100}{N_{traj}} \sum_{i=1}^{N_{traj}} \left| \frac{\eta_i - \eta_{0i}}{\eta_{0i}} \right|, \tag{3.7}$$

where N_{traj} is the number of trajectories for a given duration, η_0 is the nominal viscosity value (used as input in the simulations) and η is the measured one.

3.4.2 Optical tweezers rig

Experimental measurements were performed by using an OT system based on a continuous wave, diode pumped solid state (DPSS) laser (Ventus, Laser Quantum), which provided up to 3 W at $1,064$ nm. A nematic liquid crystal spatial light modulator (SLM) (BNS, XY series 512×512) was used to create and arrange the desired optical trap. The laser entered a custom-made inverted microscope that uses a microscope objective lens (Nikon, 100x, 1.3 NA) to both focus the trapping beam and to image the thermal fluctuations of 4.74μm diameter silica beads (Bangs Laboratories), at room temperature $\sim 20^o$C. Samples were mounted on a motorized microscope stage (ASI, MS-2000). A complementary metal-oxide semiconductor (CMOS) camera (Dalsa, Genie HM 1024 GigE) acquired high-speed images of a reduced field-of-view. These images were processed in real-time at up to ~ 3 kHz to calculate the center of mass of the bead by using a particle tracking software developed in LabVIEW (National Instruments), running on a standard desktop PC [90, 91].

3.4.3 Machine Learning architecture

In fluid mechanics, machine learning (ML) has been widely used to translate observational and experimental data into knowledge about the underlying physics of the fluid [92]. Depending on the information being used for learning, ML algorithms can be categorised into supervised, semisupervised, and unsupervised. In this work we consider a supervised ML algorithm where the input (i.e., the particle trajectories) and the respective output (i.e., the viscosity) are used during learning. Specifically, we consider feed-forward neural networks (NNs), or multilayer perceptrons [93, 94], as the nonlinear function approximations between the input and output. The standard feed-forward NNs passes the input information through a network of hidden units and activation functions to produce the prediction. Deep Neural Networks (Deep NN) [95, 96] obtains a nonlinear approximation through the composition of multiple hidden layers. To obtain the unknown network weights, nonlinear optimisation methods, such as backpropagation [97], are used by minimising the discrepancy between the predictions and the known training outputs.

In this paper, we sidestep the conventional method (i.e., Equation (3.6)) of estimating fluids' viscosity from the trajectories of optically trapped particles by means of supervised ML. The training dataset consists of $100,000$ particle trajectories, each of 10s duration, for different fluids' viscosity. In order to cover the range of explored viscosity (i.e., from 0.001 to 1 Pa·s), the viscosity values are randomly sampled from a log-uniform distribution

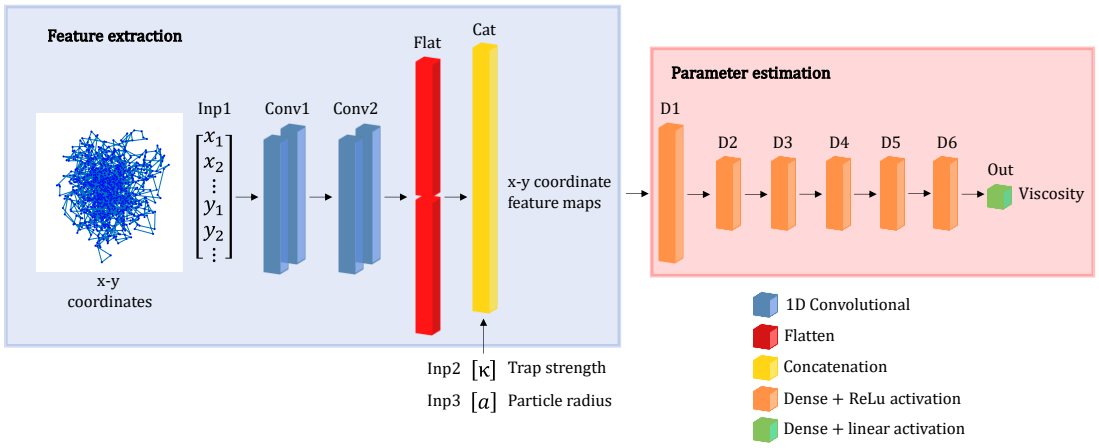

Figure 3.2: A schematic representation of the machine learning architecture used in this work. A single particle trajectory of x-y coordinates is transformed and preprocessed for feature extraction. The output of which is concatenated with the trap strength (κ) and the particle radius (a). This is used as the input for parameter estimation with a single output node of viscosity. *Author Declaration: This figure was designed by Jack Radford* [b]

ranging from 0.0008 to 1.2 Pa·s. Similarly, the trap strengths are randomly sampled from a uniform distribution ranging from 0.08 to 0.39 μN/m. Prior to the training, each trajectory coordinate input is normalised and flattened into a one-dimensional array. The normalisation, i.e., subtracting the coordinates by their initial position, makes sure that there is no significant shift between the $x-$ and $y-$ component in the flattened array. Therefore, the flattening will have minimum effect on the trajectory's temporal correlation. Moreover, we also consider in this work shorter observation times of the trajectories, i.e., $T_m = \{1\text{s}, 0.5\text{s}, 0.1\text{s}, 0.05\text{s}\}$, which are obtained through subdivision of the original 10s datasets.

Figure 3.2 shows a schematic representation of the ML architecture used in this study, consisting of two blocks, i.e., feature extraction and parameter estimation. The one-dimensional input, obtained by flattening the coordinates, is first processed through the feature extraction block, which comprises one-dimensional convolutional neural network (CNN) layers [98, 99]. These CNN layers serve as convolution operator that enhance the local temporal structures present in the particle trajectories. In this study, two CNN layers are employed to eliminate the randomness of particle motion and highlight important features encoded in the trajectory. While it is possible to add more convolutional layers, we found that two layers are sufficient for the Newtonian fluid case. In each CNN layer, two filters with the same kernel width are used to increase the chances of identifying various features in the data. The filter widths are 10 and 100 for the first and second layers, respectively, which

correspond to 0.01s and 0.1s in the particle trajectory. The width increase in the second layer allows for filtering random motion with longer periods. Note that, for observation time $T_m = 0.1$s and $T_m = 0.05$s, the second convolutional layer filter sizes were adjusted, due to the shorter vector lengths, to be 50 and 25, respectively. The resulting 'feature maps' are transformations of the input data into latent variables which highlight important information for the task of estimating viscosity.

The feature maps are then concatenated, along with the trap stiffness and particle radius, to a 1D vector and passed to the parameter estimation block to predict the viscosity. The concatenation of additional variables is crucial to discriminate between fluids which have different viscosity, but similar particle trajectories due to other dependant variables (e.g., trap stiffness and particle radius). Neural networks are known to be universal approximators [93], and deeper layers often lead to a more expressive mapping or approximation. The number of layers and neurons is selected based on Occam's razor principle [100] to ensure generalisability and prevent overfitting. In this study, we identified that six fully-connected dense layers provided a good estimate of viscosity. Each neuron in the hidden layers uses a ReLu (rectified linear unit) activation function, while a linear activation function is used in the output layer. The loss function was chosen to be the mean absolute percentage error (MAPE) to prevent bias in training towards minimising losses for high viscosity values with larger residuals. The hyper-parameters of the model including the batch size, learning rate, number of epochs and validation split were 256, 10^{-5}, 200 and 0.1, respectively. The training has been performed in triplicate for each model with input trajectories having interval T_m from 0.05 to 1 seconds, using an Adam optimizer [101], and was performed on a desktop PC equipped with an 18-core Intel i9-10980XE CPU (3GHz), 256GB RAM and an NVIDIA GeForce RTX 3090 with 24GB memory. The training time for each ML model increased with decreasing input length due to the increasing number of training examples so each model took from $2.5-6.5$hrs to train depending on input trajectory.

3.5 Results

One of the key features and advantages of using optical tweezers for microrheology purposes is that they can be easily calibrated without the use of external transducers. Indeed, as we shall discuss hereafter, it has been assumed [24, 43–45, 85, 87, 88] that the trap stiffness of symmetric OT can be determined to a high accuracy by appealing to the principle of

equipartition of energy:

$$\frac{d}{2}k_BT = \frac{1}{2}\kappa\langle\vec{r}^2\rangle_{eq.}, \tag{3.8}$$

where d is the dimension of the motion. This is true as long as the measurement time is "*sufficiently*" longer than the characteristic time τ_{OT} of the compound system made of OT (i.e., its trap stiffness), fluid (i.e., its compliance) and bead (i.e., its radius taken as a characteristic length of the probe), which is not known *a priori* in rheological investigations of complex materials.

However, in the case of Newtonian fluids and operational condition of the instrument within the micro length- and time-scales, as mentioned earlier, the compound system has a single characteristic time defined as $\tau_{OT} = \lambda^{-1}$, which can be used as a reference to estimate the minimum measurement duration required to properly calibrate the trap stiffness. In particular, by defining the duration of a measurement (T_m) as the ratio between the total number of readings (N) and the acquisition rate ($f = samples/s$) of the detector used for tracking the particle position, one could define a Deborah number [102] for optical tweezers (De_{OT}) as:

$$De_{OT} = \frac{\tau_{OT}}{T_m} = \frac{6\pi\eta af}{N\kappa}, \tag{3.9}$$

which can be further differentiated into "*nominal*" ($De_{OT,Nom.}$) and "*effective*" ($De_{OT,Eff.}$), depending on whether the trap stiffness used for determining λ is the nominal value set as input in the simulation code generating the trajectories or the measured one by means of Equation (3.8), which is affected by T_m as demonstrated hereafter.

In Figure 3.3–(A) we report the ratio between the two Deborah numbers *versus* $De^{-1}_{OT,Nom.}$ for a series of 528 simulated trajectories of variable duration of an optically trapped particle experiencing various constraining forces and suspended in four different Newtonian fluids having viscosity values spanning three orders of magnitude. Interestingly, the ordinate of such a diagram is equivalent to the ratio between the two trap stiffness $\kappa_{Nom.}/\kappa_{Eff.}$, while the abscissa is proportional to the measurement duration T_m. From Figure 3.3–(A) it is apparent the existence of a crossover value of $De_{OT,Nom.} \sim 1$ delimiting two operating ranges of OT rigs, i.e.: (i) for $De^{-1}_{OT,Nom.} >> 1$, the trap stiffness is determined to a high accuracy via Equation (3.8); whereas, (ii) for $De^{-1}_{OT,Nom.} << 1$, the constraining force is *undetermined*; or more specifically, $\kappa_{Eff.}$ is *overestimated* as often happens in many real experiments for which T_m is not sufficiently long. Based on Equation (3.5), it follows that when the trap stiffness is *overestimated* the outcomes of MOT measurements are *underestimated*, especially when they are attempted in high viscous fluids or soft-solids (e.g., gels and cells) [104, 105]. Our findings are further corroborated by the data shown in Figure 3.3–(B), where the

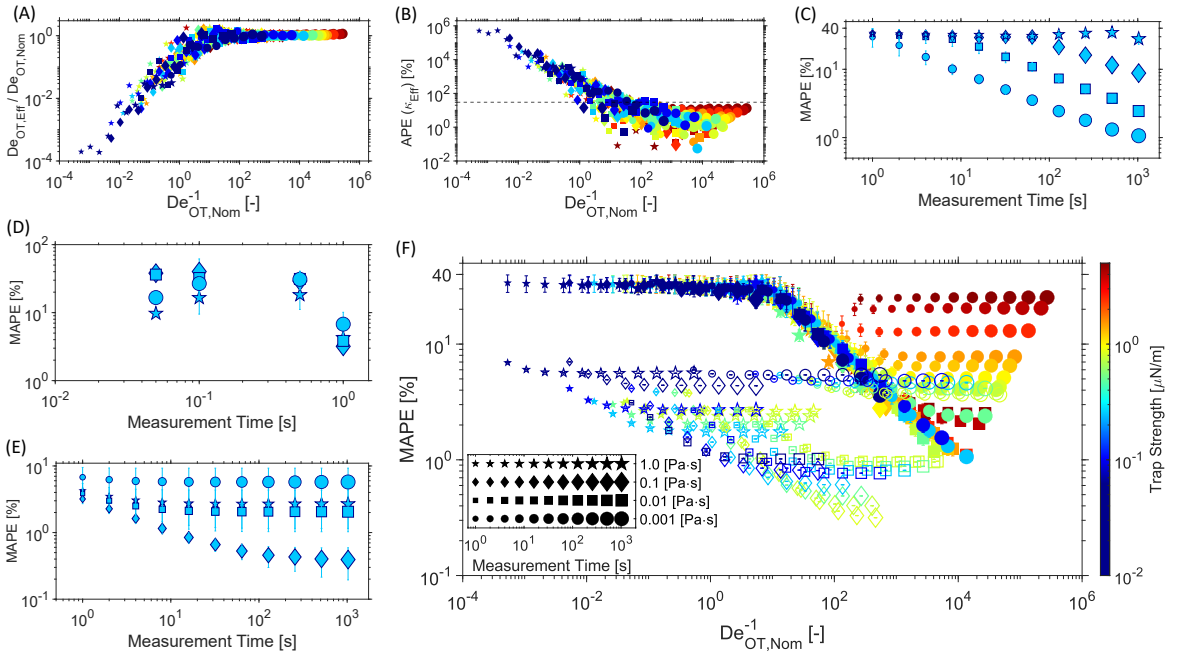

Figure 3.3: (A) The ratio between the effective Deborah number for optical tweezers $De_{OT,Eff.}$ $De_{OT,Eff.}$ and the nominal one $De_{OT,Nom.}$ $De_{OT,Nom.}$ *versus* $De^{-1}_{OT,Nom.} \propto T_m$ for a series of 528 simulated trajectories of different duration of an optically trapped particle experiencing various constraining forces and suspended into four different Newtonian fluids having viscosity values spanning three orders of magnitude. (B) The absolute percentage error (APE) of $\kappa_{Eff.}$ *vs.* $De^{-1}_{OT,Nom.}$ for the same set of trajectories as in (A). The line indicates an APE value of 30%, as reported in Ref.[103]. (C–E) The mean absolute percentage error (MAPE) of viscosity *vs.* measurement duration (T_m) determined (C) by using the conventional analytical method described in the body of the manuscript; (D) by averaging the prediction error from ML algorithms with different input dimensions; (E) by averaging the predictions of the three models with 1s input dimension. (F, closed symbols) The MAPE of viscosity *vs.* $De^{-1}_{OT,Nom.}$ evaluated from the conventional approach applied to the same set of trajectories used in (A). (F, open symbols) The MAPE of the optimal ML algorithm with an input measurement time of 1s. The colour bar indicates trap stiffness used during the generation of the trajectories. The size of the symbols scales with the measurement time as shown in the inset of (F).

absolute percentage error (APE) of $\kappa_{Eff.}$ is reported against $De^{-1}_{OT,Nom.}$ and compared with the experimental results (i.e., the horizontal line) reported by Matheson *et al.* [103], representing the threshold value of the APE of $\kappa_{Eff.}$ below which microrheology measurements performed with OT return an APE of the fluids' viscosity lower than circa 5% (see Figure 5 of Ref.[103]). It follows that, based on a conservative approach, one could argue that only

for $De_{OT,Eff.} \leq 0.001$ an accurate calibration could be achieved; which implies a minimum measurement duration of $T_m \geq 1000 \times \tau_{OT}$ for a given system. For instance, in the case of two measurements both performed at room temperature (i.e., $T = 20^o$C) with a bead of 1μm in radius and a trap stiffness of $\kappa = 2\mu$N/m, but one in water (with $\eta = 0.001$Pa·s) and the other in a fluid having a viscosity thousand times higher than water (e.g., glycerol), the characteristic times of the two compound systems would be $\tau_{OT} \cong 0.01$s and $\tau_{OT} \cong 10$s, respectively. It follows that, in order to achieve an accurate calibration of the OT (i.e. for $De_{OT} \leq 0.001$), the measurements should last at least 10s and 2.78hrs, respectively.

At this point it is important to highlight that optical tweezers rigs are commonly equipped with either a camera or a quadrant photodiode (QPD) device for tracking the particle position to a high acquisition rate, often operating at KHz or MHz, respectively. It follows that, when microrheology measurements are performed on materials with a higher viscous character than water, significantly longer measurements would be required, and therefore rigs equipped with either a QPD or an ultra high-speed camera would be more prone to be miscalibrated. This is because they are often equipped with an insufficient capacity of random access memory (RAM) to process the high–volume of data (of several MB/s) generated during the particle tracking procedure (of possible duration of $T_m = 10^4$s, which would result in $>$ 10 GB RAM occupancy); thus, they either crash or, in order to avoid this, measurements are stopped early causing a $De_{OT} >> 1$. A possible solution to avoid memory clogging, but not the lengthiness of measurements, is achieved by equipping the rig with an online digital correlator, which allows the machine to process high-volume data streams and to compress the relevant information in real-time, thus minimising the use of RAM [106, 107].

Let us now investigate how T_m affects the evaluation of the fluid viscosity when it is determined using a conventional method. In particular, as introduced earlier, in the case of Newtonian fluids it is a straightforward step to determine their viscosity by performing a linear fit of $Ln\big[A(\tau)\big]$ vs. τ, which here is executed for ordinate values ranging from 0 and -1 (equivalent to $A(\tau) = 1$ and $A(\tau) = e^{-1}$, respectively) to minimize the error. In Figure 3.3–(C) we report the mean absolute percentage error of the fluids' viscosity evaluated as mentioned above *versus* the measurement duration, which varies from 1s to 1024s. The simulated trajectories were generated for optically trapped particles suspended into four fluids having viscosity spanning three orders of magnitude (i.e., from 0.001 to 1Pa·s), but with all the other inputs having the following values: trap stiffness of 0.25μN/m, particle radius of 1μm, constant temperature of 19^oC and acquisition rate of 1kHz. From the diagram it can be seen that, for short measurement duration (i.e., at $T_m = 1$s) all the measurements return an

error as high as circa 33%; whereas, as the length of the measurement increases, the MAPE decreases down to a remarkable value of only 1% at $T_m = 1024$s for the fluid with the lowest viscosity value of 0.001Pa·s; whereas, for the other fluids it would have required significantly longer measurements to reach a similar accuracy, as elucidated hereafter. Notably, when the same data shown in Figure 3.3–(C) are drawn against $De^{-1}_{OT,Nom.} \propto T_m$, all the four curves collapse onto a master curve as shown in Figure 3.3–(F) (closed symbols), together with the outcomes obtained from the same analysis as the one described above, but applied to all the 528 simulated trajectories mentioned earlier. Thus, corroborating the concept introduced earlier that "*the higher the fluid's viscosity, the longer the measurement must be*". Moreover, from Figure 3.3–(F) it can be seen that, at relatively low trap strengths, the MAPE of the viscosity decreases as the T_m increases (i.e., for $De^{-1}_{OT,Nom.} >> 1$). However, at relatively high trap strengths, the error increases again, becoming almost independent by the duration of the measurement. Notably, this phenomenon can be explained in terms of the relative value assumed by the time-dependent fluid's shear compliance ($J(t)$) to that of the 'complex' system ($J_{cs}(t)$) composed by (i) the OT (whose contribution is purely elastic; i.e., κ), (ii) the viscoelastic fluid (whose contribution relies on its elastic and viscous components) and (iii) the particle radius a (which defines a characteristic length scale). In particular, when the suspending medium is a Newtonian fluid, $J(t)$ can be expressed as follows [44, 108]:

$$J(\tau) = \frac{\tau}{\eta} = \frac{\langle \Delta r^2(\tau) \rangle_{t_0} \pi a}{k_B T}, \tag{3.10}$$

where $\langle \Delta r^2(\tau) \rangle_{t_0}$ is the particle MSD as introduced in Equation (3.4). Whereas, $J_{cs}(t)$ is proportional to $\Pi(\tau)$ [44] and it assumes the following analytical expression:

$$J_{cs}(\tau) = J_{OT} \left(1 - e^{-\lambda \tau}\right), \tag{3.11}$$

where $J_{OT} = 6\pi a/\kappa \propto \langle r^2 \rangle_{eq.}$ is the time-independent compliance of the OT, which is inversely proportional to the trap stiffness and whose values are represented in Figure 3.1–(D) by the plateau values of the MSD curves. $J_{cs}(t)$ has been derived by combining Equations (3.6), (3.8) and (3.10) and it is represented by the $\Pi(\tau)$ data drawn in the inset of Figure 3.1–(D) for the same combinations of fluids' viscosity and trap stiffness discussed above. From Equations (3.10) and (3.11) it follows that, by dividing the 2^{nd} Maclaurin polynomial of $J_{cs}(t)$ by $J(\tau)$, one would obtain the following ratio:

$$\frac{J_{cs}(\tau)}{J(\tau)} = \left(1 - \frac{\tau}{\tau_{OT}}\right) \equiv \left(1 - \frac{J(\tau)}{J_{OT}}\right), \tag{3.12}$$

which provides a means for elucidating the high values of the viscosity MAPE at relatively high trap strengths, as reported in Figure 3.3–(C). Indeed, from Equation (3.12) one could

argue that: at short lag-times, $J_{cs}(\tau) \cong J(\tau)$ *if and only if* $\tau_{OT} >> \tau$ (or equivalently for $J_{OT} >> J(\tau)$), which is true either for vanishing trap strengths (e.g., blue symbols in Figure 3.1–(D)) or for increasingly high viscous fluids (e.g., star symbols in Figure 3.1–(D)). Therefore, given that the accuracy to which the viscosity is calculated depends on the number of data points of the NPAF (or equivalently of the MSD via Equation (3.10)) available at lag-times $\tau < \tau_{OT}$ – i.e., within the time–window ranging from $\tau_1 = 1/f$ (for which $A(\tau_1) \sim 1$) to $\tau = \tau_{OT}$ (for which $A(\tau_{OT}) = e^{-1}$), used for the fitting procedure – the analysis of the particles' trajectory will return viscosity values with a high degree of uncertainty at relatively large κ values, for which $\tau_{OT} \to \tau_1$. Indeed, as shown in Figure 3.1 (D), for each fluid's viscosity, the effective time–window $[t_1, \tau_{OT}]$ shortens as the trap stiffness increases. From a physics prospective, this is simply because the stronger is κ, the smaller is the particle variance from the trap centre (i.e., Eq. (3.8)), thus overshadowing the fluid's contribution to the particle dynamics. Notably, the above concept are in agreement with the Fickian approach adopted by Matheson *et al.* [4] to estimate the viscosity of Newtonian fluids via MOT measurements, by determining the gradient of the MSD at the first two lag-times (i.e., $\tau_1 = 1/f$ and τ_2); for which they obtained an average error of $\sim 10\%$ (see Equation 10 and related results in Figure 5 of their manuscript).

In order to better understand the *optimal modus operandi* of MOT measurements, it is thus important to analyse the relative position of the system's characteristic time within the 'finite' experimental time–window. This concept has been recently introduced by Tassieri *et al.*[23] while testing the efficacy of a novel analytical tool (i-Rheo *GT*) for converting the time–dependent materials' shear relaxation modulus into their frequency–dependent complex shear modulus. In particular, they introduced a dimensionless parameter $T_a = log(\tau/t_1)/log(t_N/t_1)$ that accounts for the relative position of the material's characteristic relaxation time τ to that of the experimental time window $[t_1, t_N]$; where t_1 is the shortest time of the experimental data set (here $t_1 = 1/f$) and t_N is the longest one (here $t_N \equiv T_m = N/f$). Interestingly, in the context of this work, T_a assumes the following form:

$$T_a = \frac{log(f\tau_{OT})}{log(N)}, \tag{3.13}$$

and by plotting the MAPE of the viscosity *vs.* T_a, as shown in Figure 3.4, it is possible to identify a value of $T_a \simeq 1/3$ where MAPE assumes a minima. Notably, this could be used to express N as a function of De_{OT} via Equations (3.9) and (3.13), i.e.: $N \simeq De_{OT}^{-3/2}$; thus, providing a means of estimating the number of data points to be acquired to achieve a MAPE of $\sim 1\%$ for any generic fluid. This is indeed possible if the trap stiffness of the OT rig is calibrated first in water and it is also assumed not to vary significantly when

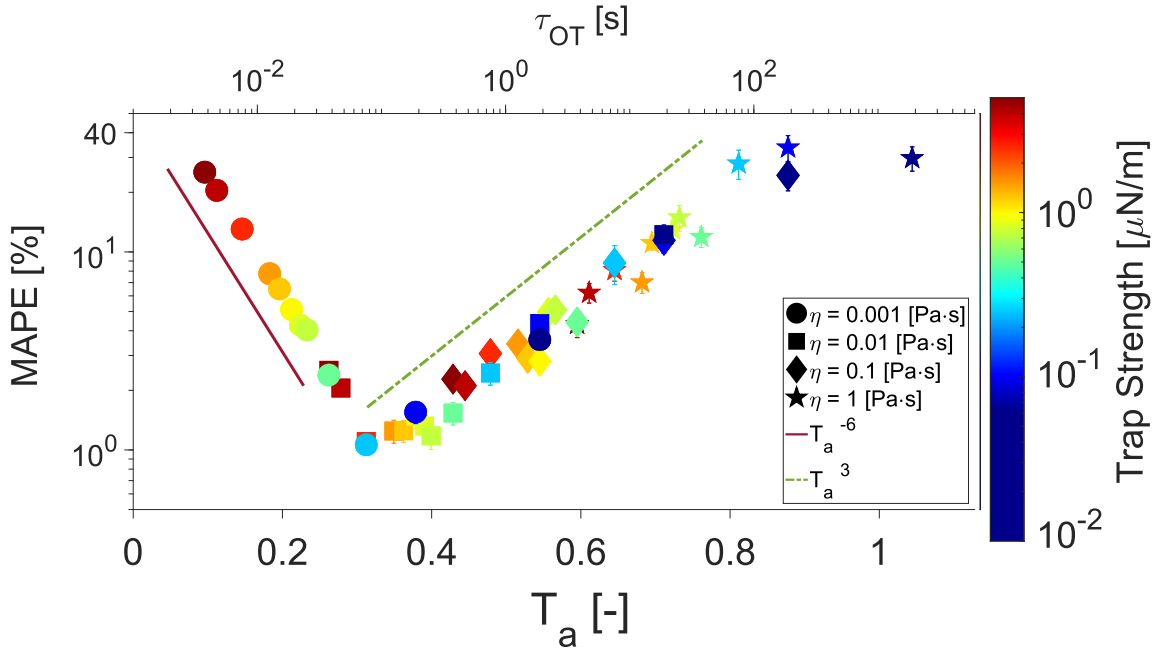

Figure 3.4: Data taken from Figure 3.3–(F) for the trajectories with maximum T_m and drawn *vs.* T_a. The top axis reports the characteristic time of the compound system τ_{OT}. The colour bar indicates the nominal trap stiffness used during the generation of the trajectories. The two lines are guides for the power laws as indicated in the legend.

measurements are performed on different fluids (i.e., when the refractive index of the sample under investigation does not differ significantly from that of water). With these conditions satisfied, one could write:

$$N \simeq N_w \eta_r^3, \tag{3.14}$$

where N_w is the number of positional data points acquired during the microrheology measurement performed in water (e.g., here $N_w \simeq 10^6$) and $\eta_r = \eta/\eta_w$ is the relative viscosity of the fluid under investigation to that of water, of which an estimate is needed to determine N.

Moreover, from Figure 3.4, it is interesting to notice that (i) for $T_a < 1/3$, the MAPE of the viscosity decreases with a power law of T_a^{-6} as $T_a \to 1/3$ from the left, and that (ii) the data points adhering to this scaling law are mostly those obtained from trajectories drawn by using as inputs a low viscosity value (i.e., 0.001Pa·s) and relatively high trap stiffness as the outcomes diverge from the minima. Thus implying that the MAPE of the viscosity in this region is governed mainly by the trap strength. Whereas, for $T_a > 1/3$, the MAPE of the viscosity follows a power law of T_a^3 and the data points adhering to this scaling law are mainly related to those trajectories drawn with a relatively low trap stiffness and relatively

high viscosity, for which the measurement duration is not long enough for the bead to explore the whole potential well.

In summary, we can argue that microrheology with OT requires long measurement times with many individual readings to achieve fluid's viscosity measurements with an error of only a few percent, which in practice translates to a measurement duration of the order of tens of minutes when dealing with fluids having viscosity close to that of water, OT rigs working at kHz and exerting a trap stiffness of the order of a few μN/m. Notably, when attempting microrheology measurements of fluids with significantly higher viscosity than water and with the same experimental conditions mentioned above, Equation (3.14) reveals that the measurement duration would become soon '*unachievable*' because T_m scales with the cubic power of the relative viscosity: $T_m \simeq T_{m,s}\eta_r^3$. These conclusions further corroborate Tassieri's '*opinion*' [80] that conventional passive microrheology measurements with OT of living systems "*are not an option*", as biological processes occur at much shorter time scales than the required T_m and therefore their rheological properties could not be considered '*time invariant*' during the measurements. Thus the aim of this paper to employ machine learning algorithms to significantly shorten the duration of microrheology measurements performed with OT, as elucidated hereafter.

3.5.1 Enhanced MOT with Machine Learning

Let us now investigate the efficacy of ML algorithms when used to enhance the accuracy of viscosity measurement of Newtonian fluids in passive MOT measurements. It would be prudent here to highlight the change in language that will occur when discussing the aforementioned ML algorithms. Indeed, throughout the previous sections, the attainment of Newtonian viscosity by means of conventional analytical methods presented in Equations (3.1) - (3.4) has been justifiably described as '*calculated*', however the ML algorithms described in this paper specifically '*predict*' the viscosity of the Newtonian fluid in question and therefore they will be described as such here.

As for the results described in Figure 3.3–(A–C and F), the simulated trajectories used for evaluating the ML models were generated for optically trapped particles suspended into four fluids having viscosity spanning three orders of magnitude (i.e. from 0.001 to 1Pa·s). Figure 3.3–(D) shows the MAPE of the fluids' viscosity prediction versus the measurement time, associated with input segment length, for the ML algorithms fed with the following inputs: the trap strength, particle radius, temperature and acquisition rate having values of 0.25μN/m, 1μm, 19^{o}C and 1kHz, respectively. It can be seen that for measurement times

shorter than 1s, using the architecture described in the methods section, the MAPE is as high as 40% depending on fluid viscosity. Interestingly, for a measurement time of 0.05s the MAPE for the highest viscosity analysed of $\eta = 1$Pa·s is 10%, which is four times lower than the conventional method using 1s of trajectory. This is a striking result, considering that the characteristic time for that particular point, $\tau_{OT} \approx 75$, is around 1500 times larger than the measurement time. Whereas, for $T_m = 1$s, the prediction error drops to between $3-6\%$ across the three decades of fluid viscosity explored. Notice that, the input measurement times used in this study did not exceed a value of 1s because of the demanding computational processes involved in training of ML algorithms. Therefore, in order to obtain consistent predictions of fluid viscosity, to extrapolate to 1024s, the input measurement time used in Figure 3.3–(E) was 1s. The extrapolation was carried out by feeding 1s segments of particle trajectory into each of the three 1s input ML models trained and averaging each of the predictions over increasingly longer times. The diagram shows the MAPE of the ML viscosity prediction versus the measurement time extrapolated to 1024s using the same parameters described in Figure 3.3–(D). Generally, as the measurement time increases, the MAPE, starting at values between $3-6\%$, quickly drops to a plateau value for each viscosity, reaching as low as 0.4% for a viscosity of 0.1Pa·s. When compared to the conventional method in Figure 3.3–(C), the viscosity prediction errors displayed in Figure 3.3–(E) are significantly lower for most of the explored time windows, apart from the MAPE of the conventional approach at the longest times. It is important to highlight that, in machine learning algorithms the individual model accuracy is determined by the model hyper-parameters as well as the size and quality of training data. Moreover, the random initialisation of the training process can cause the model to learn to predict particular viscosity ranges more accurately than others. The variability in performance of different instances of the same model for different viscosity values is indicated by the error bars in Figures 3.3–(D-E). Notably, the significant reduction in MAPE from the conventional approach to the ML prediction occurs over the entire range of explored viscosity.

As for standard ML studies, we have selected the best performing 1s model to be analysed for a range of trap strengths as shown in Figure 3.3–(F). Here, the MAPE of both the conventional method (closed symbols) and the ML model (open symbols) are plotted versus $De^{-1}_{OT,Nom.}$ for trap strengths ranging from $0.01-5\mu$N/m. Notice that, the range of trap strengths used in ML analysis is $0.01-0.85\mu$N/m, which is slightly wider than the range of trap strengths used in training ($0.08-0.39\mu$N/m). Figure 3.3–(F) shows that the MAPE values of the ML algorithm are 5 times smaller than those of the conventional method for

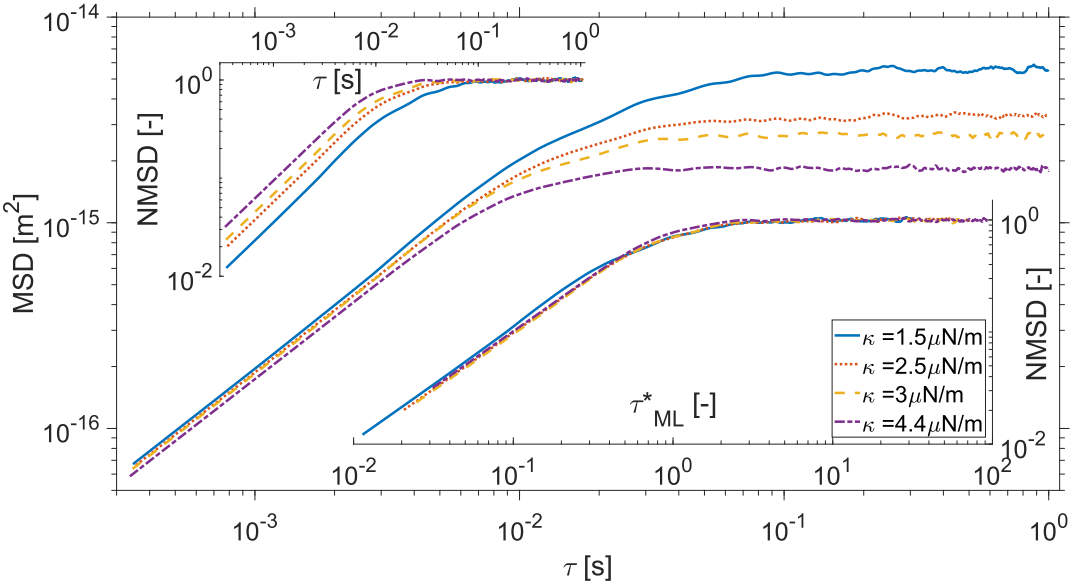

Figure 3.5: (Main) The mean square displacement (MSD) *versus* lag-time τ of the trajectory of an optically trapped particle suspended in water and subjected to different trap strengths κ. (Top-left inset) The same data as in the main, but normalised by twice the variance of the particle displacement from the trap center, which returns the normalised mean square displacement (NMSD) *versus* τ. (Bottom-right inset) The same data as in the top-left inset, but *versus* a dimensionless lag-time $\tau^*_{ML} = \kappa\tau/(6\pi a\eta_{ML})$.

$De^{-1}_{OT,Nom.} < 1$; i.e., $\sim 7\%$ and $\sim 35\%$ respectively. It is also apparent that, unlike the conventional method, the ML error curves do not collapse into a master curve when drawn against $De^{-1}_{OT,Nom.}$. This is believed to be due to the design of the feature extraction component of the ML architecture, which uses convolutional filters that learn local temporal structures common to both short and long trajectories. Therefore, once the model has learned to extract low- and high-dimensional local features in the measurements *a priori* during the training process, the CNN can decode the fluids' viscosity '*directly*' from the raw measurements using a statistically relevant number of steps N' required to disambiguate features that are present in the data, rather than from statistically averaged quantities over $N = T_m f$ steps used in the standard approach. Notably, the number N' can be much smaller than N and no longer needs to satisfy the scaling governed by the Deborah number on the individual measurement – as the missing information has been encoded before the measurement into the learned CNN parameters.

Confident of the effectiveness of the ML algorithm described above, we have employed it to determine the viscosity of water from real experimental MOT data obtained by tracking the position of an optically trapped bead subjected at different laser powers (i.e., trap

strengths). The analysis of the trajectories returned the MSD curves shown in the main Figure 3.5 having different plateau values at long lag-times, whose values are equal to twice the variance of the particle displacement from the trap center. These latter values can indeed be used to normalise the MSD curves as shown in the top-left inset of Figure 3.5, thus validating Equation (3.11) stating that at long lag-times the compliance of the OT overshadows the one of the fluid. In order to apply the ML algorithm to the raw data of the measurements described above, the simulated training data and the training of the model had to be adjusted to match the real experimental parameters, i.e.: (i) an acquisition rate of 2780fps; (ii) the length of the input data to 2780, to be consistent with the analysis of 1sec trajectory; (iii) the viscosity range has been narrowed to 10^{-3}–10^{-2} Pa·s and their values were randomly sampled from a log-uniform distribution; (iv) the values of the trap stiffness have been increased to a range of 1–5μN/m and they were randomly sampled from a uniform distribution. As for the simulated data described earlier, the ranges of viscosity and trap strength were slightly greater than the target range to encompass the extremities. Notably, when the ML algorithm was applied to real experimental data of 1 second duration, it returned an estimation of the fluid viscosity of $\eta_{ML} = 0.986 \pm 0.028$ mPa·s, which would result in an error as low as 1.1% at best, when compared with the viscosity value of water obtained by means of bulk rheology measurement, $\eta_{water} = 0.997$ mPa·s (at $T = 20^{o}$C). The effectiveness of the method is further corroborated by the master curve drawn in the bottom-right inset of Figure 3.5, where the NMSD curves have been plotted against a dimensionless lag-time $\tau^{*}_{ML} = \kappa\tau/(6\pi a\eta_{ML})$.

Therefore, we can argue that ML has the ability to enhance the accuracy of passive MOT measurements by significantly reducing the measurement time from tens of minutes down to 1s with a prediction error that is 5 times smaller than the conventional analytical method applied to the same data. Additionally, the ML algorithm shown here is able to predict the viscosity of a Newtonian fluid across 3 decades range and we expect that a less generalised model, which is trained on a smaller span of viscosity values, could further improve the performance of the ML approach.

3.6 Discussion

In this article we provide experimental evidence supporting the observation made by Tassieri [80] in 2015, that conventional linear microrheology with optical tweezers may not be an appropriate experimental methodology for studying the viscoelastic properties of living systems. In particular we have focused on the analysis of computer simulated trajectories of an

optically trapped particle suspended within a set of Newtonian fluids having viscosity values spanning three decades, i.e. from 10^{-3} to 1 Pa·s. The conventional statistical mechanics analysis of these simulations has led to the following key findings: (i) we corroborate the requirement for MOT studies to perform "*sufficiently*" long measurements when using conventional analytical methods for data analysis and (ii) we provide, for the first time in literature, a means for estimating the required duration of the experiment to achieve an uncertainty as low as 1%; (iii) we provide evidence explaining why conventional MOT measurements commonly underestimate the materials' viscoelastic properties, especially in the case of high viscous fluids or soft-solids such as gels and cells. Moreover, we have developed a machine learning algorithm that uses feature extraction on only 'one second' of trajectory data to determine the viscosity of Newtonian fluids, yet capable of returning viscosity values carrying an error as low as $\sim 0.3\%$ at best, which is five times smaller than those obtained from conventional analytical methods applied to the same data. Our results clearly indicate that machine learning is a valid option to be exploited to perform fast and accurate microrheology measurements with optical tweezers in Newtonian fluids and we believe that this is the first step for its use in living systems, provided an adequate volume of data is available to train such a model.

3.7 Author Contributions

Matthew G. Smith: conceptualization, investigation, methodology, formal analysis, writing – original draft preparation, writing - review and editing; **Jack Radford**: investigation, visualization, formal analysis, writing - review and editing; **Helen O'Mahony**: conceptualization, investigation; **Jorge Ramírez, Eky Febrianto, Graham M. Gibson, Andrew B. Matheson**: writing - review and editing; **Daniele Faccio**: supervision, writing - review and editing; **Manlio Tassieri**: conceptualization, methodology, validation, supervision, project administration, writing – review and editing.

3.8 Conflicts of interest

There are no conflicts to declare.

3.9 Acknowledgements

This work was supported by the EPSRC CDT in “Intelligent Sensing and Measurement” (EP/L016753/1). M.T. acknowledges support via EPSRC grant “Experiencing the micro-world - a cell’s perspective” (EP/R035067/1 – EP/R035563/1 – EP/R035156/1).

Chapter 4

The role of elastic instability on the self-assembly of particle chains in simple shear flow

Matthew G. Smith [a], Graham M. Gibson [b], Andreas Link [a], Anand Raghavan [c], Andrew Clarke [c], Thomas Franke [a], Manlio Tassieri [a],

[a] Division of Biomedical Engineering, James Watt School of Engineering, University of Glasgow, Glasgow G12 8LT, U.K.

[b] School of Physics and Astronomy, University of Glasgow, Glasgow G12 8QQ, U.K.

[c] Schlumberger Cambridge Research, High Cross, Madingley Road, Cambridge, CB3 0EL, U.K.

Published: Physics of Fluids

Access: https://doi.org/10.1063/5.0182175 [109]

Author Declaration

I confirm that my contribution to this paper is over 50%.

4.1 Abstract

Flow-Induced Self-Assembly (FISA) is the phenomena of particle chaining in viscoelastic fluids while experiencing shear flow. FISA has a large number of applications across many fields including material science, food processing and biomedical engineering. Nonetheless,

this phenomena is currently not fully understood and little has been done in literature so far to investigate the possible effects of the shear-induced elastic instability. In this work, a bespoke cone and plate shear cell is used to provide new insights on the FISA dynamics. In particular, we have fine tuned the applied shear rates to investigate the chaining phenomenon of micron-sized spherical particles suspended into a viscoelastic fluid characterised by a distinct onset of elastic instability. This has allowed us to reveal three phenomena never reported in literature before, i.e.: (I) the onset of the elastic instability is strongly correlated with an enhancement of FISA; (II) particle chains break apart when a constant shear is applied for 'sufficiently' long-time (i.e. much longer than the fluids' longest relaxation time). This latter point correlates well with the outcomes of parallel superposition shear measurements, which (III) reveal a fading of the elastic component of the suspending fluid during continuous shear flows.

4.2 Introduction

Flow-Induced Self-Assembly (FISA) of single particles into long chains while subjected to shear flow is a phenomenon that has been discussed at length since its first description in the 1977 paper by Michele *et al.*[110]. FISA phenomena occur frequently across a variety of applications, e.g.: (i) in material science, it is well documented that the inclusion of micro and nano particles in polymer melts can greatly enhance the final mechanical properties of products [111]; (ii) in food processing, the addition of soft microspheres or microgel droplets can be used to encapsulate phytonutrients for targeted delivery in the gut [112]; and (iii) in microfluidics, particle alignment is often required to enhance processes such as counting, analysis and separation [113–118].

Currently, the exact mechanism that causes micro-particles to align in simple shear flow is unclear, and the focus of the debate between different schools of thought is mainly on the relative contribution to the driving force governing the phenomena by the elastic and the viscous forces generated during flow, due to the viscoelastic nature of complex fluids. It follows that, most of the arguments have been developed around the relative value assumed by the Weissenberg number (Wi), which is a dimensionless parameter used in rheology studies to describe the ratio between the elastic and the viscous forces. For a general overview of the field, an up-to-date review has been masterly drawn by D'Avino and Maffettone [119], whose highlights are summarised hereafter for the convenience of the reader. The aforementioned work by Michele *et al.*[110] reported for the first time glass beads forming into

long chains and aggregations in a viscoelastic media, under both oscillatory and pipe flows; suggesting that (i) the alignment of particles could be related to the fluid's normal stresses (a measure of the fluid's elastic character) and that (ii) a critical Weissenberg value of 10 is necessary for the alignment to occur. Subsequent studies by Petit and Noetinger [120], and Lyon *et al.* [121] further corroborated Michele's observation in the case of string formation. Conversely, a more recent study by Won and Kim [122] suggests that the shear-thinning nature of the suspension fluid is the driving force for FISA, while normal stresses facilitate migration. Furthermore, Scirocco *et al.* [123] found that a critical Weissenberg number (as low as 1) is not solely responsible for string formation as they observed no alignment in Boger fluids (i.e., a viscoelastic fluid with a constant viscosity value). Interestingly, by varying the gap distance between their parallel plate flow cell, Scirocco *et al.* [123] also found that FISA is a phenomena that occurs within the bulk of the fluid, rather than being a wall effect. However, in contrast to these findings, other studies [124, 125] observed single particles migration towards the walls, where they would assemble and form strings in the flow direction, when suspended in weakly viscoelastic liquids (i.e., $Wi << 1$). Nonetheless, a recent study by Pasquino *et al.* [126] has shown that FISA occurs in both the bulk of the fluid and at the walls of the system; thus implying that such phenomenon is a convoluted function of specific parameters of the system being analysed, such as fluids' viscoelastic properties and flow cell geometries.

Nevertheless, most of the works cited above, and in general in literature, have focused on low Weissenberg numbers (i.e., $Wi < 10$) in simple flow cell geometries. Whereas, little has been done to study FISA at relatively high Weissenberg numbers (i.e., $Wi >> 10$), where the shear-induced elastic instability may develop. In this regard, it is worth to remind that elastic turbulence, first proposed by Groisman and Steinberg [127], has been observed in microchannel flow [128] and in core-floods [129], and it describes fluctuations in the flow velocity across a broad range of spatial and temporal frequencies, up to a threshold shear rate, where a sharp power-law transition occurs [129–131]. This transition is identified by a dimensionless parameter M_{Norm}, as posited by Mckinley *et al.*[130, 131], and further explored in this manuscript for the case of simple shear flow of a shear thinning fluid, which is made of a water based solution of a high molecular weight Polyacrylamide. Interestingly, in a recent study by Howe *et al.*[129], it has been shown that the onset of the shear-induced elastic instability of Polyacrylamide solutions is very distinct and it is concentration independent, but it scales with the square of the polymers' molecular weight.

In this work, a bespoke, counter-rotating cone and plate shear cell has been used to anal-

yse the effects that fluid's viscoelasticity, and more specifically the shear-induced elastic instability, has on FISA. This has been investigated by exploring shear rates that spanned across the onset of elastic instability of a water based solution of Polyacrylamide (PAM), whose frequency-dependent viscoelastic moduli have been determined by means of both classical bulk rheology and microrheology measurements performed with optical tweezers. In agreement with previous works in literature, we have observed that particle chains form in the bulk of the fluid and in the flow direction. In particular, we show that FISA is significantly enhanced by the onset of the elastic instability; although, a significant alignment is also observed at lower shear rates. Moreover, we report evidence of a spontaneous reduction in particles' chain length at relatively long times (i.e., much longer than the fluids' longest relaxation time), which is not associated with particle migration (e.g., sedimentation), but actually to a shear-induced change of the viscoelastic properties of the suspending fluid [132]. We speculate that these changes may be caused by a shear induced disentanglement of the polymer chains constituting the viscoelastic fluid. This thesis is supported by the outcomes of parallel superposition shear flow measurements, as described below.

4.3 Materials and Methods

Particle Suspension

A dilute solution of particle suspension was prepared by gently mixing 5.2μm diameter polystyrene beads (Bangs Laboratories), at a final concentration of 0.02% w/v, in a water based solution of Polyacrylamide (PAM – molecular weight 18M, Polysciences Inc.) at a final concentration of 0.07% wt. This concentration is circa ten times higher than the polymer's entanglement concentration, which has been estimated to be (i) $\sim$ 0.008%wt as obtained via viscometry measurements performed by Howe *et al.* [129] and (ii) $\sim$ 0.007%wt as read from Figure 6-(D) of the work by Tassieri *et al.* [133] reporting a comparison between the viscosity values measured by means of multiple rheological techniques. Additionally, a 97%wt glycerol/water mixture with beads concentration of 0.02% w/v was used as a control. This ratio of glycerol/water mixture was chosen based on the fact that its Newtonian viscosity of $\eta = 0.765$ Pa·s closely approximates the one of the PAM solution at low frequencies.

Bulk rheology

Bulk rheology measurements were performed with a stress-controlled rheometer (Netzsch Kinexus Ultra+), utilising a roughened cone and plate geometry (4^o cone, 25mm radius plate). All measurements were performed at 20^oC, and prior to a rheological measurement, the sample underwent a pre-shear at $10s^{-1}$ for 3min, to homogenise the sample and remove any history dependant effects from the loading procedure. Partially hydrolysed polyacrylamide (Flopaam 3630S – molecular weight 18-20MDa, SNF) at a final concentration of 0.07%wt in deionised water, without polystyrene beads, was used for all measurements. Parallel superposition measurements were conducted at constant shear rates of $0.49s^{-1}$ and $0.79s^{-1}$. As the instrument is stress controlled, these shear rates were converted to stress values utilising Carreau – Yasuda fitting parameters from flow curve data. An oscillation stress amplitude of 0.1133Pa was selected from a dynamic amplitude sweep measurement, lying within the linear viscoelastic region. The parallel superposition measurement was conducted at a frequency of 0.4Hz, sampling over a duration of 2hr.

Optical tweezers rig

Microrheology measurements were performed by using an OT system based on a continuous wave, diode pumped solid state (DPSS) laser (Ventus, Laser Quantum), which provided up to 3 W at $1,064$ nm. A nematic liquid crystal spatial light modulator (SLM) (BNS, XY series 512×512) was used to create and arrange the desired optical trap. The laser entered a custom-made inverted microscope that uses a microscope objective lens (Nikon, 100x, 1.3 NA) to both focus the trapping beam and to image the thermal fluctuations of a 4.74μm diameter silica bead (Bangs Laboratories), at room temperature $\sim 20^o$C. The sample was mounted on a motorized microscope stage (ASI, MS-2000). A complementary metal-oxide semiconductor (CMOS) camera (Dalsa, Genie HM 1024 GigE) acquired high-speed images of a reduced field-of-view. These images were processed in real-time at up to ~ 1 kHz to calculate the center of mass of the bead by using a particle tracking software developed in LabVIEW (National Instruments), running on a standard desktop PC [90, 91].

A Theoretical Background of Microrheology with Optical Tweezers

Microrheology is an branch of Rheology (the study of the flow of matter), and it is focused on the characterisation of the viscoelastic properties of complex fluids by using sample volumes in the micro-litre range; thus making microrheological methods ideal candidates for measur-

ing rare or precious samples, with a clear advantage over classical bulk rheology approaches that require millilitres of sample volume. Microrheology techniques are categorised into either "passive" or "active" depending on whether the tracer particle, suspended in the target fluid, is driven by thermal fluctuations within the fluid, or by means of an external force, respectively.

Developed in the 1970s [134], optical tweezers (OT) utilise a monochromatic laser beam, focused through a microscope objective with a high numerical aperture, to optically trap in three dimensions a micron sized particle, suspended in a fluid; a schematic representation is presented in Fig4.2-(A). Once trapped, the particle 'feels' a harmonic potential, therefore the restoring force exerted on the particle is linearly proportional to the distance from the center of the trap, provided the displacement is within the bead diameter, and it is of the order of a few μN. In this work, passive microrheology with OT (MOT) has been used to measure the viscoelastic properties of a PAM solution at a concentration of 0.07% wt. The thermal fluctuations of an optically trapped particle were analysed by means of the theoretical framework developed by Tassieri *et al.*[39, 133, 135], which is here summarised for convenience of the reader.

The Brownian motion of an optically trapped particle can uncover the viscoelastic properties of the suspending fluid when its trajectory is analysed by means of a generalised Langevin equation (Eqn.(4.1)) – as first established by Mason and Weitz [136] for the case of a freely diffusing particle – which in this case reads:

$$m\vec{a}(t) = \vec{f}_R(t) - \int_0^t \xi(t-\tau)\vec{v}(\tau)d\tau - \kappa\vec{r}(t), \tag{4.1}$$

where m is the mass of the particle, $\vec{a}(t)$ is its acceleration, $\vec{v}(t)$ is its velocity, $\vec{r}(t)$ is its position, $\vec{f}_R(t)$ is the Gaussian white noise term used for modelling the stochastic forces acting on the particle, and $\xi(t)$ is the generalised time-dependent memory function accounting for the viscoelastic nature of the fluid.

As described by Tassieri *et al.*[39, 133, 135, 137], Eqn.(4.1) can be solved for the fluid's complex modulus ($G^*(\omega)$) *via* either the normalised mean squared displacement (NMSD) $\Pi(\tau) = \langle \Delta r^2(\tau) \rangle / 2\left\langle r^2 \right\rangle$ or the normalised position autocorrelation function (NPAF) $A(\tau) = \langle \vec{r}(t)\vec{r}(t+\tau) \rangle / \left\langle r^2 \right\rangle$, which are simply related to each another as:

$$\Pi(\tau) = \frac{\langle \Delta r^2(\tau) \rangle_{t_0}}{2\langle r^2 \rangle_{eq.}} \equiv \frac{\langle [r(t_0+\tau) - r(t_0)]^2 \rangle_{t_0}}{2\langle r^2 \rangle_{eq.}} = 1 - A(\tau), \tag{4.2}$$

where τ is the lag-time ($t - t_0$) and the brackets $\langle ... \rangle_{t_0}$ represent an average over all initial

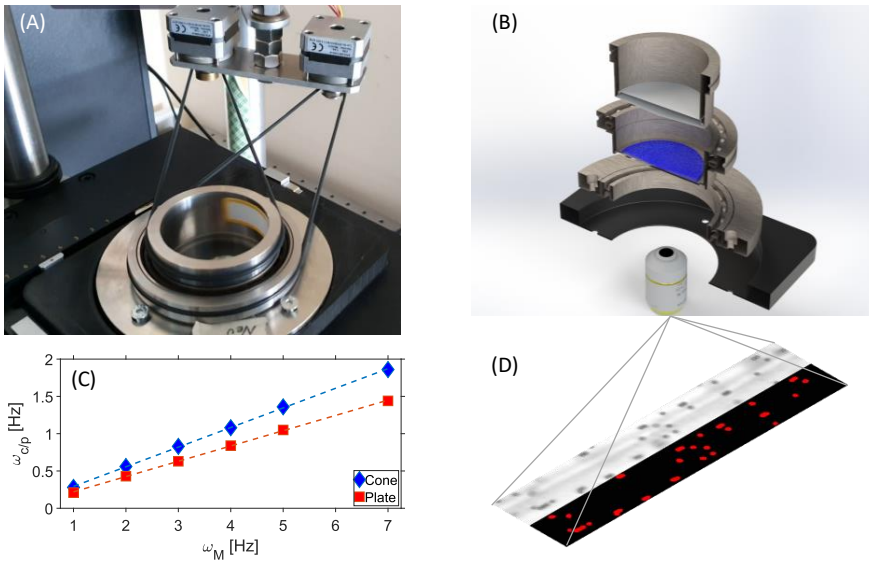

Figure 4.1: (A) A picture of the bespoke shear cell mounted on a microscope stage with two driving motors. (B) An exploded schematic representation of the shear cell showing the transparent cone (grey area) and plate (blue area) geometries. (C) Calibration curve comparing the rotational frequency of the cone and the plate ($\omega_{c/p}$) versus the rotational frequency of the motors (ω_M). The conversion factor for the cone and the plate was 0.263 and 0.205, respectively. (D) Example of a typical frame captured during experiments and the same image post processing. In red are the single beads, dimers and one trimer identified by using the particle tracking software developed in LabVIEW (National Instruments) for this work, running on a standard desktop PC.

times t_0. The fluid's complex modulus can then be expressed as:

$$G^*(\omega)\frac{6\pi a}{\kappa} = \left(\frac{1}{i\omega\hat{\Pi}(\omega)} - 1\right) \equiv \left(\frac{1}{i\omega\hat{A}(\omega)} - 1\right)^{-1} \equiv \frac{\hat{A}(\omega)}{\hat{\Pi}(\omega)} \tag{4.3}$$

where $G^*(\omega)$ is a complex number, whose real and imaginary parts define the elastic ($G'(\omega)$) and the viscous ($G''(\omega)$) moduli of the fluid, respectively; a is the particle radius, κ is the optical trap stiffness, $\hat{\Pi}(\omega)$ and $\hat{A}(\omega)$ are the Fourier transforms of the NMSD and the NPAF, respectively. To obtain Eqn.(4.3), the inertial term ($m\omega^2$) present in the original works[138, 139] has been here neglected, because for micron-sized particles it only becomes significant at frequencies of the order of MHz. From Eqn.(4.3) it is a trivial step to derive the complex viscosity ($\eta^*(\omega)$) of the fluid:

$$|\eta^*(\omega)| = \frac{\sqrt{G'^2(\omega) + G''^2(\omega)}}{\omega}. \tag{4.4}$$

Shear Cell

The shear cell used in this work had a bespoke cone and plate design, both of which were transparent allowing the use of an optical microscope to capture images and the generation of a uniform shear rate along the diameter of the shear cell. An image and an exploded schematic representation of the setup is shown in Fig.4.1-(A,B). The shear cell is positioned on top of a microscope stage and is composed of several individual parts including: the 3D printed base, the shear cell mount, the plate body, and the cone, which slot together creating a chamber for the fluid being analysed. As shown in Fig.4.1-(B), the base of the shear cell (black) is 3D printed that allows the setup to fit within the microscope stage and hence accurately position the shear cell within the optical path of the microscope. The mount for the shear cell is a ring that screws into the 3D printed base and houses a bearing around its internal diameter. On this bearing sits the plate body allowing the plate to rotate freely. The plate body also has a bearing on which the cone body sits. The fluid is applied between the cone and the plate, which in Fig.4.1-(B) is schematically represented by the blue area. The rotation of the cone and the plate was driven by two independent stepper motors via two nitrile O-rings as shown in Fig.4.1-(A). Motor control was provided by two individual Arduino boards, each driving an A4988 stepper motor controller, interfaced with a Labview program that allowed us to control motor speed.

Prior to performing the measurements, a calibration of the relative speed between the two electric motors and the related cone and plate geometries was performed. This consisted in varying the rotational frequency of the motors and measuring those of the related geometries, which was much lower because of the relatively high gear ratio. The rotational frequency of the driven cone/plate ($\omega_{c/p}$) can be calculated using the Eqn.(4.5), which is based on the diameter ratio between motor and the cone/plate, d_m and $d_{c/p}$ respectively.

$$\omega_{c/p} = \frac{d_m}{d_{c/p}} \omega_M, \tag{4.5}$$

where ω_M is the rotational frequency of the motor shaft and the diameter of the cone and the plate are 60 and 80mm respectively.

Calibration was measured in three configurations: (i) with either the cone or the plate stationary, (ii) with both rotating in the same direction and (iii) with both rotating in opposite directions. The purpose of measuring in each configuration was to make sure that the rotation of the cone did not influence the rotation of the plate and *vice versa*. In each configuration the time required for the cone and the plate to complete 10 revolutions was measured. The rotational frequency of both the cone and the plate were graphed against the rotational fre-

quency of the motors, shown in Fig.4.1-(C), and the gradient of the line is the inverse of the gear ratio.

The shear cell was counter rotated, and the shear rates explored during the measurements are those reported in Table4.1, which shows also the rotational frequency of the cone driving motor (ω_{cM}) and the plate driving motor (ω_{pM}) required to achieve an equal rotational frequency of the cone and the plate ($\omega_{c/p}$) for each of the shear rate examined:

$$\dot{\gamma} = \frac{(\omega_c + \omega_p)}{tan(\alpha)} \simeq \frac{(\omega_c + \omega_p)}{\alpha}, \tag{4.6}$$

where $\dot{\gamma}$ is the shear rate and α is the angle of the cone (i.e.$4.20^\circ \pm 0.25^\circ$) [140, 141]. The truncation gap of the cone was $125\mu m$, which is significantly larger than the polystyrene beads used in the suspension (diameter of $5.2\mu m$) and therefore gap effects are negligible [123].

$\dot{\gamma}\,[s^{-1}]$	$\omega_c\,[rad \cdot s^{-1}]$	$\omega_p\,[rad \cdot s^{-1}]$	$\omega_{cM}\,[rad \cdot s^{-1}]$	$\omega_{pM}\,[rad \cdot s^{-1}]$
27.682	1.025	1.005	3.896	4.901
43.479	1.603	1.584	6.095	7.728
68.403	2.528	2.486	9.613	12.127
107.745	3.983	3.916	15.143	19.101
169.028	6.246	6.144	23.750	29.971
265.690	9.816	9.660	37.322	47.124

Table 4.1: Table of shear rates and rotational frequencies explored in this work.

The sample, 750μl of 0.07%wt PAM-bead solution, was inserted between the cone and the glass coverslip (plate) and then a constant shear rate was applied for 30 minutes. Images were acquired using a Teledyne Dalsa Genie camera at 960fps with an exposure time of 400μs. The high frame rate was achieved by reducing the region of interest of the camera from 1400×1024 pixels to 752×100 pixels. The window was aligned in the direction of flow, so that chaining could be observed through the major axis of the window and the focal plane was positioned in the center of the shear flow, which was kept constant for each experiment. A Labview program has been developed to allow us to run the camera at 960fps, but capture images at set intervals in milliseconds, thus improving significantly the performance of the image acquisition and reducing the time taken for analysis. The acquisition rate of the Labview program was set to 1.2s for all experiments, thus returning 1500 frames for each measurement; which were performed in triplicates. Fig.4.1-(D) shows a typical image frame

captured both before and after image processing.

Image analysis was carried out by using custom code, developed using National Instruments Labview, to automatically process the acquired images. Each frame was analysed by first removing the background of the image, as shown in Fig.1-(D), and then each particle/chain was identified automatically using functions from the National Instruments, Vision Development Module, which can discriminate different objects via their (i) area (as each additional bead in a given chain increases the object area linearly) and (ii) elongation value (which regulated the counting of only chains rather than artifacts such as particles' agglomerates); thus, allowing us to classify whether an identified object belonged to a specific chain length (i.e., single bead, dimer, trimer, tetra or penta). Once classified, the total number of each chain length per frame was exported into a spreadsheet.

4.4 Results and Discussion

Rheological characterization of a Polyacrylamide solution

The rheological properties of a PAM solution at a concentration of 0.07%wt were measured by means of both microrheology measurements performed with optical tweezers and conventional rotational shear rheology, as summarised in Fig.4.2-(D). In the case of microrheology, the trajectory of an optically trapped particle was captured at circa 1kHz for an extended measurement duration of circa 27 minutes, in compliance to the arguments described in detail by Smith *et al.*[70] to achieve statistically valid outcomes. The NPAF of the particle trajectory was analysed by using i-Rheo MOT [142], an algorithm based on the analytical method developed by Evans *et al.*[61] for evaluating the Fourier transform of any generic function, sampled over a finite time window, without the need for Laplace transforms or fitting functions. For more detail about the principles underpinning i-Rheo MOT, the reader is advised to read these references [20, 133, 137, 143].

The first and the second normal stress differences (N_1 and N_2, respectively) for the 0.07%wt PAM solution are shown in Fig.4.2-(C). They are in good agreement with the theoretical predictions of uniform shear flow of inelastic hard spheres in dilute regime, for which N_1 is expected to be positive and monotonically increasing for higher shear rates; while, N_2 is expected to be negative and monotonically decreasing for higher shear rates. Additionally, in the inset of Fig.4.2-(C), we report the ratio between N_1 and the applied shear stress (σ), which shows a plateauing behaviour at shear rates close to the onset of the shear induced elastic instability.

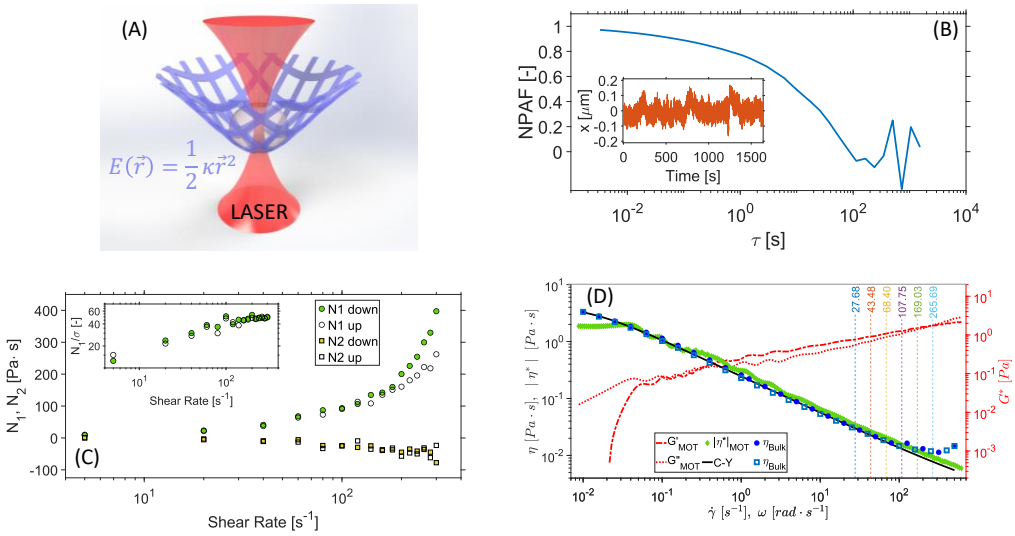

Figure 4.2: (A) A schematic representation of an optically trapped bead within a harmonic potential, $E(\vec{r})$, where κ is the trap stiffness and $\vec{r}(t)$ is the bead position from the trap centre. (B) The normalised position autocorrelation function (NPAF) *versus* lag-time (τ) calculated using the x coordinate of the trajectory of an optically trapped bead suspended in a 0.07%wt PAM solution shown in the inset. (C) The first and the second normal stress differences (N_1 and N_2, respectively) obtained using a cone and plate and parallel plate configurations respectively *versus* the shear rate. The inset displays the ratio between N_1 and the shear stress (σ) *versus* the shear rate. These measurements have been corrected for inertia which did not exceed 10% of the signal. (D) The viscoelastic moduli (red lines, $G'(\omega)$,$G''(\omega)$) and the complex viscosity (green diamond, $|\eta^*(\omega)|_{MOT}$) as obtained from the analysis of the NPAF shown in (B). In the same figure the shear viscosity (blue symbols, η) and its fit by means of Carreau-Yasuda model (black line, C-Y) are reported; η and $|\eta^*(\omega)|_{MOT}$ are plotted *versus* shear rate ($\dot{\gamma}$) and angular frequency (ω), respectively; in compliance to the Cox-Merz rule. The vertical dotted lines represent the shear rates explored in the shear cell experiments (see table 4.1).

In Fig.4.2-(D), we report the viscoelastic moduli ($G'(\omega)$, $G''(\omega)$) and the complex viscosity ($|\eta^*(\omega)|_{MOT}$) as obtained by means of MOT measurements together with the rotational shear viscosity (η_{Bulk}) obtained by using a stress-controlled rheometer. Strikingly, despite the substantial difference in the nature of the two rheological techniques employed here, the outcomes of these experimental approaches are in very good agreement over a range of shear rates/frequencies spanning ~ 5 decades. Moreover, it is important to highlight that, while at high shear rates (i.e., $\dot{\gamma} > 107.75\text{s}^{-1}$), bulk rheology measurements reveal the onset of the elastic instability as inferred by the blue symbols departing from the Carreau-

Yasuda fit (black line) of the flow curve in a shear thickening behaviour; this phenomenon is not revealed by the complex viscosity curve because of the quiescent nature of MOT measurements. Nonetheless, the viscoelastic moduli reveal the existence of two characteristic crossover frequencies occurring at (I) circa 0.3rad/s and (II) circa 200rad/s. The inverse of these frequencies provide a measure of two of the material's characteristic relaxation times, i.e.: the reptation time τ_{rep} and the entanglement time τ_e, respectively. These measurable parameters can be used to educe the material's Rouse time (τ_R) [144]:

$$\tau_R = \tau_e \left(\frac{\tau_{rep}}{6\tau_e} \right)^{2/3} \cong 0.12\ sec, \tag{4.7}$$

which, as we shall demonstrate hereafter, correlates very closely with the instability time [129] derived from bulk rheology measurements.

The vertical lines in Fig.4.2-(D) are the experimental shear rates investigated by using the cone and plate shear cell (see table 4.1). These shear rates span the range of the shear induced elastic instability and cover its onset, with the aim to provide new insights into FISA under this condition. At this point it is important to remind that, the onset of elastic instability has been described by means of a dimensionless parameter M, first introduced by McKinley *et al.*[130, 131], which is related to both the Weissenberg and the Deborah numbers of the system under investigation:

$$M = \sqrt{Wi \cdot De}. \tag{4.8}$$

This equation has been made explicit in the case of a cone and plate geometry[129], and here further modified for a counter rotating configuration:

$$M_{Norm} = \frac{M}{M_{crit}} = \frac{\lambda_{PM}(\omega_c + \omega_p)}{\sqrt{\theta}} . \frac{1}{M_{crit}}, \tag{4.9}$$

where λ_{PM} is a characteristic relaxation time of the viscoelastic fluid, for which we have adopted the suffix *PM* for Pakdel-Mckinley [130] to distinguish this time as already done by Howe *et al.*[129], and M_{crit} is the critical value of M when the flow becomes unstable. Interestingly, a linear-stability analysis [129, 130, 145] of a cone and plate geometry has shown that flow instability initiates at $M \geq 21.17$. Thus, by using this inequality and the onset of shear induced instability in Fig.4.2-(D) at $126.5s^{-1}$, it is possible to determine a characteristic relaxation time λ_{PM} of 0.14s, which can be associated to the material's Rouse time as described by Howe *et al.* [129] and here further corroborated by the value obtained from microrheology measurements with optical tweezers via Equation (4.7).

Accumulation of Particles

FISA phenomenon can be analysed by calculating the accumulation of chains, of a given length, over each successive image frame. The analysis can be thought of as a series of 'bins' into which different chain lengths are added. The number of chains in each bin can easily be summed over time to produce information on the long time effect of shear rate on the chaining occurring within the sample. As mentioned earlier, the image analysis software separated the particles/chains identified in each image frame into five different 'bins', i.e.: singles, dimers, trimers, tetras and pentas. The curves shown in Fig.4.3-(A) are the total number of single particles accumulated throughout the experiment for each imposed shear rate. Whereas, in Fig.4.3-(B) we report the accumulation of each chain length for the two extreme shear rates explored in this work.

From Fig.4.3-(A-B) it is clear and expected that the accumulation of particles increases with time. However, it is interesting to notice that the curves settle into clear "bands" depending on the relative value of M_{Norm}. Indeed, from Fig.4.3-(A) it is apparent that the accumulation curves overlay on each other at relatively low shear rates (i.e., for $\dot{\gamma} \leq 107.75\text{s}^{-1}$ or equivalently for $M_{Norm} < 1$), but they branch off at higher ones (i.e., for $\dot{\gamma} \geq 169.03\text{s}^{-1}$ or equivalently for $M_{Norm} > 1$). The differences between the curves representing the accumulation of particles is most apparent for the dark blue symbols in Fig.4.3-(B), which are representative of the pentas at the smallest and the largest explored shear rates, i.e. 27.68s^{-1} and 265.69s^{-1}, respectively. Here, the curve at the largest shear rate (denoted by triangular symbols) has a significantly greater accumulation of particles than the one at lowest shear rate (circle symbols); thus, implying a shear induced enhancement of the generation of pentas. Interestingly, this phenomenon is better explicated by the mean rate of accumulation (MROA) of the curves as reported in Fig.4.3-(C); which has been determined by normalising the mean value of the time derivative of the accumulation curves by its maximum value. In Fig.4.3-(C) the MROA is reported against M_{Norm}, and it can be observed that for single particles the MROA decreases with increasing M_{Norm}; whereas, for dimers it stays relatively constant across the same range of explored M_{Norm}. In contrast, the MROA of the longer chain particles has a relatively low and constant value for $M_{Norm} < 1$, with a sharp increase for $M_{Norm} > 1$. At this point it is important to remind that, in these experiments the total number of individual polystyrene beads is constant, and therefore as chains of different length start to form, the number of single particles decreases. It follows that, at low M_{Norm}, particles are not able to form long chains and the MROA value of single particles is high. Whereas, as the shear rate increases to a point where the M_{Norm} is greater than 1, the elastic

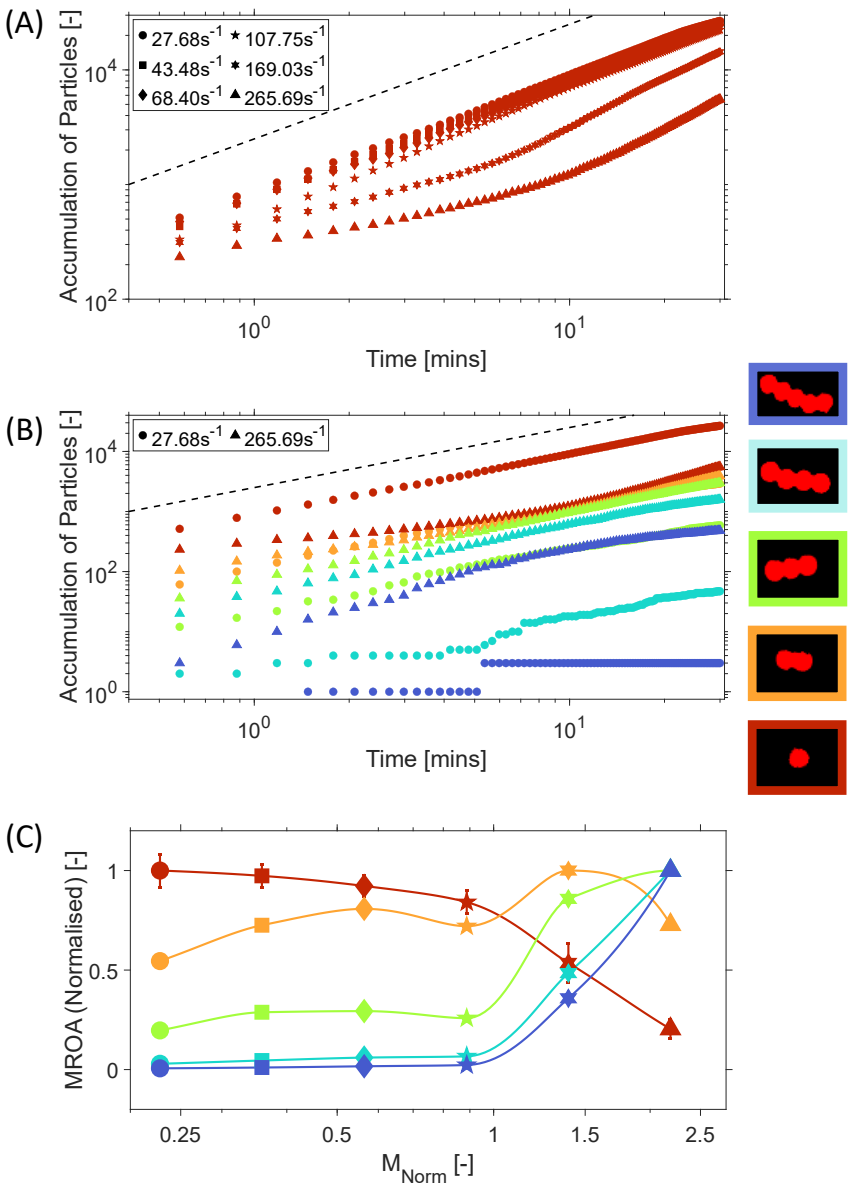

Figure 4.3: (A) Accumulation of particles for a chain length of 1 *versus* time for shear rates ranging from 27.68s^{-1} to 265.69s^{-1}. Each curve has been down-sampled for easier identification and the dashed black line indicates a linear growth. (B) Accumulation of particles for each chain length *versus* time for shear rates of 27.68s^{-1} and 265.69s^{-1}. As in (A) each curve has been down-sampled for easier identification and the dashed black line indicates a linear growth. (C) Mean rate of accumulation (MROA), normalised by the maximum MROA for each particle chain length *versus* M_{Norm}. The colours associated with each curve represent a particle chain length as for by the outline of the single, dimer, trimer, tetra and penta images on the right side. The outputs shown in this figure were obtained in triplicates.

instability of the PAM solution enhances the chaining, which results in a significant drop of the MROA value for the single particles, while the MROA of the trimers, tetras and pentas increases rapidly.

Relative Population of Chains

A complementary method to analyse the progression of FISA within the sample at different shear rates, is by identifying the relative population of each chain length in the image frame. To achieve this, the percentage of particles was calculated by taking the ratio between each chain length and the total number of particles identified in each frame, as shown in Fig.4.4.

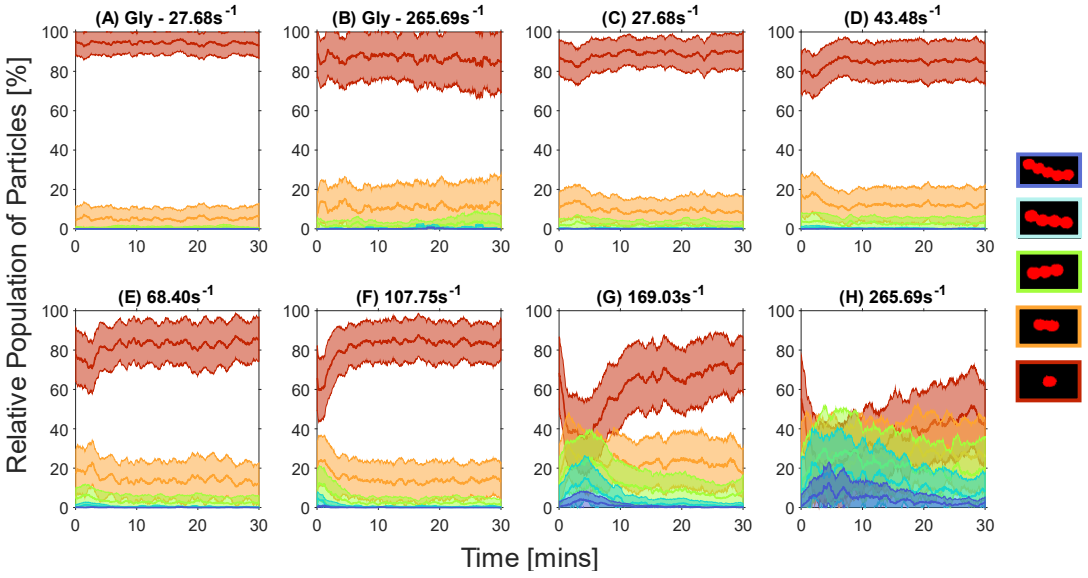

Figure 4.4: Relative population of particle chains (singles, dimers, trimers, tetras and pentas) *versus* time. (A and B) Particle suspension in glycerol/water mixture at a shear rates of $27.68s^{-1}$ and $265.69s^{-1}$, respectively. (C-H) PAM solutions at shear rates spanning from $27.68s^{-1}$ to $265.69s^{-1}$, with related values reported in table 4.1, respectively. The shaded areas are the standard deviation associated with the experimental triplicates and each curve has been smoothed by using a moving average window of 30s.

In particular, in Fig.4.4-(A-B) are reported the relative population of particle chains for suspensions made with glycerol/water mixture and measured at the two extremes of the range of explored shear rates (i.e., $27.68s^{-1}$ and $265.69s^{-1}$). From these diagrams it is apparent that no significant changes occur and that the mean percentage of single particles identified in the image frames stays well above 80%; whereas, for all the other particle chain sizes, it remains well below 20%. Thus confirming that chaining does not occur in Newtonian fluids. Interestingly, this is not the case of particle suspensions in the viscoelastic solution employed in this work. Indeed, as shown in Fig.4.4-(C-F), there is an initial fall of the mean percentage of single particles whose magnitude increases with the applied shear rate. This is followed by a corresponding rise in the mean percentage of longer chains, all within the first 5 minutes from the start of the experiments. Then the percentage of single

particles begins to climb back to an almost steady value for the duration of the experiment, which is higher than 80% for $M_{Norm} < 1$ and lower than 80% for $M_{Norm} > 1$. A similar, but opposite behaviour is seen for the longer particle chains, where an initial increase of their population is observed over the same time scale (i.e., 5min), followed by a decrease towards a steady value. One could argue that, a possible explanation of such dynamic process could be related to the migration of single particles and chains from/into the focal plane; however, the complementarity of these processes between the single particles and the chains (i.e., the decrease/increase in single particles is complemented by the increase/decrease in the percentage of dimers, trimers, tetras and pentas) implies (i) that the total number of particles is constant during the measurement and (ii) that longer chain particles are breaking down back to single particles.

Alignment Factor

An additional method to analyse the progression of FISA is by means of the alignment factor (A_f), as described by Pasquino *et al.* [125], which is defined as:

$$A_f = \frac{\sum_{L=1}^{L_{max}} N_L L^2}{\sum_{L=1}^{L_{max}} N_L L}, \tag{4.10}$$

where L is the chain length and N_L is the number of chains of a given length L in an image frame. As suggested by its name, A_f is a measure of bead alignment in a given image frame and will always have a value ≥ 1, where $A_f = 1$ is achievable *if and only if* there were solely single beads in the image frame. As stated by Pasquino *et al.* [125], A_f bares a resemblance to the weight average molecular weight of polymer chains and as such chains of longer length have greater impact on A_f.

In Fig.4.5-(A) we report the alignment factor for the same set of experiments analysed earlier in Fig.4.3 and 4.4. From Fig.4.5-(A) it can be seen that at relatively short times, all curves show an increase of A_f up to a maximum value, whose amplitude increases proportionally to the shear rate, while its abscissa is inversely proportional to $\dot{\gamma}$ for $M_{Norm} < 1$ and remains almost constant for $M_{Norm} > 1$. After reaching a maximum, all the curves tend to exponentially decrease towards a steady-state value at long times. This is the first time in literature that such behaviour of A_f is reported, as it was expected that A_f would have increased monotonically until a plateau value at long times, as described by Pasquino *et al.* [125, 126]. However, it must be said that, their focal plane was positioned at the wall of the shear cell and therefore particle migration[124, 125] towards the plate continued to supply the area with new beads. In this work, the focal plane was placed at the centre of the fluid

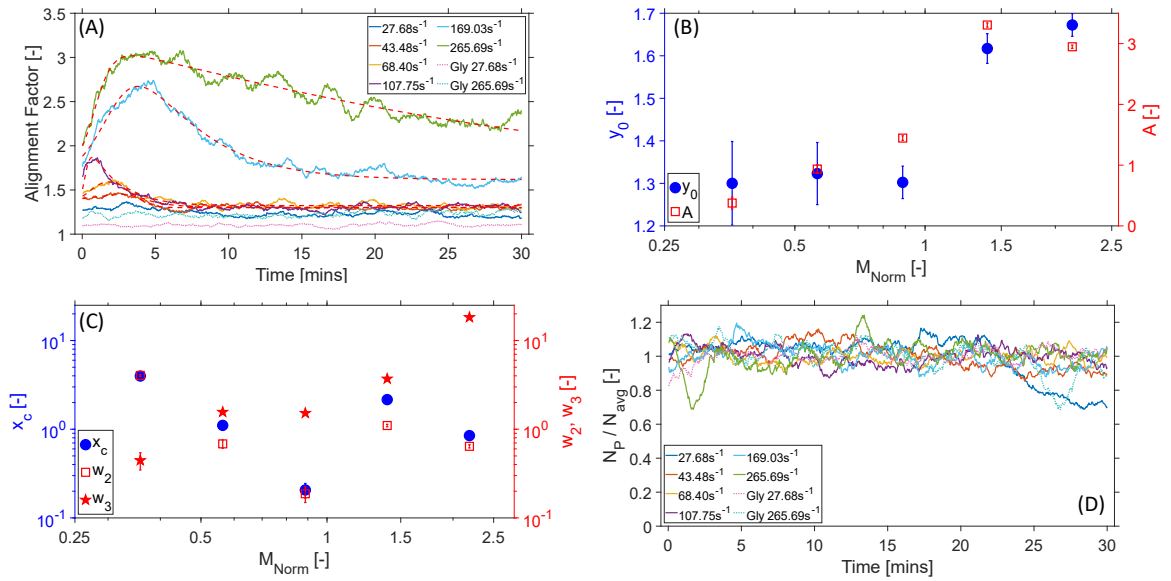

Figure 4.5: (A) Alignment factor curves (averaged over triplicates) for the explored shear rates, including the two set of measurements performed on the 97% glycerol/water mixture (Gly) as control (dotted lines). The red dashed lines represent Eq.(4.11) as fitting function. Notice that, each curve has been smoothed by using a moving average window of 60s width. (B) The resulting fitting parameters y_0 and A of Eq.(4.11) *versus* M_{Norm}. (C) The resulting fitting parameters x_c (left axis), w_2 and w_3 (right axis) of Eq.(4.11) *versus* M_{Norm}. The standard deviation of the fitting function is depicted as error bars in (B) and (C). (D) The normalised number of particles *versus* time, used to analyse the migration of particles away from the focal plane. Here, each curve has been smoothed by using a moving average window of 30s width.

chamber and therefore we again posit that the decrease of A_f at long-times may be due to either (i) particle migration away from the centre of the channel (this being a possible explanation that is not supported by the experimental evidence reported in this work), or (ii) longer chain particles breaking down to single particles (which is the thesis we support).

To better understand the temporal behaviour of A_f, we performed a best fit of the curves by means of the following asymmetric double sigmoid function[146] (also known as piecewise logistic function):

$$y = y_0 + A\frac{1}{1+e^{-\frac{x-x_c+w_1/2}{w_2}}}\left(1-\frac{1}{1+e^{-\frac{x-x_c-w_1/2}{w_3}}}\right), \tag{4.11}$$

where y_0 is the steady state value, A is the amplitude, x_c is the peak center, w_1 is the curve width, w_2 and w_3 are shape parameters. For the fitting curves shown in Fig.4.5-(A), it was found that $w_1 = 0$ for all fits; whereas, the remaining parameters were different from zero and they are plotted against M_{Norm} in Fig.4.5-(B) and (C). From these figures, it can be seen

that y_0 is almost constant for $M_{Norm} < 1$, with a significant increase for $M_{Norm} > 1$. Whereas, the amplitude A shows a progressive increase with M_{Norm}; although, it could be argued that there is an initial shallow increase for $M_{Norm} < 1$ and then a relatively sharp increase for $M_{Norm} > 1$. From Fig.4.5-(C) one will notice that x_c (the peak centre) behaves rather erratically when plotted against M_{Norm}. Indeed, it initially decreases for $M_{Norm} < 1$ (which corresponds to a reduction in time for the peak to occur in Fig.4.5-(A)); however, as M_{Norm} exceeds 1, there is first a sharp increase in x_c and then it starts decreasing again. Interestingly, a similar behaviour is shown by w_2. Finally, w_3 is the 'shape parameter' for the curve after its peak, and an increase in its value would suggest an increase of the characteristic "*relaxation time*" of A_f. Thus suggesting that the degradation of the particle chains is controlled by a different physical process than the one governing the generation of particle chains.

Overall, the above analysis of the fitting parameters indicates a clear change in behaviour of the particle chaining phenomena as M_{Norm} exceeds 1; with a sharp enhancement of the chaining that correlates well with the onset of the elastic instability of the fluid.

Flow induced particle chains break down

Both the analysis of the relative chain length population and the A_f have raised the same question: is the decrease in FISA at long-times due to the migration of longer chain particles away from the focal plane or is it due to the break down of these same particle chains back to single particles?

To address this question, we have followed the approach introduced by Mirsepassi *et al.* [147], whereby one could reveal the existence of migration during flow by normalising the change in the number of particles in each frame (independently on whether they are single or belonging to chains of different length) to the average number of particles in each image determined over the entire measurement duration. In Fig.4.5-(D) we report the results of such analysis with a moving average window of 30s width. Despite the existence of significant fluctuations, all curves fluctuates around a constant value equal to 1, which suggests that the average number of particles in the bulk of the PAM solution does not change during the (30mins) measurements; hence, it is unlikely that the migration of particles out of the focal plane can fully justify the decrease in A_f, although it cannot be fully discarded. Additionally, the sedimentation time of the particles was considered, due to the decrease in the 27.68s^{-1} PAM curve after $\sim$ 20mins, but no agglomerates were observed at the bottom of the shear cell after the experiments, suggesting its influence is insignificant and therefore the decrease seen in this curve is caused by a yet unknown phenomenon. These results further corroborate our

hypothesis that the reduction in FISA at long-times is likely to be due to the longer particle chains breaking down back into shorter chain lengths.

This poses a further question: what would cause the particles chains to break down? A possible cause would involve the flow induced disentanglement of the polymer chains, as described by Vasquez *et al.* [148]. This phenomenon would occur on time scales much longer than the characteristic relaxation time (λ) and would produce a drop in the viscoelastic properties of PAM solutions during shear; thus dimming the elastic character of the fluid and therefore potentially reversing the particle chaining (as in Fig.4.5-(A)) by shifting the M_{Norm} towards values lower than one. Interestingly, this thesis is supported by the experimental evidences reported in a recent study by Tran and Clarke [132], where they performed parallel-superposition shear measurements to reveal (i.e., see Figure 2 of their study) a significant reduction of the longest characteristic relaxation time of high molecular weight PAM solutions as function of the imposed shear rate. These results unveil a shift of the low-frequency crossover of the viscoelastic moduli towards higher frequencies, which would imply a reduction of the fluid's longest characteristic relaxation time. However, the results reported by Tran and Clarke [132] were recorded at steady state and therefore they do not inform on the dynamics of the above phenomenon, which one would expect to be potentially correlated to the characteristic time-scales shown in Fig.4.5.

In Fig.4.6 we report, for the first time in literature, an experimental evidence revealing the time scale of the phenomenon described above. In particular, Fig.4.6 shows the normalized viscoelastic moduli *versus* time of a PAM solution at concentration of 0.07%wt as obtained by two parallel superposition shear measurements performed at shear rates of 0.49s^{-1} and 0.79s^{-1}, respectively. The measurements were performed at a constant frequency of 0.4Hz and the moduli normalized by their value at time equal to 10s (i.e., $G'_{||}/G'_{||}|_{t=10}$ and $G''_{||}/G''_{||}|_{t=10}$). The two lines indicate the values of $1\pm$ standard deviation of the viscoelastic moduli *versus* time of the same solution as above, but measured at zero shear (i.e., as obtained from a time-sweep of a small amplitude oscillatory measurement); in this case the moduli were normalized by their mean values, respectively.

From Fig.4.6 it is possible to argue that: (i) there is a significant reduction over the time of the elastic component of the polymer solution (i.e., $G'_{||} \propto t^{-1/15}$), when the fluid is subjected to a continuous shear rate (thus supporting the thesis of polymers disentanglement); (ii) the viscous modulus is significantly less affected than the elastic component (because the polymer concentration and its molecular conformation are almost constant during the measurement); (iii) most of the significant changes of the viscoelastic properties of the solution

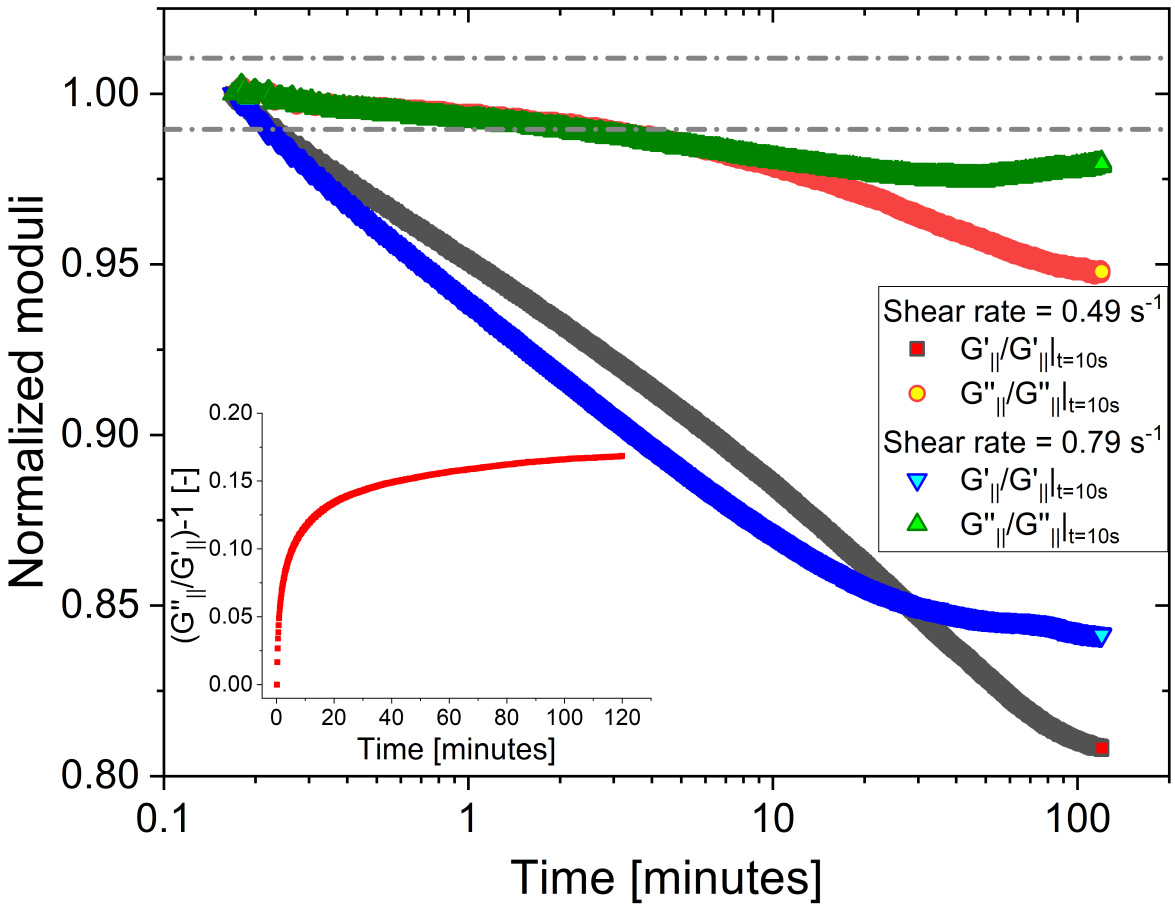

Figure 4.6: (Symbols) The normalized viscoelastic moduli *versus* time of a PAM solution at concentration of 0.07%wt as measured by means of two parallel superposition shear measurements performed at shear rates of 0.49s^{-1} and 0.79s^{-1}, respectively. The moduli were measured at a constant frequency of 0.4Hz and normalized by their value at time 10s. The two dashed lines indicate the values of $1\pm$ standard deviation of the viscoelastic moduli (measured at a constant frequency of 0.4Hz) *versus* time of the same solution as above, but at zero shear (i.e., as obtained from a time-sweep of a small amplitude oscillatory measurement); in this case the moduli were normalized by their mean values, respectively. The inset shows the averaged ratio of the viscous modulus to that of the elastic modulus minus one for the two set of measurements shown in the main. *Author Declaration: The results in this figure were collected by Anand Raghavan [c] and Andrew Clarke [c] and, the figure was designed by Manlio Tassieri [a].*

occur within the first ~ 20 minutes of the measurement (as revealed by the data shown in the inset), which is in very good agreement with the time-scales of the alignment factor shown in Fig.4.5, especially for those measurements having the same shear rates.

4.5 Conclusions

In this work we have studied the flow-induced self-assembly (FISA) of particles suspended into both Newtonian and viscoelastic fluids. This has been achieved by means of a bespoke shear cell that has allowed us to monitor the dynamics of the particle chain 'generation' and for the first time in literature 'degradation'. In particular, the adoption of a viscoelastic fluid characterised by a clear transition between a shear thinning behaviour (i.e., with a decreasing viscosity) at relatively low frequencies (or equivalently at low shear rates) and a shear-thickening character (onset of elastic instability) at relatively high frequencies (or shear rates) and the fine tuning of the applied shear rates, have allowed us to investigate the particle chaining phenomenon across a M_{Norm} of 1. In particular, this study has led to the following key findings: (i) we have corroborated that particles suspended into Newtonian fluids do not show FISA enhancement at different shear rates; (ii) FISA within viscoelastic fluids is significantly greater than in Newtonian fluids, when compared over the same range of shear rates; (iii) for M_{Norm} higher than 1, the onset of the elastic turbulence of the viscoelastic fluid correlates strongly with the enhancement of FISA; (iv) particle chains break apart when a constant shear is applied for sufficiently long-time (i.e. much longer than the fluids' longest relaxation time). (v) We provide for the first time in literature experimental evidence of a significant reduction of the fluid's elastic character when a continuous flow is applied for sufficiently long time. Points (iv) and (v) have been corroborated (via private communication) by means of computational fluid dynamics simulations kindly performed by Pier Luca Maffettone and Gaetano D'Avino (data not reported here), whose outcomes will be published in a separate publication.

Finally, we envisage that, in future works the adoption of imaging systems with a wider field of view capable of capturing images of the whole shear cell at higher resolution and acquisition rate, would allow a deeper understanding of the dynamics of both FISA and chain breakdown phenomena. Moreover, further investigation of the rheological properties of PAM solutions by means of parallel superposition shear measurements, may elucidate the newly discovered phenomenon of the reduction of the fluid's viscoelastic properties when subjected to a continuous flow for sufficiently long time.

Acknowledgements

The authors thank Rossana Pasquino and Francesco Del Giudice for the informative discussions. We thank Pier Luca Maffettone and Gaetano D'Avino for corroborating our ex-

perimental results by means of computational fluid dynamics simulations. This work was supported by the EPSRC CDT in Intelligent Sensing and Measurement, Grant Number EP/L016753/1.

Author contributions statement

M.T. conceived the experiment(s), M.G.S. conducted the experiments with the shear cell, M.G.S. and M.T. analysed the data, M.G.S. wrote the manuscript, G.M.G. & M.T. conducted the microrheology measurements, T.F. & A.L. supervised the shear cell measurements, A.C. & A.R. conducted the bulk rheology measurements. All authors contributed to the drafting of the manuscript.

Chapter 5

Conclusions and Future Work

This thesis has compiled a series of original works on various areas within the field of microrheology. This chapter will summarise the main findings of each of those works, the future work that could be performed to advance the specific area and, where applicable, how the work has impacted the wider community.

Chapter 2 presented an open-access MATLAB code called "i-RheoFT" that is able to evaluate the Fourier transform of any time-dependent generic function which vanishes for negative times, with a finite number of data points which do not need to be equally spaced, and sampled over a finite range. The effectiveness of the MATLAB code was investigated by evaluating the Fourier transform of two functions; a single exponential decay describing the dynamics of a Maxwell fluid and a function that resembles the mean squared displacement of a weakly trapped particle suspended in a non-Newtonian fluid. The density of initial experimental data points and signal-to-noise ratio was varied for each function and the interpolation function used in virtual oversampling was examined to determine i-RheoFT's efficacy for different experimental conditions. The main findings of this study were that if the density of initial data points and the signal-to-noise ratio were high, the three interpolation functions used in oversampling, "Spline", "Makima" and "PCHIP", all performed well with the spline function showing the best performance. Additionally, there exists a threshold value, for both the density of initial points and signal-to-noise ratio, at which all three interpolation functions performed poorly with the spline function performing the worst.

One of the main goals of i-RheoFT was to provide researchers with the means of evaluating the Fourier transform of their discrete time-dependent signals, and if necessary calculate the LVE properties of materials. Work carried out after the publication of this chapter involved the development of two open-source applications that are able to compute the complex shear modulus. The first evaluates the Fourier transform of the time-dependent step

stress or strain measurement from bulk rheology [1] and the second evaluates the Fourier transform of the force and indentation data from atomic force microscopy measurements [2]. The work presented in chapter 2 has been utilised in a study by Mendonca *et al.* [3] to characterise hydrogels using their new "OptoRheo" instrument which has been developed to explore drug transport through complex cell culture matrices and optimise the design of new disease models. Additionally, i-RheoFT was used in a study by Matheson *et al.* [4] aimed at providing a new analytical framework for 3D trajectories, produced from passive MOT, to help minimise the characterisation error associated with anisotropic optical traps. Furthermore, the work presented in chapter 2 has been cited in a study by Hardiman *et al.* [5], who used the OptoRheo instrument to perform passive microrheology experiments on living cells, by chemically binding the particle to the cell's surface, in order to measure cell stiffness over the course of hours.

Chapter 3 is an original work and has been published in AIP Advances [70]. This work investigates the effect experimental measurement time has on the accuracy of conventional passive MOT measurements through the simulation of 2D optically trapped particle trajectories, suspended in a Newtonian fluid, across a three-decade range of viscosities. Additionally, using these trajectories, a machine learning algorithm was developed and subsequently trained to extract features from only one second of trajectory and provide a prediction of the viscosity. This work displays how conventional passive MOT, with its requirement to have sufficiently long measurement times with many individual readings, is unsuitable for use with living systems. Furthermore, chapter 3, provides a way of estimating the experimental duration required to reduce the uncertainty of the measurement to 1%. Moreover, this work presents a viable enhancement to passive MOT through the use of machine learning, which can reduce the measurement time from tens of minutes to one second while returning a measurement uncertainty that is 5 times smaller than conventional passive MOT for the same conditions. Interestingly, this machine learning algorithm performed well even on real data and was able to predict the viscosity to a high accuracy. This combination of machine learning and conventional MOT has been shown to work well with Newtonian fluids and it is believed that it will open the door for accurate microrheology studies of living systems, provided there is substantial data available to train the model. The next steps would be to increase the scope of the machine learning algorithm to include viscoelastic fluids, which would more closely resemble living systems of interest, and use the algorithm to predict the frequency dependent LVE properties rather than just the viscosity.

Chapter 4, published in Physics of Fluids [109], investigates the flow-induced self-

assembly of particles, suspended in a shear thinning 0.07%*wt* Polyacrylamide solution, while experiencing simple shear flow provided by a bespoke shear cell. In particular, this study was targeted at the transition of the viscoelastic fluid from a shear thinning (at relatively low frequencies) to a shear-thickening character (at relatively high frequencies) caused by the onset of elastic instability. This study has led to a number of key findings: (i) we have corroborated that particles suspended into Newtonian fluids do not show FISA enhancement at different shear rates; (ii) FISA within viscoelastic fluids is significantly greater than in Newtonian fluids, when compared over the same range of shear rates; (iii) for M_{Norm} higher than 1, the onset of the elastic turbulence of the viscoelastic fluid correlates strongly with the enhancement of FISA; (iv) particle chains break apart when a constant shear is applied for sufficiently long-time (i.e. much longer than the fluids' longest relaxation time). (v) We provide for the first time in literature experimental evidence of a significant reduction of the fluid's elastic character when a continuous flow is applied for sufficiently long time. Future work could include the adoption of imaging systems with a wider field of view capable of capturing images of the whole shear cell at higher resolution and acquisition rate, would allow a deeper understanding of the dynamics of both FISA and chain breakdown phenomena. Moreover, further investigation of the rheological properties of PAM solutions by means of parallel superposition shear measurements, may elucidate the newly discovered phenomenon of the reduction of the fluid's viscoelastic properties when subjected to a continuous flow for sufficiently long time.

Bibliography

1. Smith, M. & Tassieri, M. *I-rheo* May 2022. `https://researchdata.gla.ac.uk/1289/`.
2. Smith, M. & Tassieri, M. *I-rheo-AFM2* June 2022. `https://researchdata.gla.ac.uk/1311/`.
3. Mendonca, T. *et al.* OptoRheo: Simultaneous in situ micro-mechanical sensing and imaging of live 3D biological systems. *Communications Biology* **6,** 463 (2023).
4. Matheson, A. B. *et al.* An analytical framework for 3D microrheology measurements using an optical trap (2022).
5. Hardiman, W. *et al.* Living Cells as an Analog of Optical Tweezers-A Non-Invasive Microrheology Approach. *Available at SSRN 4325474.*
6. Weber, W. Ueber die elasticitaet der seidenfaeden. *Annalen der Physik* **110,** 247–257 (1835).
7. Kohlrausch, F. W. *Pogg Ann Physik* **119,** 337–368 (1863).
8. Wiechert, E. *Wied Ann Phys Lpz* **50,** 335–348, 546–570 (1893).
9. Maxwell, J. C. IV. On the dynamical theory of gases. *Philosophical transactions of the Royal Society of London,* 49–88 (1867).
10. Boltzmann, L. Zur theorie der elastischen nachwirkung. *Annalen der Physik* **241,** 430–432 (1878).
11. Poynting, J. & Thomson, J. Elasticity. *Properties of Matter,* 53–61 (1902).
12. Barnes, H. A., Hutton, J. F. & Walters, K. *An introduction to rheology* (Elsevier, 1989).
13. Mezger, T. *The rheology handbook: for users of rotational and oscillatory rheometers* (European Coatings, 2020).

14. Dos Santos, D., Carastan, D., Tavares, L. & Batalha, G. in *Comprehensive Materials Processing* (eds Hashmi, S., Batalha, G. F., Van Tyne, C. J. & Yilbas, B.) 37–63 (Elsevier, Oxford, 2014). ISBN: 978-0-08-096533-8. https://www.sciencedirect.com/science/article/pii/B9780080965321002053.

15. Ferry, J. D. *Viscoelastic properties of polymers* (John Wiley & Sons, 1980).

16. Macosko, C. W. Rheology principles. *Measurements and Applications* (1994).

17. Rubinstein, M., Colby, R. H., *et al. Polymer physics* (Oxford university press New York, 2003).

18. McLeish, T. Tube theory of entangled polymer dynamics. *Advances in physics* **51,** 1379–1527 (2002).

19. Geri, M. *et al.* Time-resolved mechanical spectroscopy of soft materials via optimally windowed chirps. *Physical Review X* **8,** 041042 (2018).

20. Tassieri, M. *et al.* i-Rheo: Measuring the materials' linear viscoelastic properties "in a step"! *Journal of Rheology* **60,** 649–660 (2016).

21. Evans, R. Transforming from time to frequency without artefacts. *arXiv preprint arXiv:0911.4652* (2009).

22. Chim, Y. H. *et al.* A one-step procedure to probe the viscoelastic properties of cells by Atomic Force Microscopy. *Scientific reports* **8,** 1–12 (2018).

23. Tassieri, M., Ramírez, J., Karayiannis, N. C., Sukumaran, S. K. & Masubuchi, Y. i-rheo gt: Transforming from time to frequency domain without artifacts. *Macromolecules* **51,** 5055–5068 (2018).

24. Tassieri, M. Microrheology with optical tweezers: peaks & troughs. *Current Opinion in Colloid & Interface Science* **43,** 39–51 (2019).

25. Block, S. M., Blair, D. F. & Berg, H. C. Compliance of bacterial flagella measured with optical tweezers. *Nature* **338,** 514–518 (1989).

26. Finer, J. T., Simmons, R. M. & Spudich, J. A. Single myosin molecule mechanics: piconewton forces and nanometre steps. *Nature* **368,** 113–119 (1994).

27. Yoon, Y.-Z., Kotar, J., Yoon, G. & Cicuta, P. The nonlinear mechanical response of the red blood cell. *Physical biology* **5,** 036007 (2008).

28. Ashkin, A. & Dziedzic, J. M. Optical trapping and manipulation of viruses and bacteria. *Science* **235,** 1517–1520 (1987).

29. Tskhovrebova, L., Trinick, J., Sleep, J. & Simmons, R. Elasticity and unfolding of single molecules of the giant muscle protein titin. *Nature* **387,** 308–312 (1997).

30. Mehta, A. D., Rief, M., Spudich, J. A., Smith, D. A. & Simmons, R. M. Single-molecule biomechanics with optical methods. *Science* **283,** 1689–1695 (1999).

31. Mao, Y., Nielsen, P. & Ali, J. Passive and active microrheology for biomedical systems. *Frontiers in Bioengineering and Biotechnology* **10,** 916354 (2022).

32. Ashkin, A. Acceleration and trapping of particles by radiation pressure. *Physical review letters* **24,** 156 (1970).

33. Svoboda, K. & Block, S. M. Biological applications of optical forces. *Annual review of biophysics and biomolecular structure* **23,** 247–285 (1994).

34. Diekmann, R. *et al.* Nanoscopy of bacterial cells immobilized by holographic optical tweezers. *Nature communications* **7,** 13711 (2016).

35. Davies, J. F. & Wilson, K. R. Raman spectroscopy of isotopic water diffusion in ultraviscous, glassy, and gel states in aerosol by use of optical tweezers. *Analytical chemistry* **88,** 2361–2366 (2016).

36. Ayala, Y. A. *et al.* Rheological properties of cells measured by optical tweezers. *BMC biophysics* **9,** 1–11 (2016).

37. Weigand, W. *et al.* Active microrheology determines scale-dependent material properties of Chaetopterus mucus. *PloS one* **12,** e0176732 (2017).

38. Kim, H. *et al.* In situ single-atom array synthesis using dynamic holographic optical tweezers. *Nature communications* **7,** 13317 (2016).

39. Tassieri, M. *Microrheology with Optical Tweezers: Principles and Applications* (CRC Press, 2016).

40. Maxwell, J. C. *A treatise on electricity and magnetism* (Oxford: Clarendon Press, 1873).

41. Lemons, D. S. & Gythiel, A. Paul langevin's 1908 paper "on the theory of brownian motion"["sur la théorie du mouvement brownien," cr acad. sci.(paris) 146, 530–533 (1908)]. *American Journal of Physics* **65,** 1079–1081 (1997).

42. Berg-Sørensen, K. & Flyvbjerg, H. Power spectrum analysis for optical tweezers. *Review of Scientific Instruments* **75,** 594–612 (2004).

43. Tassieri, M. *et al.* Measuring storage and loss moduli using optical tweezers: Broadband microrheology. *Physical Review E* **81,** 026308 (2010).

44. Tassieri, M., Evans, R., Warren, R. L., Bailey, N. J. & Cooper, J. M. Microrheology with optical tweezers: data analysis. *New Journal of Physics* **14,** 115032 (2012).

45. Preece, D. *et al.* Optical tweezers: wideband microrheology. *Journal of optics* **13,** 044022 (2011).

46. Gittes, F., Schnurr, B., Olmsted, P., MacKintosh, F. C. & Schmidt, C. F. Microscopic viscoelasticity: shear moduli of soft materials determined from thermal fluctuations. *Physical review letters* **79,** 3286 (1997).

47. Schnurr, B., Gittes, F., MacKintosh, F. & Schmidt, C. Determining microscopic viscoelasticity in flexible and semiflexible polymer networks from thermal fluctuations. *Macromolecules* **30,** 7781–7792 (1997).

48. MacKintosh, F. & Schmidt, C. Microrheology. *Current opinion in colloid & interface science* **4,** 300–307 (1999).

49. Nishi, K., Kilfoil, M. L., Schmidt, C. F. & MacKintosh, F. A symmetrical method to obtain shear moduli from microrheology. *Soft Matter* **14,** 3716–3723 (2018).

50. Tassieri, M. Comment on "A symmetrical method to obtain shear moduli from microrheology" by K. Nishi, ML Kilfoil, CF Schmidt, and FC MacKintosh, Soft Matter, 2018, 14, 3716. *Soft Matter* **14,** 8666–8670 (2018).

51. Smith, M. G., Gibson, G. M. & Tassieri, M. i-RheoFT: Fourier transforming sampled functions without artefacts. *Scientific Reports* **11,** 1–12 (2021).

52. Ewen, B., Mours, M., Richter, D., Shiga, T. & Winter, H. *Neutron spin echo spectroscopy viscoelasticity rheology* (Springer Science & Business Media, 1997).

53. Richter, D., Monkenbusch, M., Arbe, A. & Colmenero, J. Neutron spin echo in polymer systems. *Neutron Spin Echo in Polymer Systems: -/-,* 1–221 (2005).

54. Rizzi, L. G. & Tassieri, M. Microrheology of Biological Specimens. *Encyclopedia of Analytical Chemistry* (2018).

55. Waigh, T. A. Advances in the microrheology of complex fluids. *Reports on Progress in Physics* **79,** 074601 (2016).

56. Lodge, J. M. & Heyes, D. Transient colloidal gels by Brownian dynamics computer simulation. *Physical Chemistry Chemical Physics* **1,** 2119–2130 (1999).

57. Berne, B. J. & Pecora, R. *Dynamic light scattering: with applications to chemistry, biology, and physics* (Courier Corporation, 2000).

58. Pine, D. J., Weitz, D. A., Chaikin, P. M. & Herbolzheimer, E. Diffusing wave spectroscopy. *Phys. Rev. Lett.* **60,** 1134–1137. https://link.aps.org/doi/10.1103/PhysRevLett.60.1134 (12 Mar. 1988).

59. Tassieri, M. *et al.* Dynamics of semiflexible polymer solutions in the highly entangled regime. *Physical Review Letters* **101,** 198301 (2008).

60. Tassieri, M. Dynamics of semiflexible polymer solutions in the tightly entangled concentration regime. *Macromolecules* **50,** 5611–5618 (2017).

61. Evans, R., Tassieri, M., Auhl, D. & Waigh, T. A. Direct conversion of rheological compliance measurements into storage and loss moduli. *Physical Review E* **80,** 012501 (2009).

62. Peddireddy, K. R. *et al.* Unexpected entanglement dynamics in semidilute blends of supercoiled and ring DNA. *Soft Matter* **16,** 152–161 (2020).

63. Alshareedah, I., Moosa, M. M., Pham, M., Potoyan, D. A. & Banerjee, P. R. Programmable viscoelasticity in protein-RNA condensates with disordered sticker-spacer polypeptides. *Nature communications* **12,** 6620 (2021).

64. MathWorks. *Spline, Cubic spline data interpolation* ((accessed September 28, 2020)). https://uk.mathworks.com/help/matlab/ref/spline.html.

65. MathWorks. *Makima, modified akima piecewise cubic hermite interpolation* ((accessed September 28, 2020)). https://uk.mathworks.com/help/matlab/ref/makima.html.

66. MathWorks. *PCHIP, Piecewise Cubic Hermite Interpolating Polynomial (PCHIP)* ((accessed September 28, 2020)). https://uk.mathworks.com/help/matlab/ref/pchip.html.

67. Lathi, B. P. & Green, R. A. *Linear systems and signals* (Oxford University Press New York, 2005).

68. Akima, H. A new method of interpolation and smooth curve fitting based on local procedures. *Journal of the ACM (JACM)* **17,** 589–602 (1970).

69. Akima, H. A method of bivariate interpolation and smooth surface fitting based on local procedures. *Communications of the ACM* **17,** 18–20 (1974).

70. Smith, M. G. *et al.* Machine learning opens a doorway for microrheology with optical tweezers in living systems. *AIP Advances* **13** (2023).

71. Ashkin, A. & Dziedzic, J. Optical levitation by radiation pressure. *Applied Physics Letters* **19,** 283–285 (1971).

72. Ashkin, A., Dziedzic, J. M., Bjorkholm, J. E. & Chu, S. Observation of a single-beam gradient force optical trap for dielectric particles. *Optics letters* **11,** 288–290 (1986).

73. Madsen, L. S. *et al.* Ultrafast viscosity measurement with ballistic optical tweezers. *Nature Photonics* **15,** 386–392 (2021).

74. Capitanio, M. *et al.* Ultrafast force-clamp spectroscopy of single molecules reveals load dependence of myosin working stroke. *Nature methods* **9,** 1013–1019 (2012).

75. Squires, T. M. & Mason, T. G. Fluid mechanics of microrheology. *Annual review of fluid mechanics* **42,** 413–438 (2010).

76. Waigh, T. A. Microrheology of complex fluids. *Reports on progress in physics* **68,** 685 (2005).

77. Hoffman, B. D. & Crocker, J. C. Cell mechanics: dissecting the physical responses of cells to force. *Annual review of biomedical engineering* **11,** 259–288 (2009).

78. Tassieri, M. in *Microrheology with Optical Tweezers* 235–272 (Jenny Stanford Publishing, 2016).

79. Valentine, M., Dewalt, L. & Ou-Yang, H. Forces on a colloidal particle in a polymer solution: a study using optical tweezers. *Journal of Physics: Condensed Matter* **8,** 9477 (1996).

80. Tassieri, M. Linear microrheology with optical tweezers of living cells 'is not an option'! *Soft Matter* **11,** 5792–5798 (2015).

81. Harrison, A. W., Kenwright, D. A., Waigh, T. A., Woodman, P. G. & Allan, V. J. Modes of correlated angular motion in live cells across three distinct time scales. *Physical biology* **10,** 036002 (2013).

82. Mizuno, D., Tardin, C., Schmidt, C. F. & MacKintosh, F. C. Nonequilibrium mechanics of active cytoskeletal networks. *Science* **315,** 370–373 (2007).

83. Toyota, T., Head, D. A., Schmidt, C. F. & Mizuno, D. Non-Gaussian athermal fluctuations in active gels. *Soft Matter* **7,** 3234–3239 (2011).

84. Alberts, B. *et al. Molecular Biology of the Cell* 6th, 1–1464 (W.W. Norton & Company, 2015).

85. Tassieri, M. *et al.* Microrheology with Optical Tweezers: Measuring the relative viscosity of solutions 'at a glance'. *Scientific reports* **5,** 8831 (2015).

86. Volpe, G. & Volpe, G. Simulation of a Brownian particle in an optical trap. *American Journal of Physics* **81,** 224–230 (2013).

87. Pommella, A. *et al.* Using optical tweezers for the characterization of polyelectrolyte solutions with very low viscoelasticity. *Langmuir* **29,** 9224–9230 (2013).

88. Lee, M., Gibson, G., Phillips, D., Padgett, M. & Tassieri, M. Dynamic stereo microscopy for studying particle sedimentation. *Optics express* **22,** 4671–4677 (2014).

89. Mason, T. G. & Weitz, D. A. Optical measurements of frequency-dependent linear viscoelastic moduli of complex fluids. *Physical review letters* **74,** 1250 (1995).

90. Bowman, R. W. *et al.* "Red Tweezers": Fast, customisable hologram generation for optical tweezers. *Computer Physics Communications* **185,** 268–273 (2014).

91. Gibson, G. M., Leach, J., Keen, S., Wright, A. J. & Padgett, M. J. Measuring the accuracy of particle position and force in optical tweezers using high-speed video microscopy. *Optics express* **16,** 14561–14570 (2008).

92. Brunton, S. L., Noack, B. R. & Koumoutsakos, P. Machine learning for fluid mechanics. *Annual review of fluid mechanics* **52,** 477–508 (2020).

93. Hornik, K., Stinchcombe, M. & White, H. Multilayer feedforward networks are universal approximators. *Neural networks* **2,** 359–366 (1989).

94. Bishop, C. M. & Nasrabadi, N. M. *Pattern recognition and machine learning* **4** (Springer, 2006).

95. LeCun, Y., Bengio, Y. & Hinton, G. Deep learning. *nature* **521,** 436–444 (2015).

96. Goodfellow, I., Bengio, Y. & Courville, A. *Deep learning* (MIT press, 2016).

97. Rumelhart, D. E., Hinton, G. E. & Williams, R. J. Learning representations by back-propagating errors. *nature* **323,** 533–536 (1986).

98. LeCun, Y. *et al.* Backpropagation applied to handwritten zip code recognition. *Neural computation* **1,** 541–551 (1989).

99. LeCun, Y., Bengio, Y., *et al.* Convolutional networks for images, speech, and time series. *The handbook of brain theory and neural networks* **3361,** 1995 (1995).

100. MacKay, D. J. & Mac Kay, D. J. *Information theory, inference and learning algorithms* (Cambridge university press, 2003).

101. Kingma, D. P. & Ba, J. Adam: A method for stochastic optimization. *arXiv preprint arXiv:1412.6980* (2014).

102. Reiner, M. The deborah number. *Physics today* **17,** 62 (1964).

103. Matheson, A. B. *et al.* Microrheology with an anisotropic optical trap. *Frontiers in Physics* **9,** 621512 (2021).

104. Ashworth, J. *et al.* Peptide gels of fully-defined composition and mechanics for probing cell-cell and cell-matrix interactions in vitro. *Matrix Biology* **85,** 15–33 (2020).

105. Geonzon, L. C. *et al.* Microrheological properties and local structure of ι-carrageenan gels probed by using optical tweezers. *Food Hydrocolloids* **137,** 108325 (2023).

106. Yanagishima, T., Frenkel, D., Kotar, J. & Eiser, E. Real-time monitoring of complex moduli from micro-rheology. *Journal of physics: Condensed matter* **23,** 194118 (2011).

107. Ramírez, J., Sukumaran, S. K., Vorselaars, B. & Likhtman, A. E. Efficient on the fly calculation of time correlation functions in computer simulations. *The Journal of chemical physics* **133,** 154103 (2010).

108. Xu, J., Viasnoff, V. & Wirtz, D. Compliance of actin filament networks measured by particle-tracking microrheology and diffusing wave spectroscopy. *Rheologica acta* **37,** 387–398 (1998).

109. Smith, M. G. *et al.* The role of elastic instability on the self-assembly of particle chains in simple shear flow. *Physics of Fluids* **35,** 122017. ISSN: 1070-6631. eprint: https://pubs.aip.org/aip/pof/article-pdf/doi/10.1063/5.0182175/18271631/122017_1_5.0182175.pdf. https://doi.org/10.1063/5.0182175 (Dec. 2023).

110. Michele, J., Pätzold, R. & Donis, R. Alignment and aggregation effects in suspensions of spheres in non-Newtonian media. *Rheologica Acta* **16,** 317–321 (1977).

111. Vaia, R. A. & Giannelis, E. P. Polymer nanocomposites: status and opportunities. *MRS bulletin* **26,** 394–401 (2001).

112. Shewan, H. M. & Stokes, J. R. Review of techniques to manufacture micro-hydrogel particles for the food industry and their applications. *Journal of Food Engineering* **119,** 781–792 (2013).

113. Del Giudice, F. *et al.* Particle alignment in a viscoelastic liquid flowing in a square-shaped microchannel. *Lab on a Chip* **13,** 4263–4271 (2013).

114. Del Giudice, F. Simultaneous measurement of rheological properties in a microfluidic rheometer. *Physics of Fluids* **32,** 052001 (2020).

115. Charjouei Moghadam, M., Eilaghi, A. & Rezai, P. Elasto-inertial microparticle focusing in straight microchannels: A numerical parametric investigation. *Physics of Fluids* **33,** 092002 (2021).

116. Hazra, S., Mitra, S. & Sen, A. Cross-stream migration of droplets in a confined shear-thinning viscoelastic flow: Role of shear-thinning induced lift. *Physics of Fluids* **32,** 092007 (2020).

117. Liu, J. & Pan, Z. Self-ordering and organization of in-line particle chain in a square microchannel. *Physics of Fluids* **34** (2022).

118. Hu, X., Li, X., Lin, P. & Zhu, Z. Self-organizing single-line particle trains with differently shaped particles in a channel flow. *Physics of Fluids* **35** (2023).

119. D'Avino, G. & Maffettone, P. L. Particle dynamics in viscoelastic liquids. *Journal of Non-Newtonian Fluid Mechanics* **215,** 80–104 (2015).

120. Petit, L. & Noetinger, B. Shear-induced structures in macroscopic dispersions. *Rheologica acta* **27,** 437–441 (1988).

121. Lyon, M., Mead, D., Elliott, R. & Leal, L. Structure formation in moderately concentrated viscoelastic suspensions in simple shear flow. *Journal of Rheology* **45,** 881–890 (2001).

122. Won, D. & Kim, C. Alignment and aggregation of spherical particles in viscoelastic fluid under shear flow. *Journal of non-newtonian fluid mechanics* **117,** 141–146 (2004).

123. Scirocco, R., Vermant, J. & Mewis, J. Effect of the viscoelasticity of the suspending fluid on structure formation in suspensions. *Journal of non-Newtonian fluid mechanics* **117,** 183–192 (2004).

124. Pasquino, R., Snijkers, F., Grizzuti, N. & Vermant, J. The effect of particle size and migration on the formation of flow-induced structures in viscoelastic suspensions. *Rheologica Acta* **49,** 993–1001 (2010).

125. Pasquino, R., Panariello, D. & Grizzuti, N. Migration and alignment of spherical particles in sheared viscoelastic suspensions. A quantitative determination of the flow-induced self-assembly kinetics. *Journal of colloid and interface science* **394,** 49–54 (2013).

126. Pasquino, R., D'Avino, G., Maffettone, P. L., Greco, F. & Grizzuti, N. Migration and chaining of noncolloidal spheres suspended in a sheared viscoelastic medium. Experiments and numerical simulations. *Journal of Non-Newtonian Fluid Mechanics* **203,** 1–8 (2014).

127. Groisman, A. & Steinberg, V. Elastic turbulence in a polymer solution flow. *Nature* **405,** 53–55 (2000).

128. Zilz, J. *et al.* Geometric scaling of a purely elastic flow instability in serpentine channels. *Journal of Fluid Mechanics* **712,** 203–218 (2012).

129. Howe, A. M., Clarke, A. & Giernalczyk, D. Flow of concentrated viscoelastic polymer solutions in porous media: effect of MW and concentration on elastic turbulence onset in various geometries. *Soft Matter* **11,** 6419–6431 (2015).

130. Pakdel, P. & McKinley, G. H. Elastic instability and curved streamlines. *Physical Review Letters* **77,** 2459 (1996).

131. McKinley, G. H., Pakdel, P. & Öztekin, A. Rheological and geometric scaling of purely elastic flow instabilities. *Journal of Non-Newtonian Fluid Mechanics* **67,** 19–47 (1996).

132. Tran, E. & Clarke, A. The relaxation time of entangled HPAM solutions in flow. *Journal of Non-Newtonian Fluid Mechanics* **311,** 104954 (2023).

133. Tassieri, M. Microrheology with optical tweezers: peaks & troughs. *Current Opinion in Colloid & Interface Science* **43.** Rheology, 39–51. ISSN: 1359-0294. https://www.sciencedirect.com/science/article/pii/S1359029418301316 (2019).

134. Ashkin, A. Acceleration and Trapping of Particles by Radiation Pressure. *Phys. Rev. Lett.* **24,** 156–159. https://link.aps.org/doi/10.1103/PhysRevLett.24.156 (4 Jan. 1970).

135. Tassieri, M. Linear microrheology with optical tweezers of living cells 'is not an option'! *Soft Matter* **11,** 5792–5798. http://dx.doi.org/10.1039/C5SM01133G (29 2015).

136. Mason, T. G. & Weitz, D. A. Optical Measurements of Frequency-Dependent Linear Viscoelastic Moduli of Complex Fluids. *Phys. Rev. Lett.* **74,** 1250–1253. https://link.aps.org/doi/10.1103/PhysRevLett.74.1250 (7 Feb. 1995).

137. Smith, M. G., Gibson, G. M. & Tassieri, M. i-RheoFT: Fourier transforming sampled functions without artefacts. *Scientific Reports* **11,** 24047. ISSN: 2045-2322. https://doi.org/10.1038/s41598-021-02922-8 (Dec. 2021).

138. Tassieri, M. *et al.* Measuring storage and loss moduli using optical tweezers: Broadband microrheology. *Phys. Rev. E* **81,** 026308. https://link.aps.org/doi/10.1103/PhysRevE.81.026308 (2 Feb. 2010).

139. Preece, D. *et al.* Optical tweezers: wideband microrheology. *Journal of Optics* **13,** 044022. https://doi.org/10.1088/2040-8978/13/4/044022 (Mar. 2011).

140. Derks, D., Wisman, H., Van Blaaderen, A. & Imhof, A. Confocal microscopy of colloidal dispersions in shear flow using a counter-rotating cone–plate shear cell. *Journal of Physics: Condensed Matter* **16,** S3917 (2004).

141. Tees, D., Coenen, O. & Goldsmith, H. L. Interaction forces between red cells agglutinated by antibody. IV. Time and force dependence of break-up. *Biophysical journal* **65,** 1318–1334 (1993).

142. Tassieri, M., Evans, R. M. L., Warren, R. L., Bailey, N. J. & Cooper, J. M. Microrheology with optical tweezers: data analysis. *New Journal of Physics* **14,** 115032. https://doi.org/10.1088/1367-2630/14/11/115032 (Nov. 2012).

143. Tassieri, M., Ramírez, J., Karayiannis, N. C., Sukumaran, S. K. & Masubuchi, Y. i-Rheo GT: Transforming from Time to Frequency Domain without Artifacts. *Macromolecules* **51,** 5055–5068. ISSN: 0024-9297. https://doi.org/10.1021/acs.macromol.8b00447 (July 2018).

144. Colby, R. H. & Rubinstein, M. Polymer physics. *New-York: Oxford University* **100,** 274 (2003).

145. Olagunju, D. O. Instabilities and bifurcations of von Kármán similarity solutions in swirling viscoelastic flow. *Zeitschrift für angewandte Mathematik und Physik ZAMP* **46,** 224–238 (1995).

146. Chen, C., Miao, W., Zhou, C. & Wu, H. Thermogravimetric pyrolysis kinetics of bamboo waste via Asymmetric Double Sigmoidal (Asym2sig) function deconvolution. *Bioresource technology* **225,** 48–57 (2017).

147. Mirsepassi, A., Rajaram, B., Mohraz, A. & Dunn-Rankin, D. Particle chaining and chain dynamics in viscoelastic liquids. *Journal of Non-Newtonian Fluid Mechanics* **179,** 1–8 (2012).

148. Vazquez, M., Schmalzing, D., Matsudaira, P., Ehrlich, D. & McKinley, G. Shear-induced degradation of linear polyacrylamide solutions during pre-electrophoretic loading. *Analytical chemistry* **73,** 3035–3044 (2001).